Research on Analysis Techniques for Beam Structures Using Functionally Graded Materials by Means of Finite Element Method

（有限要素法による傾斜機能材料を用いた梁構造の解析手法に関する研究）

January 2017

Submitted to the Department of Architecture
in Fulfillment of the Requirements for the Degree of
DOCTOR OF ENGINEERING
in Department of Architecture at the College of Engineering
NIHON UNIVERSITY

Trinh Thanh Huong

Abstract

At present, members using functionally graded materials (FGMs) are widely applied to production of manned spaceships. This is to cope with the problem that the surface of the space-planes reaches an extremely high temperature and the covering heat-resistant ceramic peels off and falls out in the atmosphere. The new concept of heat-resistant material used to protect the aircrafts in the space plane from extremely high temperature proposes a member whose composition has been continuously changed from metal to ceramic in the cross section. This conception alleviates the problem of jointing constituents as well as has many other useful features such as no stress concentration which is commonly found in conventional composite materials (Composite).

If such a member is applied to a large-scale building/civil engineering structure, the structure can be optimally distributed in intensity. As a result, it is possible to design homogeneous buildings or intentionally changed strength buildings.

Currently, Fourier transform, Laplace transform, and theoretical solution are used for analysis of members having such characteristics; however, these are complicated and poor in versatility. Therefore, this research proposes a new analytical method by incorporating theoretical formulas that can analyze members using functionally graded technology by means of the finite element method (FEM). As part of the research, new shape functions are developed in order to obtain a minimum number of element divisions and high precision in numerical results.

Chapter 1 describes the background and purpose of the research.

Chapter 2 formulates FGM beam structures based on conventional beam theories, and proposes new shape functions as well.

Chapter 3 describes the formulation of the FGM beam structures used in the finite element method.

Chapter 4 describes analysis techniques using in the research, including co-rotational approach, incremental iteration method in combination with arc-length control method, and implicit average constant acceleration Newmark method. With the aid of these

techniques, not only the nonlinear equilibrium equations are solved but also the large deformation is analyzed, paving the way for performance of elastic-plastic and post-buckling analyses.

Chapters 5 and 6 examine the accuracy of new shape functions proposed in the research by using application examples of modified cross section beams in static analysis and dynamic analysis. The results are displayed in comparison with reference works.

Chapter 7 describes the effectiveness of FGM beam structures in the dynamic problems.

Chapter 8 investigates the behaviour after buckling of axially FGM beam structures.

Chapter 9 analyzes the elastic-plastic of the FGM beam structure resting on elastic foundation.

Chapter 10 summarizes the research and discusses future prospects.

TABLE OF CONTENT

Acknowledgements

This research was completed with much support from researchers at the Department of Architecture of the College of Engineering, Nihon University. I wish to express my sincerest gratitude to institutes and people who made substantial contributions to the completion of this dissertation as follows:

Prof. Buntara Sthenly Gan, Department of Architecture, College of Engineering, Nihon University, the supervisor of this dissertation who offered enlightened guidance, valuable comments, suggestions, assistance and encouragement towards the completion of this dissertation.

I would also like to thank my former supervisor Dr. Nguyen Dinh Kien at the Vietnam Academy of Science and Technology, Hanoi, Vietnam who played an important role providing useful comments, suggestions and guidance. And I would like to thank the members of Computational Applied Mechanics Laboratory for assisting with my stay in Japan.

I would like to thank the Ministry of Education, Culture, Sports, Science and Technology, JAPAN (MEXT Scholarship) for providing financial supports for living and tuition during my doctoral course in the College of Engineering, Nihon University.

A very special note of appreciation is expressed to my father, mother, husband and son for their concern, self–sacrifice and encouragement both directly and indirectly for me.

Chapter 1: Introduction of FGM

1.1. History

Although the concept of Functionally Graded Materials (FGMs) was initiated by Japanese scientists in 1984 in Sendai [67], these sorts of materials have been exploited in numerous biological systems in nature such as bamboo, plant stems, leaf shafts or feathers, and human and animal bone, to name but a few.

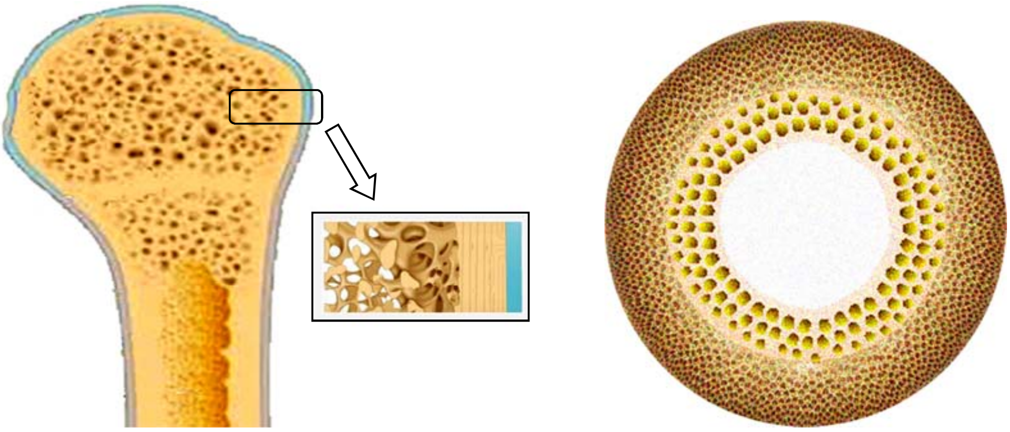

(a) Bone (b) Bamboo

Figure 1.1: FGM in nature

Bone and bamboo are two examples of natural FGMs displayed in Fig.1.1 as an illustration. While biological structures are living organisms that can be characterized by adaptability in order to accommodate to their physical environment, human-made FGM structures require a functional selection and combination of materials for special purposes.

1.2. FGM as new materials

FGMs have been of great importance to many researchers for a long time because of their wide range of applications in structural mechanics. The newly-created materials have promising applications in many fields such as space projects, the energy sector, communications projects, the defence industries, biomedical sectors and miscellaneous others (Figs. 1.2, 1.3). There is a comprehensive list of publications on analyses of FGM structures subjected to different loadings is given in a review paper by Birman and Byrd [10]. Previously, Chakraborty [17] employed the solutions of the governing differential equations of an FGM Timoshenko segment as interpolation functions to formulate a shear deformation beam element for analyzing the thermo-elastic behaviour of FGM beams. In 2008, Kadoli [58] formulated a beam element based on the higher-order shear deformation beam theory for studying the static behaviour of FGM beams under ambient temperature. Simultaneously, Li [75] presented a unified approach for investigating the static and dynamic behaviour of FGM beams with rotary inertia and shear deformation included. Taking the shift in position of the neutral axis into account, Kang and Li [59], [60], in the two consecutive years of 2009 and 2010, derived expressions for tip displacements of a non-linear FGM cantilever beam under a tip load or a tip moment. At the same time, Şimşek and his co-workers [114], [116] studied the vibration of FGM beams subjected to a moving load by using polynomial series as trial functions for the displacements and rotation of the beam. Singh and Li [119], in 2009, proposed a model for computing buckling loads of non-uniform axially FGM columns by approximating the column by another one with piecewise uniform geometric and material properties. Meanwhile, Sina [118] presented an analytical method based on a new beam theory for free vibration analysis of FGM beams. Two years later, in 2011, Alshorbagy [1] studied the free vibration of FGM Bernoulli beams with material gradation in axial or transversal directions through the thickness by using the finite element method. Simultaneously, Fallah and Aghdam [31] derived the non-linear governing differential equation for geometrically non-linear vibration and post-buckling analysis of FGM beams resting on a non-linear elastic foundation. Meanwhile, Shahba [111] used the static solutions of a homogeneous Timoshenko beam element to formulate the mass and stiffness matrices for computing the critical loads and vibration characteristics of tapered Timoshenko beams made of axial FGM. In 2014, Kocatürk [68] presented the post-buckling analysis of an FGM Timoshenko beam subjected to thermal loading by using the total Lagrangian Timoshenko beam formulation. A year later, taking the shift in the neutral axis position into account, Eltaher [30] derived the finite element formulation for computing the natural frequencies, and showed that ignoring the shift in the neutral axis position leads to an overestimation of the computed natural frequencies. At the same year, Nguyen [91] investigated the dynamic response of functionally graded non-uniform sections of Timoshenko beams traversed by a variable speed moving load. Nguyen and his co-workers [90], [92], [93], then derived the finite element formulation for studying the large displacement behaviour of FGM beams and frames.

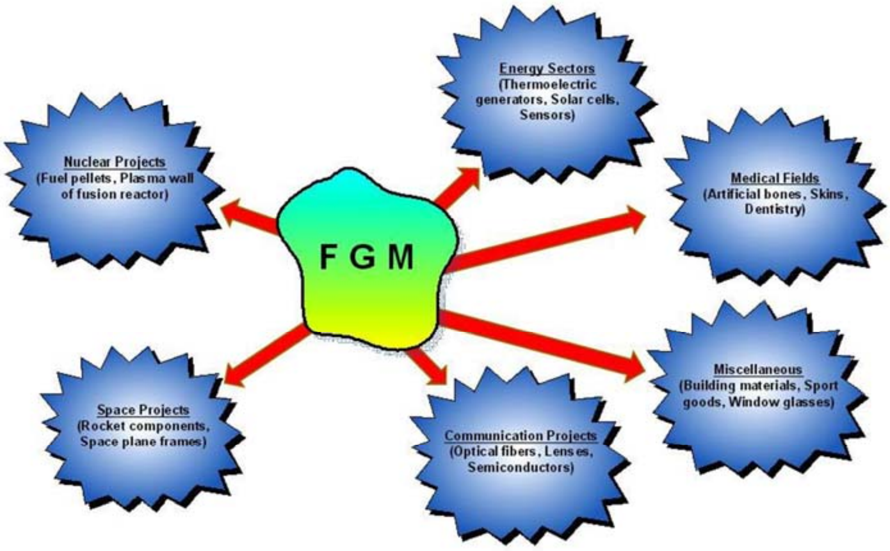

Figure 1.2: FGM as a new material

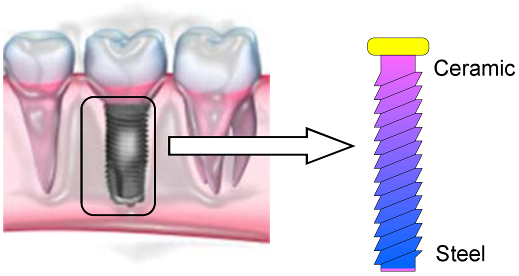

Figure 1.3: FGM used in ceramic–steel dental implant

1.3. Modelling effective FGM properties

FGMs can be formed by varying the percentage of constituents in any desired spatial direction in order to create new materials with specific physical and mechanical properties. The effective properties of the resulting material exhibit continuous change, thus eliminating the interface problem and reducing the stress concentration that is often met in conventional composites.

In general, FGMs consist of two distinct material phases of ceramic and metal alloy in order to take advantage of the good high temperature strength and creep resistance of ceramics together with the high fracture toughness and excellent thermal shock resistance of metallic materials.

Various analytical approaches to FGM modelling are reported in [56]:

- Self-consistent estimates
- Mori–Tanaka scheme
- Composite sphere assemblage model
- Composite cylindrical assemblage model
- The simplified strength of materials method
- The methods of cells
- Micromechanical model

The following three popular types of variation in constructing FGMs are reported in [56], [117]:

- The exponential law

$$P(z) = P_t \exp\left(-\lambda\left(1-\frac{2z}{h}\right)\right) \tag{1.1}$$

where

$$\lambda = \frac{1}{2}\ln\left(\frac{P_t}{P_b}\right) \tag{1.2}$$

- The power law in the thickness direction

$$P(z) = \left(P_t - P_b\right)\left(\frac{z}{h}+\frac{1}{2}\right)^n + P_b \tag{1.3}$$

in which *P(z)* is the effective material properties of the FGM structure (including

Young's modulus E, shear modulus G, or mass density ρ,...); h is the structure's thickness; P_t and P_b are material properties at the top-most ($z = h/2$) and bottom-most ($z = -h/2$) surfaces, respectively; n is the non-negative power law index.

- The power law in the longitudinal direction

$$P(x) = \left(P_l - P_r\right)\left(1 - \frac{x}{L}\right)^n + P_r \tag{1.4}$$

where Pl and Pr are material properties at the left-end and the right-end of the structures, respectively; L is the total length of the structures (beam).

Chapter 2: Beam made of FGM

2.1 Beam theory

Beam models have been helpful in solving a large number of engineering problems. Beam theories are extensively used to analyze the structural behaviour of slender bodies such as columns, arches, blades, aircraft wings, and bridges [33].

2.1.1 Euler–Bernoulli beam

The Euler–Bernoulli beam theory is derived from the following assumptions:

- the cross-section is rigid on its plane;
- the cross-section rotates around a neutral surface remaining in-plane;
- the cross-section remains perpendicular to the neutral surface during deformation.

Displacement field

According to the first hypothesis, the in-plane displacements u_x and u_z depend on the axial coordinate y only:

$$\begin{aligned} \varepsilon_{xx} &= \frac{\partial u_x}{\partial x} = 0 \\ \varepsilon_{zz} &= \frac{\partial u_z}{\partial z} = 0 \\ \gamma_{xz} &= \frac{\partial u_x}{\partial z} + \frac{\partial u_z}{\partial x} = 0 \end{aligned} \tag{2.1}$$

Thus

$$\begin{aligned} u_x(x,y,z) &= u_{x1}(y) \\ u_z(x,y,z) &= u_{z1}(y) \end{aligned} \tag{2.2}$$

Based on the second hypothesis, axial displacement u_y is linear versus the in-plane coordinates:

$$u_y(x,y,z) = u_{y1}(y) + \phi_z(y)x + \phi_x(y)z \tag{2.3}$$

where ϕ_z and ϕ_x are the rotation angles along the *z*- and *x*-axis, respectively.

According to the third hypothesis and based on the definition of shear strains, the shear deformations are:

$$\gamma_{yz} = \gamma_{yx} = 0 \tag{2.4}$$

The rotation angles are obtained as functions of the derivatives of displacements:

$$\begin{aligned} \varepsilon_{xy} &= \frac{\partial u_y}{\partial x} + \frac{\partial u_x}{\partial y} = \phi_z + \frac{\partial u_{x1}}{\partial y} = 0 \\ \varepsilon_{yz} &= \frac{\partial u_y}{\partial z} + \frac{\partial u_z}{\partial y} = \phi_x + \frac{\partial u_{z1}}{\partial y} = 0 \end{aligned} \tag{2.5}$$

Thus

$$\begin{aligned} \phi_z &= -\frac{\partial u_{x1}}{\partial y} \\ \phi_x &= -\frac{\partial u_{z1}}{\partial y} \end{aligned} \tag{2.6}$$

The displacement field of the Euler–Bernoulli beam theory is then

$$\begin{aligned} u_x &= u_{x1} \\ u_y &= u_{y1} - \frac{\partial u_{x1}}{\partial y} x - \frac{\partial u_{z1}}{\partial y} z \\ u_z &= u_{z1} \end{aligned} \tag{2.7}$$

Strains

According to the kinematic hypotheses, the Euler–Bernoulli beam theory accounts for the axial strain only:

$$\varepsilon_{yy} = \frac{\partial u_y}{\partial y} = \frac{\partial u_{y1}}{\partial y} - \frac{\partial^2 u_{x1}}{\partial y^2} x - \frac{\partial^2 u_{z1}}{\partial y^2} z \tag{2.8}$$

Stresses and stress resultants

The axial stress, σ_{yy}, is obtained from the axial strain:

$$\sigma_{yy} = E\varepsilon_{yy} = E\left(\frac{\partial u_{y1}}{\partial y} - \frac{\partial^2 u_{x1}}{\partial y^2} x - \frac{\partial^2 u_{z1}}{\partial y^2} z \right) \tag{2.9}$$

The stress resultants:

- axial force $N(y)$

$$\begin{aligned} N(y) &= \int_\Omega \sigma_{yy} d\Omega \\ &= \int_\Omega E\left(\frac{\partial u_{y1}}{\partial y} - \frac{\partial^2 u_{x1}}{\partial y^2}x - \frac{\partial^2 u_{z1}}{\partial y^2}z\right)d\Omega \\ &= E\left(\frac{\partial u_{y1}}{\partial y}\underbrace{\int_\Omega d\Omega}_{A} - \frac{\partial^2 u_{x1}}{\partial y^2}\underbrace{\int_\Omega x d\Omega}_{S_x} - \frac{\partial^2 u_{z1}}{\partial y^2}\underbrace{\int_\Omega z d\Omega}_{S_z}\right) \end{aligned} \tag{2.10}$$

- bending moment versus the z-axis $M_Z(y)$

$$\begin{aligned} M_z(y) &= \int_\Omega \sigma_{yy} x d\Omega \\ &= \int_\Omega E\left(\frac{\partial u_{y1}}{\partial y} - \frac{\partial^2 u_{x1}}{\partial y^2}x - \frac{\partial^2 u_{z1}}{\partial y^2}z\right)x d\Omega \\ &= E\left(\frac{\partial u_{y1}}{\partial y}\underbrace{\int_\Omega x d\Omega}_{S_x} - \frac{\partial^2 u_{x1}}{\partial y^2}\underbrace{\int_\Omega x^2 d\Omega}_{I_{xx}} - \frac{\partial^2 u_{z1}}{\partial y^2}\underbrace{\int_\Omega xz d\Omega}_{I_{xz}}\right) \end{aligned} \tag{2.11}$$

- bending moment versus the x-axis $M_x(y)$

$$\begin{aligned} M_x(y) &= -\int_\Omega \sigma_{yy} z d\Omega \\ &= -\int_\Omega E\left(\frac{\partial u_{y1}}{\partial y} - \frac{\partial^2 u_{x1}}{\partial y^2}x - \frac{\partial^2 u_{z1}}{\partial y^2}z\right)z d\Omega \\ &= -E\left(\frac{\partial u_{y1}}{\partial y}\underbrace{\int_\Omega z d\Omega}_{S_z} - \frac{\partial^2 u_{x1}}{\partial y^2}\underbrace{\int_\Omega xz d\Omega}_{I_{xz}} - \frac{\partial^2 u_{z1}}{\partial y^2}\underbrace{\int_\Omega z^2 d\Omega}_{I_{xx}}\right) \end{aligned} \tag{2.12}$$

where A is the cross-section area; S_x and S_z are static momenta; and I_{xx}, I_{xz} and I_{zz} are momenta of inertia. Eqs. (2.10), (2.11) and (2.12) can be written in matrix form:

$$\begin{Bmatrix} N \\ M_z \\ -M_x \end{Bmatrix} = \begin{bmatrix} A & S_x & S_z \\ S_x & I_{zz} & I_{xz} \\ S_z & I_{xz} & I_{xx} \end{bmatrix} \begin{Bmatrix} k_1 \\ k_2 \\ k_3 \end{Bmatrix} \tag{2.13}$$

2.1.2 Timoshenko beam

In the Timoshenko beam theory, the third kinematic a priori assumption of the Euler–Bernoulli beam theory is relaxed.

Displacement field

According to the previous a priori kinematic assumptions, the displacement field of the Timoshenko beam theory is

$$\begin{aligned} u_x(x,y,z) &= u_{x1}(y) \\ u_y(x,y,z) &= u_{y1}(y) + \phi_z(y)x + \phi_x(y)z \\ u_z(x,y,z) &= u_{z1}(y) \end{aligned} \tag{2.14}$$

Strains

$$\begin{aligned} \varepsilon_{yy} &= \frac{\partial u_y}{\partial y} = \frac{\partial u_{y1}}{\partial y} + \frac{\partial \phi_z}{\partial y}x + \frac{\partial \phi_x}{\partial y}z \\ \gamma_{xy} &= \frac{\partial u_y}{\partial x} + \frac{\partial u_x}{\partial y} = \phi_z + \frac{\partial u_{x1}}{\partial y} \\ \gamma_{yz} &= \frac{\partial u_y}{\partial z} + \frac{\partial u_z}{\partial y} = \phi_x + \frac{\partial u_{z1}}{\partial y} \end{aligned} \tag{2.15}$$

Stresses and stress resultants

$$\begin{aligned} \sigma_{yy} &= E\varepsilon_{yy} = E\left(\frac{\partial u_{y1}}{\partial y} + \frac{\partial \phi_z}{\partial y}x + \frac{\partial \phi_x}{\partial y}z\right) \\ \sigma_{xy} &= \kappa G\left(\phi_z + \frac{\partial u_{x1}}{\partial y}\right) \\ \sigma_{yz} &= \kappa G\left(\phi_x + \frac{\partial u_{z1}}{\partial y}\right) \end{aligned} \tag{2.16}$$

where κ is the shear correction factor.

The stress resultants

- axial force $N(y)$

$$\begin{aligned} N &= \int_\Omega \sigma_{yy} d\Omega \\ &= E\int_\Omega \left(\frac{\partial u_{y1}}{\partial y} + \frac{\partial \phi_z}{\partial y}x + \frac{\partial \phi_x}{\partial y}z\right) d\Omega \end{aligned} \tag{2.17}$$

- bending moment versus the *z*-axis M_z

$$M_z = \int_\Omega \sigma_{yy} z d\Omega$$
$$= E \int_\Omega \left(\frac{\partial u_{y1}}{\partial y} z + \frac{\partial \phi_z}{\partial y} xz + \frac{\partial \phi_x}{\partial y} z^2 \right) d\Omega \tag{2.18}$$

- bending moment versus the *x*-axis M_x

$$M_x = -\int_\Omega \sigma_{yy} x d\Omega$$
$$= -E \int_\Omega \left(\frac{\partial u_{y1}}{\partial y} x + \frac{\partial \phi_z}{\partial y} x^2 + \frac{\partial \phi_x}{\partial y} xz \right) d\Omega \tag{2.19}$$

- shear force along the *x*-axis V_x

$$V_x = \int_\Omega \sigma_{xy} d\Omega$$
$$= \int_\Omega \kappa G \left(\phi_z + \frac{\partial u_{x1}}{\partial y} \right) d\Omega \tag{2.20}$$
$$= \kappa G \left(\phi_z + \frac{\partial u_{x1}}{\partial y} \right) A$$

- shear force along the *z*-axis V_z

$$V_z = \int_\Omega \sigma_{yz} d\Omega$$
$$= \int_\Omega \kappa G \left(\phi_x + \frac{\partial u_{z1}}{\partial y} \right) d\Omega \tag{2.21}$$
$$= \kappa G \left(\phi_x + \frac{\partial u_{z1}}{\partial y} \right) A$$

2.2. FGM in beam theory

2.2.1. Prismatic FGM beam

Consider the beam to have a cross-section assumed to be rectangular with width *b* and height *h* (Fig. 2.1).

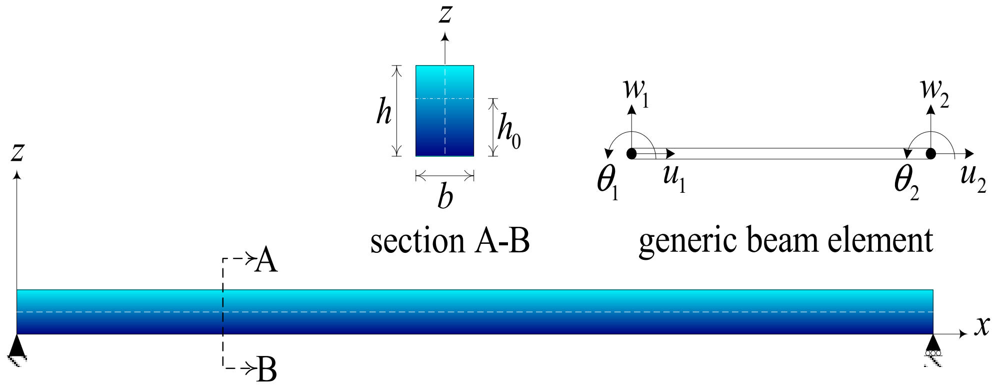

Figure 2.1: FGM beam and its generic element

The beam material is assumed to be an FGM composed of two constituent materials, and the effective material properties are graded in the thickness direction (*z*-direction) according to a power law distribution as

$$\begin{aligned}
&P(z)=P_b+\left(P_t-P_b\right)\left(\frac{z}{h}\right)^n\\
&V_t(z)=\left(\frac{z}{h}+\frac{1}{2}\right)^n\\
&V_t+V_b=1
\end{aligned} \tag{2.22}$$

where $P(z)$ represents the effective material properties, including Young's modulus, shear modulus and mass density; P_t and P_b are the material properties of the material at the top and bottom surfaces, respectively. V_t and V_b respectively denote the volume fractions of the materials at the top and bottom surfaces; *n* is the non-negative power-law index, which defines the distribution of the constituent materials.

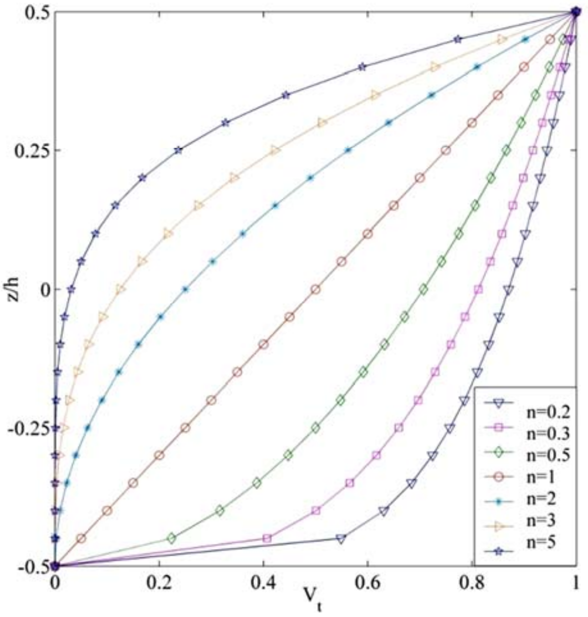

Figure 2.2: Variation in volume fraction through the thickness of FGM beams

Fig. 2.2 shows the variation in the volume fraction through the beam thickness for various values of the index *n* of the FGM beam. Due to variation of the effective Young's modulus, the neutral axis is no longer at the mid-plane, but it shifts from the mid-plane by a distance h_0, which can be determined by imposing the axial resultant in a cross-section that vanishes:

$$N = \int_A \sigma_x dA = 0 \tag{2.23}$$

then

$$h_0 = \frac{\int_{-h/2}^{h/2} E(z) z dz}{\int_{-h/2}^{h/2} E(z) dz} = \frac{hn\left(E_t - E_b\right)}{2\left(n+2\right)\left(E_t + nE_b\right)} \tag{2.24}$$

Adopting Timoshenko beam theory, the axial and transverse displacements, $u_1(x, z, t)$ and $u_3(x, z, t)$, respectively at any point of the beam are given by

$$\begin{aligned} u_1(x,z,t) &= u(x,t) - z\theta(x,t) \\ u_3(x,z,t) &= w(x,t) \end{aligned} \tag{2.25}$$

where *u(x,t)* and $w(x, t)$ are the axial and transverse displacements of the point on the neutral axis *x*; $\theta(x, t)$ is the rotation of the cross-section at a point with abscissa

x; z is the distance from any arbitrary point to the neutral axis.

Based on the assumptions of Hooke's law, the axial strain ε_x, shear strain γ_{xz} and their corresponding axial and shear stresses, σ_x and τ_{xz}, respectively, are as follows:

$$\begin{aligned} \varepsilon_x &= \frac{\partial u(x,t)}{\partial x} - z\frac{\partial \theta(x,t)}{\partial x} \\ \gamma_{xz} &= \frac{\partial w(x,t)}{\partial x} - \theta(x,t) \\ \sigma_x &= E(z)\varepsilon_x \\ \tau_{xz} &= \kappa G(z)\gamma_{xz} \end{aligned} \tag{2.26}$$

The strain energy of the beam can be written as

$$\begin{aligned} U &= \frac{1}{2}\int_V (\sigma_x\varepsilon_x + \tau_{xz}\gamma_{xz})dV \\ &= \frac{1}{2}\int_0^l \left[A_{11}\left(\frac{\partial u}{\partial x}\right)^2 - 2A_{12}\frac{\partial u}{\partial x}\frac{\partial \theta}{\partial x} + A_{22}\left(\frac{\partial \theta}{\partial x}\right)^2 + \kappa A_{33}\left(\frac{\partial w}{\partial x} - \theta\right)^2 \right]dx \end{aligned} \tag{2.27}$$

Kinetic energy is written as

$$\begin{aligned} T &= \frac{1}{2}\int_V \rho(z)\left(\dot{u}^2 + \dot{w}^2\right)dV \\ &= \frac{1}{2}\int_0^l \left[I_{11}\left(\dot{u}^2 + \dot{w}^2\right) - 2I_{12}\dot{u}\dot{\theta} + I_{22}\dot{\theta}^2 \right]dx \end{aligned} \tag{2.28}$$

where κ is the shear correction factor; $E(z)$, $G(z)$ and $\rho(z)$ are the Young's modulus, shear modulus and mass density of the material on the section with abscissa z; V is the volume; an over dot symbol denotes the time derivative; the stiffness coefficients and mass moment of inertia in Eq. (2.27) are defined as

$$\begin{aligned} \left(A_{11}, A_{12}, A_{22}\right) &= \int_A E(z)\left(1, z, z^2\right)dA \\ A_{33} &= \int_A G(z)dA \\ \left(I_{11}, I_{12}, I_{22}\right) &= \int_A \rho(z)\left(1, z, z^2\right)dA \end{aligned} \tag{2.29}$$

where A is the cross-section area.

It should be noted that due to the shift in the neutral axis position, the integrals in Eq. (2.29) should be computed in the manner described by Kang and Li [59], [60].

$$
\begin{aligned}
A_{11} &= \int_A E(z)dA = b(x)\left[\int_0^{h-h_0} E(h_0+z)dz + \int_0^{h_0} E(h_0-z)dz\right] \\
A_{12} &= \int_A zE(z)dA = b(x)\left[\int_0^{h-h_0} zE(h_0+z)dz + \int_0^{h_0} zE(h_0-z)dz\right] \\
A_{22} &= \int_A z^2E(z)dA = b(x)\left[\int_0^{h-h_0} z^2E(h_0+z)dz + \int_0^{h_0} z^2E(h_0-z)dz\right] \\
A_{33} &= \int_A G(z)dA = b(x)\left[\int_0^{h-h_0} G(h_0+z)dz + \int_0^{h_0} G(h_0-z)dz\right] \\
I_{11} &= \int_A \rho(z)dA = b(x)\left[\int_0^{h-h_0} \rho(h_0+z)dz + \int_0^{h_0} \rho(h_0-z)dz\right] \\
I_{12} &= \int_A z\rho(z)dA = b(x)\left[\int_0^{h-h_0} z\rho(h_0+z)dz + \int_0^{h_0} z\rho(h_0-z)dz\right] \\
I_{22} &= \int_A z^2\rho(z)dA = b(x)\left[\int_0^{h-h_0} z^2\rho(h_0+z)dz + \int_0^{h_0} z^2\rho(h_0-z)dz\right]
\end{aligned}
\tag{2.30}
$$

2.2.2. FGM beam in thermal environment

The beam with total length L, cross-section height h and cross-section width b, shown in Fig. 2.3, will be investigated in this sub-section.

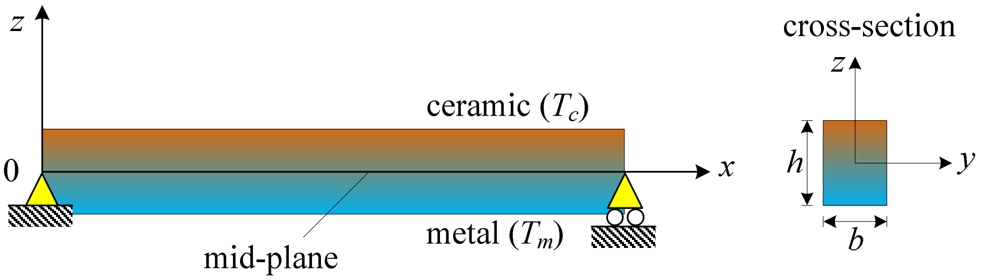

Figure 2.3: A simply supported FGM beam in thermal environment

The x-axis is chosen to be on the mid-plane, and the z-axis is perpendicular to the mid-plane. The beam material is formed from ceramic and metal, where the volume fraction of ceramic (V_C) and metal (V_m) is assumed to be given by

$$
\begin{aligned}
V_c &= \left(\frac{z}{h}+\frac{1}{2}\right)^n \\
V_m + V_c &= 1
\end{aligned}
\tag{2.31}
$$

where n ($0 \le n < \infty$) is the grading index.

In Eq. (2.31), the subscripts "c" and "m" are used to indicate ceramic and metal, respectively. The beam material is considered to be dependent on the temperature, and a typical property (P) is a function of temperature (T) as [132]

$$P = P_0\left(P_{-1}T^{-1} + 1 + P_1T + P_2T^2 + P_3T^3\right) \tag{2.32}$$

where T=T_0+ΔT, in which T_0 = 300K is the reference temperature and ΔT is the temperature rise, in the current environment temperature; P_{-1}, P_0, P_1, P_2 and P_3 are coefficients of T and they are unique to the constituents. The effective material properties are evaluated by Voigt's model:

$$P(z,T) = P_c(T)V_c + P_m(T)V_m \tag{2.33}$$

From Eqs. (2.31) and (2.33), the effective Young's modulus, thermal expansion and mass density are given by

$$\begin{aligned} E(z,T) &= \left[E_c(T) - E_m(T)\right]\left(\frac{z}{h} + \frac{1}{2}\right)^n + E_m(T) \\ \alpha(z,T) &= \left[\alpha_c(T) - \alpha_m(T)\right]\left(\frac{z}{h} + \frac{1}{2}\right)^n + \alpha_m(T) \\ \rho(z) &= (\rho_c - \rho_m) + \left(\frac{z}{h} + \frac{1}{2}\right)^n + \rho_m \end{aligned} \tag{2.34}$$

where the mass density is considered to be independent of the temperature. In this work, the temperature is considered to vary in the thickness direction only, and it is assumed that the temperature being imposed is T_m at the bottom surface and T_c at the top surface. With this condition, the distribution of temperature in the thickness can be obtained as the solution of the following Fourier equation:

$$-\frac{d}{dz}\left[K(z)\frac{dT}{dz}\right] = 0 \tag{2.35}$$

where $K(z)$ is the thermal conductivity, assumed to be independent of the temperature. The solution of Eq. (2.35) has the form

$$T = T_c + \frac{(T_c - T_m)}{\int\limits_{-h/2}^{h/2} \frac{1}{K(z,T)} dz} \int\limits_{-h/2}^{z} \frac{1}{K(z,T)} dz \tag{2.36}$$

If $T_c = T_m$, Eq. (2.36) gives a uniform temperature rise (UTR). Otherwise, it describes a non-linear temperature rise (NLTR).

2.2.3. Non-prismatic FGM beam

The beam shown in Fig. 2.4, with total length L and a constant cross-section height h, is assumed to be formed from two different materials.

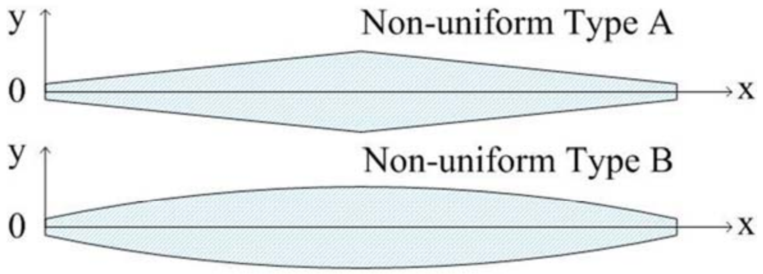

Figure 2.4: Two types of non-prismatic FGM beam

The solid cross-section area $A(x)$ and moment of inertia $I(x)$ are assumed to vary longitudinally in the two following manners:

- Type A

$$A(x) = A_m \left(1 - \alpha \left|\frac{x}{L} - \frac{1}{2}\right|\right)$$

$$I(x) = I_m \left(1 - \alpha \left|\frac{x}{L} - \frac{1}{2}\right|\right)$$

- Type B

$$A(x) = A_m \left(1 - \alpha \left|\frac{x}{L} - \frac{1}{2}\right|\right)^2$$

$$I(x) = I_m \left(1 - \alpha \left|\frac{x}{L} - \frac{1}{2}\right|\right)^2$$

where A_m, and I_m denote the area and moment of inertia of the mid-span section, respectively. $0 \le \alpha < 2$ is the non-uniform section parameter, defining how the cross-section varies. The effective property *P* (Young's modulus, shear modulus and mass density) of the beam is assumed to vary in the longitudinal direction according to a power law equation as

$$P(x) = (P_l - P_r)\left(1 - \frac{x}{L}\right)^n + P_r \tag{2.37}$$

where *n* is a non-negative power law index, which defines the distribution of the constituents along the longitudinal direction of the beam. The lower subscripts "*l*" and "*r*" stand for "*left*" and "*right*", respectively. As seen from Eq. (2.37), the left and right end sections of the beam contain one pure material. Adopting Timoshenko beam theory, the axial and transverse displacements, $u_1(x, z, t)$ and $u_3(x, z, t)$, respectively at any point of the beam are given by

$$\begin{aligned} u_1(x,z,t) &= u(x,t) - z\theta(x,t) \\ u_3(x,z,t) &= w(x,t) \end{aligned} \tag{2.38}$$

where $u(x, t)$ and $w(x, t)$ are the axial and transverse displacements of the point on the neutral axis *x*; $\theta(x, t)$ is the rotation of the cross-section at a point with abscissa *x*; *z* is the distance from any arbitrary point to the neutral axis. Based on the assumptions of Hooke's law, the axial strain ε_x, shear strain γ_{xz} and their corresponding axial and shear stresses, σ_x and τ_{xz}, respectively, are as follows:

$$\begin{aligned} \varepsilon_x &= \frac{\partial u(x,t)}{\partial x} - z\frac{\partial \theta(x,t)}{\partial x} \\ \gamma_{xz} &= \frac{\partial w(x,t)}{\partial x} - \theta(x,t) \\ \sigma_x &= E(x)\varepsilon_x \\ \tau_{xz} &= \kappa G(x)\gamma_{xz} \end{aligned} \tag{2.39}$$

The strain energy and the kinetic energy for the non-uniform FGM Timoshenko beam can be written in the following forms:

$$U = \frac{1}{2}\int_0^l \begin{bmatrix} E(x)A(x)\left(\frac{\partial u}{\partial x}\right)^2 + E(x)I(x)\left(\frac{\partial \theta}{\partial x}\right)^2 + \\ \kappa G(x)A(x)\left(\frac{\partial w}{\partial x} - \theta\right)^2 \end{bmatrix} dx$$

$$T = \frac{1}{2}\int_0^l \left[\rho(x)A(x)(\dot{u}^2 + \dot{w}^2) + \rho(x)I(x)\dot{\theta}^2\right] \tag{2.40}$$

where $E(x)$, $G(x)$, $\rho(x)$ are the Young's modulus, shear modulus and mass density of the material on the section with abscissa x.

2.2.4. Elastic–plastic FGM beam

Figure 2.5 shows a cantilever FGM beam made of ceramic and metal.

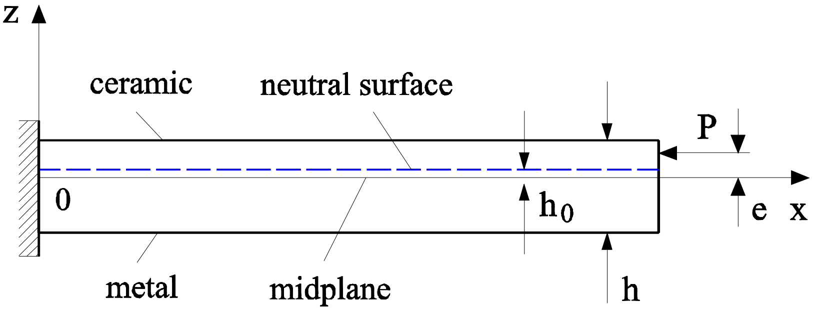

Figure 2.5: A cantilever FGM beam made of ceramic and metal

L, h, b denote the length, height and width of the beam, respectively. The volume fractions of the two constituent materials follow a simple power-law function:

$$V_c = \left(\frac{z}{h} + \frac{1}{2}\right)^n$$

$$V_c + V_m = 1 \tag{2.41}$$

where z is the transverse coordinate; V_c and V_m are respectively the volume fractions of ceramic and metal, and n is the volume fraction exponent; the subscripts "*c*" and "*m*" stand for "*ceramic*" and "*metal*", respectively. The linear elastic behaviour of FG material is described by Hooke's law, and its effective material properties can be evaluated by micromechanics models used in conventional composites. The elastic–plastic behaviour of ceramic/metal FG materials is widely described by using the Tamura–Tomota–Ozawa (TTO) model

[121]. According to this model, the uniaxial stress σ and strain E of a two-phase composite are related to the corresponding average uniaxial stresses and strains of the two constituent materials [42], [55]:

$$\begin{aligned} \sigma &= \sigma_c V_c + \sigma_m V_m \\ \varepsilon &= \varepsilon_c V_c + \varepsilon_m V_m \end{aligned} \tag{2.42}$$

In the TTO model, an additional parameter q representing the ratio of stress to strain transfer is introduced as

$$q = \frac{\sigma_c - \sigma_m}{|\varepsilon_c - \varepsilon_m|},\ 0 < q < \infty \tag{2.43}$$

The value of q depends on the properties of the constituent materials and the micro-structural interaction in the composite.

In the TTO model for a ceramic/metal FGM, the ceramic phase is assumed to be linearly elastic during its deformation process. Plastic deformation of the composite arises from plastic flow of the metal phase when the stress exceeds its yield limit. Here, a bilinear stress–strain relation with an isotropic hardening is assumed for the elastic–plastic behaviour of metal. Figure 2.6 represents a constant tangent modulus E_{tm} when the stress in the metal phase exceeds its yield limit σ_{Ym}.

The elastic–plastic behaviour of the ceramic/metal FGMs also follows a bilinear isotropic hardening model representing a tangent modulus E_t in the plastic region (blue lines in Fig. 2.6).

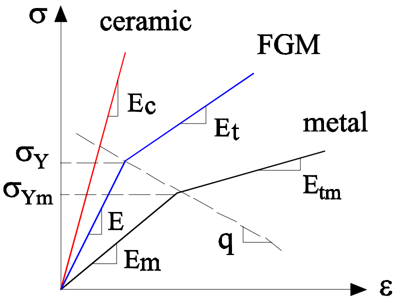

Figure 2.6: Bilinear elastic-plastic model for FGM

The effective properties such as Young's modulus E, yield stress σ_Y and tangent modulus E_t of the FGM are evaluated from the corresponding parameters of constituent materials and the parameter q by using the TTO model as

$$E(z)=\frac{\left(\dfrac{q+E_c}{q+E_m}E_mV_m+E_cV_c\right)}{\left(\dfrac{q+E_c}{q+E_m}V_m+V_c\right)}$$

$$\sigma_Y(z)=\sigma_{Ym}\left(V_m+\frac{q+E_m}{q+E_c}\frac{E_c}{E_m}\frac{E_c}{E_m}V_c\right) \qquad (2.44)$$

$$E_t(z)=\frac{\left(\dfrac{q+E_c}{q+E_0}E_0V_m+E_cV_c\right)}{\left(\dfrac{q+E_c}{q+E_{0m}}V_m+V_c\right)}$$

where $E(z)$ is the elastic modulus; $\sigma_Y(z)$ is the yield stress, and $E_t(z)$ is the tangent modulus; E_c, E_m are the Young's modulus of the ceramic and metal constituents, respectively; E_{0m}, σ_{Ym} are the tangent modulus and yield stress of the metal constituent; and the parameter q is the ratio of stress to strain transfer between the two constituents.

Since the Young's modulus of the composite varies asymmetrically, the neutral axis of the beam is no longer on the mid-plane, but it shifts from the mid-plane by a distance h_0, which can be determined by imposing the axial resultant in a cross-section that vanishes:

$$N=\int_A \sigma_x dA=0 \quad \Rightarrow \quad h_0=\frac{\int_{-h/2}^{h/2} E(z)zdz}{\int_{-h/2}^{h/2} E(z)dz} \qquad (2.45)$$

In order to calculate h_0, Simpson's rule is employed for numerical integration. The rule is described as follows:

$$\int_a^b f(x)dx \approx \frac{b-a}{6}\left[f(a)+4f\left(\frac{a+b}{2}\right)+f(b)\right] \qquad (2.46)$$

Adopting the neutral surface as the reference plane, the axial and transverse displacements at any point according to Euler–Bernoulli beam theory are as follows:

$$
\begin{aligned}
u_1 &= u - (z - h_0)\frac{\partial w}{\partial x} \\
u_2 &= 0 \\
u_3 &= w(x)
\end{aligned}
\tag{2.47}
$$

where u_1, u_2 and u_3 are the displacements at any point in directions of the x-, y- and z-axes. A degenerated form of Green strain can be adopted for the elastic–plastic analysis as

$$
\varepsilon = \frac{\partial u}{\partial x} + \frac{1}{2}\frac{\partial w}{\partial x} + (z - h_0)\chi = \varepsilon_0 + (z - h_0)\chi \tag{2.48}
$$

where $\varepsilon_0 = \frac{\partial u}{\partial x} + \frac{1}{2}\frac{\partial w}{\partial x}$ is the membrane strain, and $\chi = -\frac{\partial^2 w}{\partial x^2}$ is the beam curvature. The incremental stress–strain relationship for the one-dimensional elastic–plastic analysis can be written in the form

$$
d\sigma = E_{ep} d\varepsilon \tag{2.49}
$$

where E_{ep} is the instantaneous modulus, and for the bilinear model adopted herein it has followed the simple form

$$
E_{ep} = \frac{d\sigma}{d\varepsilon} = \begin{cases} E \; if \; \sigma \le \sigma_Y \\ E_t \; if \; \sigma > \sigma_Y \end{cases} \tag{2.50}
$$

where σ_Y and E_t are the yield stress and tangent modulus of the FGM, respectively.

2.3. Shape functions

2.3.1. Classical formulation

In the classical formulation for shape functions, linear functions $N_{u1} = \frac{L-x}{L}$ and $N_{u2} = \frac{x}{L}$ are used to interpolate the axial displacement *u* while the Hermite polynomials are applied for interpolation of transverse displacement *w* and rotation *θ*. Steps to build the Hermite shape functions are as follows:

Nodal vector $\{\mathbf{q}\} = \{w_1 \quad \theta_1 \quad w_2 \quad \theta_2\}^T$

Length *L* of the beam is scaled to *1* using scaling parameter *s*:

$$\begin{aligned} s &= \frac{x - x_1}{L} \\ ds &= \frac{1}{L}dx \end{aligned} \tag{2.51}$$

The deflection curve *w*(*s*) in terms of *s* by using cubic functions can be written as

$$w(s) = a_0 + a_1 s + a_2 s^2 + a_3 s^3 \tag{2.52}$$

The rotation

$$\theta = \frac{dw}{dx} = \frac{dw}{ds}\frac{ds}{dx} = \frac{1}{L}\left(a_1 + 2a_2 s + 3a_3 s^2\right) \tag{2.53}$$

Applying boundary conditions

$$\begin{aligned} &w(0) = w_1, \quad w(L) = w_2 \\ &\frac{dw}{dx}(0) = \theta_1, \quad \frac{dw}{dx}(L) = \theta_2 \end{aligned} \tag{2.54}$$

we have

$$\begin{aligned} w_1 &= w(0) = a_0 \\ \theta_1 &= \frac{dw}{dx}(0) = \frac{1}{L} a_1 \\ w_1 &= w(L) = a_0 + a_1 + a_2 + a_3 \\ \theta_1 &= \frac{dw}{dx}(L) = \frac{1}{L}\left(a_1 + 2a_2 + 3a_3\right) \end{aligned} \tag{2.55}$$

Expressing four coefficients (a_i, i=0..3) in nodal terms, one can obtain

$$\begin{aligned} a_0 &= w_1 \\ a_1 &= L\theta_1 \\ a_2 &= -3w_1 - 2L\theta_1 + 3w_2 - L\theta_2 \\ a_3 &= 2w_1 + L\theta_1 - 2w_2 + L\theta_2 \end{aligned} \tag{2.56}$$

Replacing back into $w(s)$

$$\begin{aligned} w(s) = (1 - 3s^2 + 2s^3)w_1 + L(s - 2s^2 + s^3)\theta_1 \\ + (3s^2 - 2s^3)w_2 + L(-s^2 + s^3)\theta_2 \end{aligned} \tag{2.57}$$

or one can rewrite

$$w(s) = \left[N_1(s) \quad N_2(s) \quad N_3(s) \quad N_4(s)\right] \begin{Bmatrix} w_1 \\ \theta_1 \\ w_2 \\ \theta_2 \end{Bmatrix} \tag{2.58}$$

where $N_i(s)$, (i=1..4) are called Hermite shape functions:

$$\begin{aligned} N_1(s) &= 1 - 3s^2 + 2s^3 \\ N_2(s) &= L(s - 2s^2 + s^3) \\ N_3(s) &= 3s^2 - 2s^3 \\ N_4(s) &= L(-s^2 + s^3) \end{aligned} \tag{2.59}$$

2.3.2 Tapered prismatic beam

Non-uniform (tapered) beam elements have been used widely in different types of engineering structures, such as high-rise buildings, bridges, ships and aircraft that are subject to static and dynamic loadings. The advantage of using such members is to achieve a better distribution of strengths and weights and very often to satisfy architectural and functional requirements. The beam element considered in this sub-section is a linearly solid rectangular tapered beam with its cross-section varying continuously along the length of the beam (Fig. 2.7).

The equations used to vary linearly the width and heights of the beam are defined as follows:

$$\begin{aligned} b(x) &= m + nx, \quad 0 \le x \le L \\ h(x) &= p + qx, \quad 0 \le x \le L \end{aligned} \tag{2.60}$$

Parameters n and q are the linear rates of changes in the width and height of the cross-section along the beam x-axis, where L is the total length of the beam.

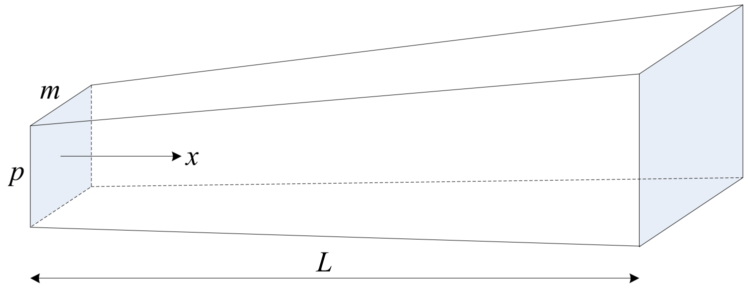

Figure 2.7: Linearly tapered beam cross-section

The Euler–Lagrange equations for the Timoshenko beams are accordingly

$$\frac{\partial}{\partial x}\left(EA(x)\frac{\partial u}{\partial x} \right) = 0 \tag{2.61}$$

$$\frac{\partial}{\partial x}\left(\kappa GA(x)\left(\frac{\partial w}{\partial x} - \theta \right) \right) = 0 \tag{2.62}$$

$$\frac{\partial}{\partial x}\left(EI(x)\frac{\partial \theta}{\partial x} \right) + \kappa GA(x)\left(\frac{\partial w}{\partial x} - \theta \right) = 0 \tag{2.63}$$

where $A(x)$ and $I(x)$ are respectively the cross-section area and moment of inertia linearly varying in the *x* direction.

Integrating Eq. (2.61) results in

$$EA(x)\frac{\partial u}{\partial x}=k_1 \tag{2.64}$$

where k_1 is an integration constant. Solving for $u(x)$,

$$\begin{aligned}u(x)&=\int\frac{k_1}{EA(x)}\\&=\frac{k_1}{E}\int\frac{dx}{A(x)}\\&=\frac{k_1}{E}\int\frac{dx}{(m+nx)(p+qx)}\\&=\frac{k_1}{E}\frac{\ln(m+nx)-\ln(p+qx)}{np-mq}+k_2\end{aligned} \tag{2.65}$$

Replacing the natural logarithmic term by using the Taylor series expanded at $x=L$ up to the quadratic terms,

$$\ln(m+nx)=\ln(m+nL)+\frac{n(x-L)}{m+nL}-\frac{n^2(x-L)^2}{2(m+nL)^2}+O[x]^3$$

$$\ln(p+qx)=\ln(p+qL)+\frac{q(x-L)}{p+qL}-\frac{q^2(x-L)^2}{2(p+qL)^2}+O[x]^3$$

and further, applying the boundary conditions at the two end nodes of the beam, where $u(0)=u_1$, $u(L)=u_2$.

Solving for k_1, k_2 and substituting back to Eq. (2.65), the second-order shape functions for the axial displacement of the beam can be obtained as

$$u(x)=\begin{bmatrix}N_{u1} & N_{u2}\end{bmatrix}\begin{Bmatrix}u_1\\u_2\end{Bmatrix} \tag{2.66}$$

For the sake of simplicity, the axial displacement shape functions and their k^{th}order derivatives (k = *0, 1, 2*) of the linear tapered beam varying in height and/or width can be given in a series form as α:

$$\frac{d^k}{dx^k}(N_{ui}) = \frac{1}{\alpha L^k}\sum_{i=1}^{2}\sum_{j=k}^{2}\left\{\frac{j!}{(j-k)!}R_{uij}\left(\frac{x}{L}\right)^{(j-k)}\right\} \tag{2.67}$$

where α is a constant defined from the taper coefficients (for a uniform section $n = 0$, $q = 0$, $\alpha = 2m^2p^2$); R_{uij} is the axial shape function coefficient corresponding to the i-th node and the j-th nodal displacement.

In order to obtain the transverse displacement and rotation shape functions, we use Eqs. (2.62) and (2.63). The solution of Eq. (2.62) can be obtained from

$$\kappa GA(x)\left(\frac{\partial w}{\partial x} - \theta\right) = c_1 \tag{2.68}$$

Accordingly, Eq. (2.63) can be written as

$$\frac{\partial}{\partial x}\left(EI(x)\frac{\partial \theta}{\partial x}\right) + c_1 = 0 \tag{2.69}$$

where c_1 is an integration constant.

By integrating Eq. (2.69) and using Eq. (2.60), the beam axis rotation equation can be obtained from the following derivation:

$$\begin{aligned} &EI(x)\frac{\partial \theta}{\partial x} = -c_1 x + c_2 \\ &\frac{\partial \theta}{\partial x} = -\frac{c_1}{E}\frac{12x}{(m+nx)(p+qx)^3} + \frac{c_2}{E}\frac{12}{(m+nx)(p+qx)^3} \\ &\theta(x) = -\frac{c_1}{E}\int \frac{12x}{(m+nx)(p+qx)^3}dx + \frac{c_2}{E}\int \frac{12}{(m+nx)(p+qx)^3}dx + c_3 \end{aligned} \tag{2.70}$$

where c_2 and c_3 are integration constants.

The transverse displacement can be derived by integrating Eq. (2.68) and using Eq. (2.60) together with Eq. (2.70), which results in the following expression:

$$\begin{aligned} &\frac{\partial w}{\partial x} = \theta(x) + \frac{c_1}{\kappa G}\frac{1}{A(x)} = \theta(x) + \frac{c_1}{\kappa G}\frac{1}{(m+nx)(p+qx)} \\ &w(x) = \int \theta(x)dx + \frac{c_1}{\kappa G}\int \frac{1}{(m+nx)(p+qx)}dx + c_4 \end{aligned} \tag{2.71}$$

where c_4 is an integration constant.

Applying the boundary conditions at the two end nodes of the beam to the shape functions,

$$w(x=0) = w_1$$

$$\theta(x=0) = \theta_1$$

$$w(x=L) = w_2$$

$$\theta(x=L) = \theta_2$$

Replacing the natural logarithmic terms in both Eqs. (2.70) and (2.71) by using the quadratic and cubic Taylor series expansions respectively, and after several substitutions, the following expression for shape functions can be obtained:

$$w(x) = \left[N_{w1} \quad N_{w2} \quad N_{w3} \quad N_{w4} \right] \begin{Bmatrix} w_1 \\ \theta_1 \\ w_2 \\ \theta_2 \end{Bmatrix} \tag{2.72}$$

$$\theta(x) = \left[N_{\theta 1} \quad N_{\theta 2} \quad N_{\theta 3} \quad N_{\theta 4} \right] \begin{Bmatrix} w_1 \\ \theta_1 \\ w_2 \\ \theta_2 \end{Bmatrix} \tag{2.73}$$

In compact matrices summation forms, the shape functions can be defined as follows:

$$\frac{d^k}{dx^k}(N_{wi}) = \frac{1}{\gamma L^k} \sum_{i=1}^{4} \sum_{j=k}^{3} \left\{ \frac{j!}{(j-k)!} R_{wij} \left(\frac{x}{L} \right)^{(j-k)} \right\} \tag{2.74}$$

$$\frac{d^k}{dx^k}(N_{\theta i}) = \frac{1}{\gamma L^k} \sum_{i=1}^{4} \sum_{j=k}^{3} \left\{ \frac{j!}{(j-k)!} R_{\theta ij} \left(\frac{x}{L} \right)^{(j-k)} \right\} \tag{2.75}$$

where γ is a constant defined from the taper coefficients (for a uniform section $n=0$, $p=0$, $\gamma = 12(1+\phi)m^3p^3$; R_{wij} and $R_{\theta ij}$ are respectively the transverse and rotation shape function coefficients corresponding to the *i*-th node and the *j*-th nodal displacement. The following are the coefficient matrices for the shape functions given above:

$$A_i = mp; \; A_{jh} = npl$$

$$A_{jb} = mql; \; A_{jj} = nql^2 \tag{2.76}$$

$$\varphi = \frac{Ep^2}{l^2 \kappa G} \text{ value at } x = 0$$

$$\mathbf{A}^T = \begin{bmatrix} A_i & A_{jb} & A_{jh} & A_{jj} \end{bmatrix}$$

$$\mathbf{A}^2 = \begin{bmatrix} A_i^2 & A^2{}_{jb} & A^2{}_{jh} \end{bmatrix} \tag{2.77}$$

$$\gamma = \mathbf{A}^T . \begin{bmatrix} 12(1+\varphi) & 13\varphi & 7\varphi \\ -24\varphi & -6\varphi & -8\varphi \\ -12\varphi & -8\varphi & -2\varphi \\ 16\varphi & 0 & 0 \end{bmatrix} . \mathbf{A}^2$$

$$\alpha = \mathbf{A}^T . \begin{bmatrix} 2 \\ 3 \\ 3 \\ 4 \end{bmatrix} \tag{2.78}$$

$$\mathbf{R}_{u10} = \alpha$$

$$\mathbf{R}_{u11} = \mathbf{A}^T . \begin{bmatrix} -2 \\ -4 \\ -4 \\ -6 \end{bmatrix}, \quad \mathbf{R}_{u12} = \mathbf{A}^T . \begin{bmatrix} 0 \\ 1 \\ 1 \\ 2 \end{bmatrix} \tag{2.79}$$

$$\mathbf{R}_{u20} = 0, \mathbf{R}_{u21} = -\mathbf{R}_{u11}, \mathbf{R}_{u22} = -\mathbf{R}_{u12}$$

$$
\begin{aligned}
&\mathbf{R}_{w10} = \gamma \\
&\mathbf{R}_{w11} = \mathbf{A}^T.\begin{bmatrix} -12\varphi & 0 & 0 \\ 18\varphi & 0 & 0 \\ 6\varphi & 0 & 0 \\ 0 & 0 & 0 \end{bmatrix}.\mathbf{A}^2 \\
&\mathbf{R}_{w12} = \mathbf{A}^T.\begin{bmatrix} -36 & -9\varphi & -3\varphi \\ 6\varphi & 0 & 0 \\ 6\varphi & 0 & 0 \\ -12\varphi & 0 & 0 \end{bmatrix}.\mathbf{A}^2 \\
&\mathbf{R}_{w13} = \mathbf{A}^T.\begin{bmatrix} 24 & -4\varphi & -4\varphi \\ 0 & 6\varphi & 8\varphi \\ 0 & 8\varphi & 2\varphi \\ -4\varphi & 0 & 0 \end{bmatrix}.\mathbf{A}^2
\end{aligned}
\tag{2.80}
$$

$$
\begin{aligned}
&\mathbf{R}_{w20} = 0 \\
&\mathbf{R}_{w21} = \mathbf{A}^T.\begin{bmatrix} 6(2+\varphi)l & 13\varphi l & 7\varphi l \\ -12\varphi l & -6\varphi l & -8\varphi l \\ -8\varphi l & -8\varphi l & -2\varphi l \\ 16\varphi l & 0 & 0 \end{bmatrix}.\mathbf{A}^2 \\
&\mathbf{R}_{w22} = \mathbf{A}^T.\begin{bmatrix} -6(4+\varphi)l & -8\varphi l & -4\varphi l \\ 6\varphi l & 0 & 0 \\ 6\varphi l & 0 & 0 \\ -10\varphi l & 0 & 0 \end{bmatrix}.\mathbf{A}^2 \\
&\mathbf{R}_{w23} = \mathbf{A}^T.\begin{bmatrix} 12l & -5\varphi l & -3\varphi l \\ 6\varphi l & 6\varphi l & 8\varphi l \\ 2\varphi l & 8\varphi l & 2\varphi l \\ -6\varphi l & 0 & 0 \end{bmatrix}.\mathbf{A}^2
\end{aligned}
\tag{2.81}
$$

$$\mathbf{R}_{w30} = 0, \mathbf{R}_{w31} = -\mathbf{R}_{w11}, \mathbf{R}_{w32} = -\mathbf{R}_{w12}, \mathbf{R}_{w33} = -\mathbf{R}_{w13}$$

$$
\begin{gathered}
\mathbf{R}_{w40} = 0 \\
\mathbf{R}_{w41} = \mathbf{A}^T . \begin{bmatrix} -6\varphi l & 0 & 0 \\ 6\varphi l & 0 & 0 \\ 2\varphi l & 0 & 0 \\ 0 & 0 & 0 \end{bmatrix} . \mathbf{A}^2 \\
\mathbf{R}_{w42} = \mathbf{A}^T . \begin{bmatrix} 6(-2+\varphi)l & -\varphi l & \varphi l \\ 0 & 0 & 0 \\ 0 & 0 & 0 \\ -2\varphi l & 0 & 0 \end{bmatrix} . \mathbf{A}^2 \\
\mathbf{R}_{w43} = \mathbf{A}^T . \begin{bmatrix} 12l & \varphi l & -\varphi l \\ -6\varphi l & 0 & 0 \\ -2\varphi l & 0 & 0 \\ \varphi l & 0 & 0 \end{bmatrix} . \mathbf{A}^2 \\
\mathbf{R}_{\theta 10} = 0, \mathbf{R}_{\theta 12} = -\mathbf{R}_{\theta 11} \\
\mathbf{R}_{\theta 11} = \mathbf{A}^T . \begin{bmatrix} -72/l & 0 & 0 \\ 0 & 0 & 0 \\ 0 & 0 & 0 \\ 0 & 0 & 0 \end{bmatrix} . \mathbf{A}^2 \\
\mathbf{R}_{\theta 20} = \gamma \\
\mathbf{R}_{\theta 21} = \mathbf{A}^T . \begin{bmatrix} -12(4+\varphi)l & -4\varphi & -4\varphi \\ 6\varphi & 0 & 0 \\ 6\varphi & 0 & 0 \\ -4\varphi & 0 & 0 \end{bmatrix} . \mathbf{A}^2 \\
\mathbf{R}_{\theta 22} = \mathbf{A}^T . \begin{bmatrix} 36 & -9\varphi & -3\varphi \\ 18\varphi & 6\varphi & 8\varphi \\ 6\varphi & 8\varphi & 2\varphi \\ -12\varphi & 0 & 0 \end{bmatrix} . \mathbf{A}^2 \\
\mathbf{R}_{\theta 30} = 0, \mathbf{R}_{\theta 31} = -\mathbf{R}_{\theta 11}, \mathbf{R}_{\theta 32} = \mathbf{R}_{\theta 11}, \mathbf{R}_{\theta 40} = 0
\end{gathered}
\tag{2.82}
$$

$$\mathbf{R}_{\theta 41} = \mathbf{A}^{T}.\begin{bmatrix} -12(-2+\varphi)l & 4\varphi & 4\varphi \\ -6\varphi & 0 & 0 \\ -6\varphi & 0 & 0 \\ 4\varphi & 0 & 0 \end{bmatrix}.\mathbf{A}^{2}$$

$$\mathbf{R}_{\theta 42} = \mathbf{A}^{T}.\begin{bmatrix} 36 & 9\varphi & 3\varphi \\ -18\varphi & -6\varphi & -8\varphi \\ -6\varphi & -8\varphi & -2\varphi \\ 12\varphi & 0 & 0 \end{bmatrix}.\mathbf{A}^{2} \tag{2.83}$$

2.3.3 Axially FGM beam

A beam, with total length L and rectangular cross-section, formed from two different materials, is considered.

Figure 2.8: Two-node-six-degrees-of-freedom beam element

The effective properties P (Young's modulus, shear modulus and mass density) of the beam materials are assumed to vary linearly in the longitudinal direction as

$$P(x) = P_0\left(1 + \frac{n-1}{L}x\right) \tag{2.84}$$

where P_0 stands for the effective properties at the right end of the beam, and n is the ratio between the effective properties at the right end and those at the left end.

The Euler–Lagrange equations for the uniform FGM Timoshenko beams are accordingly

$$\frac{\partial}{\partial x}\left(E(x)A\frac{\partial u}{\partial x}\right) = 0 \tag{2.85}$$

$$\frac{\partial}{\partial x}\left(\kappa G(x)A\left(\frac{\partial w}{\partial x} - \theta\right)\right) = 0 \tag{2.86}$$

$$\frac{\partial}{\partial x}\left(E(x)I\frac{\partial \theta}{\partial x}\right) + \kappa G(x)A\left(\frac{\partial w}{\partial x} - \theta\right) = 0 \tag{2.87}$$

Integrating Eq. (2.85) results in

$$E(x)A\frac{\partial u}{\partial x} = k_1 \tag{2.88}$$

where k_1 is an integration constant. Solving for $u(x)$,

$$\begin{aligned} u(x) &= \frac{1}{A}\int \frac{k_1}{E(x)}dx + k_2 \\ &= k_2 + \frac{k_1 L \ln\left[L+(n-1)x\right]}{AE_0(n-1)} \end{aligned} \tag{2.89}$$

Applying the boundary conditions at the two end nodes of the beam, where *u|x=0 = u1, u|x=L = u2.*

Solving for k_1, k_2 and substituting into Eq. (2.95), the shape functions for the axial displacement of the beam can be obtained as

$$u(x) = \left[N_{u1} \quad N_{u2}\right]\begin{Bmatrix} u_1 \\ u_2 \end{Bmatrix} \tag{2.90}$$

where

$$N_{u1} = \frac{(L-x)(L+Ln+x-nx)}{L^2(n+1)} \tag{2.91}$$

$$N_{u2} = \frac{x(2Ln+x-nx)}{L^2(n+1)} \tag{2.92}$$

It can be concluded from Eqs. (2.86) and (2.87) that the transverse displacement is one order higher than the rotation. Hence, the transverse displacement and rotation are assumed in polynomial equations as follows:

$$\theta(x) = b_0 + b_1 x + b_2 x^2 \tag{2.93}$$

$$w(x) = a_0 + a_1 x + a_2 x^2 + a_3 x^3 \tag{2.94}$$

The solution of Eq. (2.86) can be obtained from

$$\kappa G(x) A\left(\frac{\partial w}{\partial x} - \theta\right) = c_1 \tag{2.95}$$

Accordingly, Eq. (2.87) can be written as

$$\frac{\partial}{\partial x}\left(E(x) I \frac{\partial \theta}{\partial x}\right) + c_1 = 0 \tag{2.96}$$

By integrating Eq. (2.96) and substituting back to Eq. (2.86), the beam axis rotation equation can be obtained from the following derivation:

$$\begin{aligned} &E(x)I\frac{\partial\theta}{\partial x} = -c_1 x + c_2 \\ &\frac{\partial\theta}{\partial x} = -\frac{c_1}{I}\frac{x}{E(x)} + \frac{c_2}{I}\frac{1}{E(x)} \\ &\theta(x) = -\frac{c_1}{I}\int\frac{xdx}{E(x)} + \frac{c_2}{I}\int\frac{dx}{E(x)} + c_3 \end{aligned} \tag{2.97}$$

The transverse displacement can be derived by substitution of Eq. (2.95) into Eq. (2.93), which results in the following expression:

$$\begin{aligned} &\frac{\partial w}{\partial x} = \theta(x) + \frac{c_1}{\kappa A}\frac{1}{G(x)} \\ &w(x) = \int\theta(x)dx + \frac{c_1}{\kappa A}\int\frac{1}{G(x)}dx + c_4 \end{aligned} \tag{2.98}$$

Applying the boundary conditions at the two end nodes of the beam to the shape functions,

$$\begin{aligned} &w(x=0) = w_1 \\ &\theta(x=0) = \theta_1 \\ &w(x=L) = w_2 \\ &\theta(x=L) = \theta_2 \end{aligned} \tag{2.99}$$

By replacing the natural logarithmic terms in both Eqs. (2.97) and (2.98) using a cubic Taylor series expansion, and after several substitutions, the following expressions for shape functions can be obtained:

$$w(x) = \begin{bmatrix} N_{w1} & N_{w2} & N_{w3} & N_{w4} \end{bmatrix} \begin{Bmatrix} w_1 \\ \theta_1 \\ w_2 \\ \theta_2 \end{Bmatrix} \tag{2.100}$$

$$\theta(x)=\left[N_{\theta 1}\quad N_{\theta 2}\quad N_{\theta 3}\quad N_{\theta 4}\right]\begin{Bmatrix} w_1 \\ \theta_1 \\ w_2 \\ \theta_2 \end{Bmatrix} \tag{2.101}$$

where

$$\begin{aligned}
N_{w1} &= \frac{\begin{array}{c}(L-x)(3(1+n)^2(L-x)(L+2x)+(4L^2(1+n+n^2) \\ +L(1+(4-5n)n)x+4(n-1)^2x^2)\phi)\end{array}}{(L^3(3(1+n)^2+(4(1+n+n^2))\phi))} \\
N_{w2} &= \frac{\begin{array}{c}(L-x)x(3(1+n)^3(L-x) \\ +(L(2+n(7+n(2+n)))-(4(n-1))x)\phi)\end{array}}{(L^2(3(1+n)^3+(4(1+n))(1+n+n^2)\phi))} \\
N_{w3} &= \frac{\begin{array}{c}x(3(1+n)^2(3L-2x)x+(L^2(3+9n^2) \\ -3L(n-1)(-1+3n)x+4(n-1)^2x^2)\phi)\end{array}}{(L^3(3(1+n)^2+(4(1+n+n^2))\phi))} \\
N_{w4} &= \frac{\begin{array}{c}-(L-x)x(3(1+n)^3x+L(1+2n)(1+3n^2)\phi \\ -(4(n-1))n^2x\phi)\end{array}}{(L^2(3(1+n)^3+(4(1+n))(1+n+n^2)\phi))}
\end{aligned} \tag{2.102}$$

$$\begin{aligned}
N_{\theta 1} &= \frac{-18(1+n)^2(L-x)x}{(L^3(3(1+n)^2+(4(1+n+n^2))\phi))} \\
N_{\theta 2} &= \frac{\begin{array}{c}(L-x)(3(1+n)^3(L-3x) \\ +(4(1+n+n^2))(L+Ln+x-nx)\phi)\end{array}}{L^2(3(1+n)^3+(4(1+n))(1+n+n^2)\phi)} \\
N_{\theta 3} &= \frac{18(1+n)^2(L-x)x}{L^3(3(1+n)^2+(4(1+n+n^2))\phi)} \\
N_{\theta 4} &= \frac{\begin{array}{c}3(1+n)^3x(-2L+3x) \\ +(4(1+n+n^2))x(2Ln+x-nx)\phi\end{array}}{L^2(3(1+n)^3+(4(1+n))(1+n+n^2)\phi)}
\end{aligned} \tag{2.103}$$

in which $\phi=\frac{12}{l^2}\frac{E_0 I}{\kappa G_0 A}$ where A, I are the cross-section area and moment of inertia of the uniform beam, while E_0, G_0 are the Young's and shear moduli of the material at the left end of the FGM beam. In the homogeneous case (*n=1*) the shape functions recover linear and Kosmatka functions.

2.3.4 Thickness direction of FGM beam

Following the idea put forward by Kosmatka [69] that the shape functions can be obtained by solving the governing differential equations of a homogeneous Timoshenko beam segment, here the shape functions for the displacements and the rotation are derived by solving the static part of the governing differential equations, namely

$$\begin{aligned}
&A_{11}\frac{\partial^2 u}{\partial x^2}-A_{12}\frac{\partial^2 \theta}{\partial x^2}=0\\
&\kappa A_{33}\left(\frac{\partial^2 w}{\partial x^2}-\frac{\partial \theta}{\partial x}\right)=0 \qquad (2.104)\\
&A_{12}\frac{\partial^2 u}{\partial x^2}-A_{22}\frac{\partial^2 \theta}{\partial x^2}-\kappa A_{33}\left(\frac{\partial w}{\partial x}-\theta\right)=0
\end{aligned}$$

The solutions of Eq. (2.104) can be easily obtained with the aid of a symbolic software, for example by using the "*dsolve*" command in Maple [39] one can get the solutions of Eq. (2.104) in the forms

$$\begin{aligned}
&u=\frac{1}{2}C_4\alpha x^2+C_5\alpha x+C_1x+C_6\alpha+C_2\\
&w=\frac{1}{6}C_4x^3+\frac{1}{2}C_5x^2+C_6x-C_4(\beta+\lambda)x+C_3 \qquad (2.105)\\
&\theta=\frac{1}{2}C_4x^2+C_5x+C_6
\end{aligned}$$

where

$$\begin{aligned}
&\alpha=\frac{A_{12}}{A_{11}},\ \beta=\frac{A_{22}}{A_{33}},\ \lambda=\frac{A^2{}_{12}}{A_{11}A_{33}}\\
&\left(A_{11},A_{12},A_{22}\right)=\int_A E(z)(1,z,z^2)dA \qquad (2.106)\\
&A_{33}=\int_A G(z)dA
\end{aligned}$$

The constants C_i *(i=1:6)* in Eq. (2.105) can be determined from the following element end conditions: $u = u_1,\ w = w_1,\ \theta = \theta_1$ at $x = 0$ and $u = u_2,\ w = w_2,\ \theta = \theta_2$ at $x = L$. The shape functions obtained are given in the forms

$$N_{u1} = -\frac{x}{L} + 1, \quad N_{u4} = \frac{x}{L}$$

$$N_{u2} = \frac{6\alpha\left(\frac{x^2}{L^2} - \frac{x}{L}\right)}{L(1+\phi)}, \quad N_{u5} = -\frac{6\alpha\left(\frac{x^2}{L^2} - \frac{x}{L}\right)}{L(1+\phi)} \tag{2.107}$$

$$N_{u3} = N_{u6} = \frac{3\alpha\left(\frac{x^2}{L^2} - \frac{x}{L}\right)}{L(1+\phi)}$$

$$N_{w1} = N_{w4} = 0$$

$$N_{w2} = \frac{1}{1+\phi}\left(2\frac{x^3}{L^3} - 3\frac{x^2}{L^2} - \phi\frac{x}{L} + 1 + \phi\right)$$

$$N_{w3} = \frac{L}{1+\phi}\left[\frac{x^3}{L^3} - \left(2 + \frac{1}{2}\phi\right)\frac{x^2}{L^2} + \left(2 + \frac{1}{2}\phi\right)\frac{x}{L}\right] \tag{2.108}$$

$$N_{w5} = -\frac{1}{1+\phi}\left(2\frac{x^3}{L^3} - 3\frac{x^2}{L^2} - \phi\frac{x}{L}\right)$$

$$N_{w6} = \frac{L}{1+\phi}\left[\frac{x^3}{L^3} - \left(1 - \frac{1}{2}\phi\right)\frac{x^2}{L^2} - \frac{1}{2}\phi\frac{x}{L}\right]$$

$$N_{\theta1} = N_{\theta4} = 0$$

$$N_{\theta2} = \frac{6}{L(1+\phi)}\left(\frac{x^2}{L^2} - \frac{x}{L}\right)$$

$$N_{\theta3} = \frac{L}{1+\phi}\left[3\frac{x^2}{L^2} - (4+\phi)\frac{x}{L} + 1 + \phi\right] \tag{2.109}$$

$$N_{\theta5} = -\frac{6}{L(1+\phi)}\left(\frac{x^2}{L^2} - \frac{x}{L}\right)$$

$$N_{\theta6} = \frac{L}{1+\phi}\left[3\frac{x^2}{L^2} - (2-\phi)\frac{x}{L}\right]$$

where $\phi = \frac{12(\beta - \lambda)}{L^2}$.

2.3.5 Exact shape functions for non-prismatic FGM beam

The Euler–Lagrange equations for the Timoshenko non-prismatic FGM beam are accordingly

$$\frac{\partial}{\partial x}\left(E(x)A(x)\frac{\partial u}{\partial x}\right)=0 \tag{2.110}$$

$$\frac{\partial}{\partial x}\left(\kappa G(x)A(x)\left(\frac{\partial w}{\partial x}-\theta\right)\right)=0 \tag{2.111}$$

$$\frac{\partial}{\partial x}\left(E(x)I(x)\frac{\partial \theta}{\partial x}\right)+\kappa G(x)A(x)\left(\frac{\partial w}{\partial x}-\theta\right)=0 \tag{2.112}$$

Integrating Eq. (2.110) results in

$$E(x)A(x)\frac{\partial u}{\partial x}=k_1 \tag{2.113}$$

where k_1 is an integration constant. Solving for *u(x)*,

$$u(x)=k_1\int\frac{1}{E(x)A(x)}dx+k_2=k_1f_1+k_2 \tag{2.114}$$

where

$$f_1=\int\frac{1}{E(x)A(x)}dx \tag{2.115}$$

Applying the boundary conditions at the two end nodes of the beam, where $u(0) = u_1$, $u(L) = u_2$.

Solving for k_1, k_2 and substituting back to Eq. (2.113), the exact shape functions and the first order derivative of the axial displacement of the beam can be obtained as

$$\begin{gathered}
u(x)=\begin{bmatrix}N_{u1} & N_{u2}\end{bmatrix}\begin{Bmatrix}u_1\\ u_2\end{Bmatrix}\\
N_{u1}=\frac{f_1-f_{1L}}{f_{10}-f_{1L}},\ N_{u2}=\frac{-f_1+f_{10}}{f_{10}-f_{1L}}\\
\frac{dN_{u1}}{dx}=\frac{f_1'}{f_{10}-f_{1L}},\ \frac{dN_{u2}}{dx}=\frac{-f_1'}{f_{10}-f_{1L}}
\end{gathered} \tag{2.116}$$

where $f_{10} = f_1\big|_{x=0}$, $f_{1L} = f_1\big|_{x=L}$

The transverse displacement is assumed in the polynomial equation as follows:

$$\begin{aligned} w(x) &= a_0 + a_1 x + \frac{a_2}{2}x^2 + \frac{a_3}{6}x^3 \\ \frac{\partial w}{\partial x} &= a_1 + a_2 x + \frac{a_3}{2}x^2 \end{aligned} \tag{2.117}$$

$$\frac{\partial^2 w}{\partial x^2} = a_2 + a_3 x \tag{2.118}$$

The solution of Eq. (2.111) can be obtained from

$$\begin{aligned} &\kappa G(x)A(x)\left(\frac{\partial w}{\partial x} - \theta\right) = c_1 \\ &w(x) = c_1 f_4 + \int \theta(x)dx + c_4 \\ &\theta(x) = -c_1 \frac{1}{\kappa G(x)A(x)} + \frac{\partial w}{\partial x} \end{aligned} \tag{2.119}$$

Replacing Eq. (2.117) into Eq. (2.119),

$$\begin{aligned} \theta(x) &= -c_1 f_4' + a_1 + a_2 x + \frac{a_3}{2}x^2 \\ \frac{\partial \theta}{\partial x} &= -c_1 f_4'' + a_2 + a_3 x \\ \frac{\partial^2 \theta}{\partial x^2} &= -c_1 f_4''' + a_3 \end{aligned} \tag{2.120}$$

Replacing Eq. (2.120) into Eq. (2.119),

$$\begin{aligned} w(x) &= c_1 f_4 + \int \theta(x)dx + c_4 \\ &= c_1 f_4 + \int\left(-c_1 f_4' + a_1 + a_2 x + \frac{a_3}{2}x^2\right)dx + c_4 \\ &= a_1 x + \frac{a_2}{2}x^2 + \frac{a_3}{6}x^3 + c_4 \end{aligned} \tag{2.121}$$

Accordingly, Eq. (2.112) can be written as

$$\begin{aligned}
&\frac{\partial}{\partial x}\left(E(x)I(x)\frac{\partial\theta}{\partial x}\right)+c_1=0\\
&\frac{\partial\theta}{\partial x}=-c_1\frac{x}{E(x)I(x)}+c_2\frac{1}{E(x)I(x)}=-c_1f_3'+c_2f_2'\\
&\theta(x)=-c_1f_3+c_2f_2+c_3\\
&\frac{\partial^2\theta}{\partial x^2}=-c_1f_3''+c_2f_2''
\end{aligned}\tag{2.122}$$

where $c_i\ (i=1,2,3,4)$ and $a_i\ (i=1,2,3,4)$ are constants,

$$\begin{aligned}
f_2&=\int\frac{1}{E(x)I(x)}dx\\
f_3&=\int\frac{x}{E(x)I(x)}dx\\
f_4&=\int\frac{1}{\kappa G(x)A(x)}dx
\end{aligned}$$

Comparing the rotation and its derivatives from Eq. (2.119) and Eq. (2.122), as well as the transverse displacement between Eq. (2.117) and Eq. (2.121), we have the relationship between a_i and c_i :

$$\begin{aligned}
\{\mathbf{a}\}&=\{\mathbf{M_{ac}}\}\{\mathbf{c}\}\\
\{\mathbf{c}\}&=\{\mathbf{M_{ac}}\}^{-1}\{\mathbf{a}\}
\end{aligned}\tag{2.123}$$

Applying boundary conditions at the two end nodes of the beam where $w(x=0)=w_1,\ w(x=L)=w_2$ and $\theta(x=0)=\theta_1,\ \theta(x=L)=\theta_2$,

$$\begin{Bmatrix} w_1\\ \theta_1\\ w_2\\ \theta_2 \end{Bmatrix}=\{M_{w\theta c}\}\begin{Bmatrix} c_1\\ c_2\\ c_3\\ c_4 \end{Bmatrix}\tag{2.124}$$

or

$$\begin{Bmatrix} c_1\\ c_2\\ c_3\\ c_4 \end{Bmatrix}=\{M_{w\theta c}\}^{-1}\begin{Bmatrix} w_1\\ \theta_1\\ w_2\\ \theta_2 \end{Bmatrix}\tag{2.125}$$

By replacing c_i, the expressions for the transverse and rotational shape functions can be obtained:

$$w(x) = \begin{bmatrix} N_{w1} & N_{w2} & N_{w3} & N_{w4} \end{bmatrix} \begin{Bmatrix} w_1 \\ \theta_1 \\ w_2 \\ \theta_2 \end{Bmatrix} \tag{2.126}$$

$$\theta(x) = \begin{bmatrix} N_{\theta 1} & N_{\theta 2} & N_{\theta 3} & N_{\theta 4} \end{bmatrix} \begin{Bmatrix} w_1 \\ \theta_1 \\ w_2 \\ \theta_2 \end{Bmatrix} \tag{2.127}$$

In summary, the detailed transverse and rotational shape functions and their derivatives are expressed as follows:

$$\begin{aligned} \Phi = {} & (f_{30} - f_{3L}) L(-3 f'_{2L} + f''_{2L} L) \\ & + f_{2L}(-6 f'_{4L} + L(-3 f'_{3L} + 3 f''_{4L} + f''_{3L} L - f'''_{4L} L)) \\ & + f_{20}(6 f'_{4L} + L(3 f'_{3L} - 3 f''_{4L} - f''_{3L} L + f'''_{4L} L)) \end{aligned} \tag{2.128}$$

$$N_{w1} = \frac{1}{\Phi L} \begin{bmatrix} x(f_{20} - f_{2L}) \begin{pmatrix} 3 f''_4 x + 6 f_3 - 6 f'_4 \\ -3 f'_3 x + f''_3 x^2 - f'''_4 x^2 \end{pmatrix} \\ -6x(f_{20} f_{3L} + f_{2L} f_{30}) - \Phi \\ -(f_{30} - f_{3L})(6 f_2 x - 3 f'_2 x^2 + f''_2 x^3) \\ \end{bmatrix} \tag{2.129}$$

$$N_{w2}=-\frac{1}{6\Phi}\begin{bmatrix}(3f_2'x-f_2''x^2)\begin{pmatrix}-6f_{4L}'-3f_{3L}'L\\+3f_{4L}''L+f_{3L}''L^2\\-f_{4L}'''L^2\end{pmatrix}\\+6x\begin{pmatrix}-3f_{2L}'f_{3L}+3f_{2L}'f_{3L}L\\+3f_{2L}'f_{4L}'+f_{2L}''f_3L^2\\-f_{2L}''f_{3L}L^2-f_{2L}''f_4'L^2\\+f_2(6f_{4L}'+L(3f_{3L}'\\-3f_{4L}''-f_{3L}''L+f_{4L}'''L)\end{pmatrix}\\-6f_{2L}\begin{pmatrix}6f_{4L}'+L(3f_{3L}'-3f_{4L}''\\-f_{3L}''L+f_{4L}'''L)\end{pmatrix}\\+x(3f_{2L}'-f_{2L}'')\begin{pmatrix}3f_{3L}'-3f_{4L}''\\-f_{3L}''x+f_{4L}'''x\end{pmatrix}\end{bmatrix}\tag{2.130}$$

$$N_{w3}=\frac{1}{\Phi L}\begin{bmatrix}x((f_{30}-f_{3L})(6f_2-3f_2'x+f_2''x^2)\\+(f_{2L}-f_{20})(6f_3-6f_4'-3f_3'x+3f_4''x+f_3''x^2-f_4'''x^2)\\+6(f_{20}f_{3L}-f_{2L}f_{30})\end{bmatrix}\tag{2.131}$$

$$N_{w4}=-\frac{x}{6\Phi}\begin{bmatrix}(6f_2+f_2''x^2)\begin{pmatrix}6f_{30}-6f_{3L}\\+6f_{4L}'\\+3f_{3L}'L-3f_{4L}''L\\-f_{3L}''L^2+f_{4L}'''L^2\end{pmatrix}\\+(3f_{2L}'-f_{2L}'')\begin{pmatrix}-6f_{3L}+6f_{30}L\\+6f_{4L}'+3f_{3L}'x\\-3f_{4L}''x-f_{3L}''x^2\\+f_{4L}'''x^2\end{pmatrix}\\+(3f_2'x+6f_{20})\begin{pmatrix}-6f_{4L}'-3f_{3L}'L\\+3f_{4L}''L\\+f_{3L}''L^2-f_{4L}'''L^2\end{pmatrix}\\+6(f_{2L}-f_{20})\begin{pmatrix}6f_3-6f_{3L}\\-6f_4'\\-3f_3'x+3f_4''x\\+f_3''x^2-f_4'''x^2\end{pmatrix}\end{bmatrix}\tag{2.132}$$

$$N_{\theta 1} = \frac{1}{\Phi L}\left[6(f_{2L}(-f_3 + f_{30}) + f_{20}(f_3 - f_{3L}) + f_2(-f_{30} + f_{3L}))\right] \tag{2.133}$$

$$N_{\theta 2} = -\frac{1}{\Phi}\left[\begin{array}{l} (f_3 - f_{3L})L(3f'_{2L} - f''_{2L}L) + f_2(-6f'_{4L} + L(-3f'_{3L} + 3f''_{4L} + \\ f''_{3L}L - f'''_{4L}L)) + f_{2L}(6f'_{4L} + L(3f'_{3L} - 3f''_{4L} - f''_{3L}L + f'''_{4L}L)) \end{array}\right] \tag{2.134}$$

$$N_{\theta 3} = -N_{\theta 1} \tag{2.135}$$

$$N_{\theta 4} = -\frac{1}{\Phi}\left[\begin{array}{l} 6f_{2L}(f_3 - f_{30}) + 6f_2 f_{30} - 6f_2 f_{3L} + 6f_2 f'_{4L} - 3f'_{2L} f_{3L} \\ +3f'_{2L} f_{30} L + 3f_2 f'_{3L} L - 3f_2 f''_{4L} L + f''_{2L} f_3 L^2 - f''_{2L} f_{30} L^2 \\ -f_2 f''_{3L} L^2 + f_2 f'''_{4L} L^2 + f_{20}(-6f_3 + 6f_{3L} - 6f'_{4L} - 3f'_{3L} L \\ +3f''_{4L} L + f''_{3L} L^2 - f'''_{4L} L^2) \end{array}\right] \tag{2.136}$$

$$\frac{\partial N_{w1}}{\partial x} = \frac{1}{\Phi L}\left[\begin{array}{l} 6(f_2(-f_{30} + f_{3L}) + f_{20}(f_3 - f_{3L} - f'_4) \\ +f_{2L}(-f_3 + f_{30} + f'_4)) \end{array}\right] \tag{2.137}$$

$$\frac{\partial N_{w2}}{\partial x} = -\frac{1}{\Phi}\left[\begin{array}{l} (f_3 - f_{3L} - f'_4)L(3f'_{2L} - f''_{2L}L) \\ +f_2\left(\begin{array}{l} -6f'_{4L} + L(-3f'_{3L} \\ +3f''_{4L} + f''_{3L}L - f'''_{4L}L) \end{array}\right) \\ +f_2 L\left(6f'_{4L} + L(3f'_{3L} - 3f''_{4L} - f''_{3L}L + f'''_{4L}L)\right) \end{array}\right] \tag{2.138}$$

$$\frac{\partial N_{w3}}{\partial x} = -\frac{\partial N_{w1}}{\partial x} \tag{2.139}$$

$$\frac{\partial N_{w4}}{\partial x} = -\frac{1}{\Phi}\left[\begin{array}{l} (6f_{2L} - 6f_{20} + f''_{2L})(f_3 - f_{30} - f'_4) \\ +(f_2 - f_{20})\left(\begin{array}{l} 6f'_{4L} + 3f'_{3L}L - 3f''_{4L}L \\ -3f''_{3L}L^2 + 4f'''_{4L}L^2 \end{array}\right) \\ +6f_2(f_{30} - f_{3L}) + 3f'_{2L}\left(-f_{3L} + f_{30}L + f'_{4L}\right) \end{array}\right] \tag{2.140}$$

$$\frac{\partial N_{\theta 1}}{\partial x} = \frac{1}{\Phi L}\left[6((f_{20} - f_{2L})f'_3 + f'_2(-f_{30} + f_{3L}))\right] \tag{2.141}$$

$$\frac{\partial N_{\theta 2}}{\partial x} = \frac{1}{\Phi}\left[\begin{array}{l} f'_2\left(6f'_{4L} + L(3f'_{3L} - 3f''_{4L} - f''_{3L}L + f'''_{4L}L)\right) \\ +f'_{3L}(-3f'_{2L} + f''_{2L}L) \end{array}\right] \tag{2.142}$$

$$\frac{\partial N_{\theta 3}}{\partial x} = -\frac{\partial N_{\theta 1}}{\partial x} \tag{2.143}$$

$$\frac{\partial N_{\theta 4}}{\partial x} = -\frac{1}{\Phi}\left[f_3'\begin{pmatrix} -6f_{20} + 6f_{2L} \\ -3f_{2L}'L + f_{2L}''L^2 \end{pmatrix} + f_2'\begin{pmatrix} 6f_{30} - 6f_{3L} \\ +6f_{4L}' + 3f_{3L}'L \\ -3f_{4L}''L - f_{3L}''L^2 \\ +f_{4L}'''L^2 \end{pmatrix} \right] \tag{2.144}$$

where

$$\begin{aligned}
&f_{20} = f_2\big|_{x=0},\ f_{20}' = f_2'\big|_{x=0},\ f_{20}'' = f_2''\big|_{x=0} \\
&f_{2L} = f_2\big|_{x=L},\ f_{2L}' = f_2'\big|_{x=L},\ f_{2L}'' = f_2''\big|_{x=L} \\
&f_{30} = f_3\big|_{x=0},\ f_{30}' = f_3'\big|_{x=0},\ f_{30}'' = f_3''\big|_{x=0} \\
&f_{3L} = f_3\big|_{x=L},\ f_{3L}' = f_3'\big|_{x=L},\ f_{3L}'' = f_3''\big|_{x=L} \\
&f_{40} = f_4\big|_{x=0},\ f_{40}' = f_4'\big|_{x=0},\ f_{40}'' = f_4''\big|_{x=0} \\
&f_{4L} = f_4\big|_{x=L},\ f_{4L}' = f_4'\big|_{x=L},\ f_{4L}'' = f_4''\big|_{x=L} \\
&f_{40}''' = f_4'''\big|_{x=0},\ f_{4L}''' = f_4'''\big|_{x=L}
\end{aligned} \tag{2.145}$$

Chapter 3: FEM formulation for FGM beam

3.1 Static analysis

The potential energy of an arbitrary point in a Timoshenko beam can be expressed as

$$U=\frac{1}{2}\int_0^L\left[EA\left(\frac{\partial u}{\partial x}\right)^2+EI\left(\frac{\partial\theta}{\partial x}\right)^2+\kappa GA\left(\frac{\partial w}{\partial x}-\theta\right)^2\right]dx$$
$$=\frac{1}{2}\int_0^L\begin{Bmatrix}\dfrac{\partial u}{\partial x}\\ \dfrac{\partial\theta}{\partial x}\\ \dfrac{\partial w}{\partial x}-\theta\end{Bmatrix}^T\begin{bmatrix}EA&0&0\\0&EI&0\\0&0&\kappa GA\end{bmatrix}\begin{Bmatrix}\dfrac{\partial u}{\partial x}\\ \dfrac{\partial\theta}{\partial x}\\ \dfrac{\partial w}{\partial x}-\theta\end{Bmatrix}dx \tag{3.1}$$

The minimum potential energy will give an FEM formulation of a static problem. By substituting shape functions into Eq. (3.1), the following FEM formulation can be obtained in matrix form as

$$\mathbf{KD}=\mathbf{F} \tag{3.2}$$

where

$$\mathbf{F}=\int_0^L\begin{bmatrix}N_u\\N_w\\N_\theta\end{bmatrix}^T\begin{Bmatrix}q_u\\q_w\\m_\theta\end{Bmatrix}dx \tag{3.3}$$

K is the beam stiffness matrix obtained from the element stiffness matrix **k**:

$$\mathbf{k}=\int_0^L\begin{bmatrix}\left[N_{u,x}\right]\\ \left[N_{\theta,x}\right]\\ \left[N_{w,x}\right]-\theta\end{bmatrix}^T\begin{bmatrix}EA&0&0\\0&EI&0\\0&0&\kappa GA\end{bmatrix}\begin{Bmatrix}\left[N_{u,x}\right]\\ \left[N_{\theta,x}\right]\\ \left[N_{w,x}\right]-\theta\end{Bmatrix}dx \tag{3.4}$$

3.2 Free vibration analysis

The strain energy and kinetic energy of a Timoshenko beam element can be given by

$$\begin{aligned}
U &= \frac{1}{2}\int_0^l \int_{A(x)} (E\varepsilon_x^2 + \kappa G\gamma_{xz}^2)dAdx \\
&= \frac{1}{2}\int_0^l \int_{A(x)} \left[E(u_{,x} - z\theta_{,x})^2 + \kappa G(w_{,x} - \theta)^2\right]dAdx \\
&= \frac{1}{2}\int_0^l \left[EA(x)u_{,x}^2 + EI(x)\theta_{,x}^2 + \kappa GA(x)(w_{,x} - \theta)^2\right]dx \\
&= \int_0^l F(u_{,x}, w_{,x}, \theta, \theta_{,x})dx
\end{aligned} \tag{3.5}$$

In the thermal environment in sub-section 2.2.2, there also exists the strain energy from initial stress due to the temperature rise U_T:

$$U_T = \frac{1}{2}\int_0^L N_T \mathrm{w}_{0,x}^2 dx \tag{3.6}$$

where N_T is the axial force resultant caused by elevated temperature, defined as

$$N_T = -\int_A E(z,T)\alpha(z,T)\Delta T dA \tag{3.7}$$

$$\begin{aligned}
T &= \frac{1}{2}\int_0^l \int_{A(x)} \rho(u_{,t}^2 + w_{,t}^2)dAdx \\
&= \frac{1}{2}\int_0^l \int_{A(x)} \left[\rho(u_{,t} - z\theta_{,t})^2 + \rho w_{,t}^2\right]dAdx \\
&= \frac{1}{2}\int_0^l \left[\rho A(x)u_{,t}^2 + \rho I(x)\theta_{,t}^2 + \rho A(x)w_{,t}^2\right]dx \\
&= \int_0^l F(u_{,t}, w_{,t}, \theta_{,t})dx
\end{aligned} \tag{3.8}$$

By applying the principle of stationary total energy to the strain and kinetic energies, stiffness equations can be obtained in a matrix form as

$$\mathbf{M}\ddot{\mathbf{D}} + \mathbf{K}\mathbf{D} = \mathbf{F}_{ex} \tag{3.9}$$

where **K** and **M** are the stiffness matrix and mass matrix of the beam, respectively, obtained by assembling the element stiffness matrix **k** and the mass matrix **m** by the standard procedure of the finite element method; $\mathbf{D}$ and $\ddot{\mathbf{D}}$ denote the structural vectors of nodal displacements and accelerations, respectively; $\mathbf{F}_{ex}$ is the external nodal load vector. In the free vibration analysis, the right-hand side of Eq. (3.9) is set to zero and a harmonic response, $\mathbf{D} = \bar{\mathbf{D}}\sin(\omega t)$ is assumed so that Eq. (3.9) is deduced to an eigenvalue problem as

$$\left(\mathbf{K} - \omega^2 \mathbf{M}\right)\bar{\mathbf{D}} = 0 \tag{3.10}$$

$$\mathbf{k} = \int_0^L \begin{bmatrix} [N_{u,x}] \\ [N_{\theta,x}] \\ [N_{w,x}] - \theta \end{bmatrix}^T \begin{bmatrix} EA & 0 & 0 \\ 0 & EI & 0 \\ 0 & 0 & \kappa GA \end{bmatrix} \begin{Bmatrix} [N_{u,x}] \\ [N_{\theta,x}] \\ [N_{w,x}] - \theta \end{Bmatrix} dx \tag{3.11}$$

$$\mathbf{m} = \int_0^l \begin{bmatrix} [N_u] \\ [N_\theta] \\ [N_w] \end{bmatrix}^T \begin{bmatrix} \rho A(x) & 0 & 0 \\ 0 & \rho A(x) & 0 \\ 0 & 0 & \rho I(x) \end{bmatrix} \begin{Bmatrix} [N_u] \\ [N_\theta] \\ [N_w] \end{Bmatrix} dx \tag{3.12}$$

where ω is the circular frequency and $\bar{\mathbf{D}}$ is the vibration amplitude.

3.3 Dynamic analysis

One can write the strain and kinetic energies for the beam in terms of nodal displacements $\mathbf{d} = \{u_1 \quad w_1 \quad \theta_1 \quad u_2 \quad w_2 \quad \theta_2\}^T$ as

$$U = \frac{1}{2}\sum_{i=1}^{nel} \mathbf{d}^T \mathbf{k} \mathbf{d}$$
$$T = \frac{1}{2}\sum_{i=1}^{nel} \dot{\mathbf{d}}^T \mathbf{m} \dot{\mathbf{d}} \tag{3.13}$$

where **k** and **m** denote the stiffness and mass matrices for the element, respectively:

$$\mathbf{k} = \int_0^L \begin{bmatrix} [N_{u,x}] \\ [N_{\theta,x}] \\ [N_{w,x}] - \theta \end{bmatrix}^T \begin{bmatrix} EA & 0 & 0 \\ 0 & EI & 0 \\ 0 & 0 & \kappa GA \end{bmatrix} \begin{Bmatrix} [N_{u,x}] \\ [N_{\theta,x}] \\ [N_{w,x}] - \theta \end{Bmatrix} dx \tag{3.14}$$

$$\mathbf{m} = \int_0^l \begin{bmatrix} [N_u] \\ [N_\theta] \\ [N_w] \end{bmatrix}^T \begin{bmatrix} \rho A(x) & 0 & 0 \\ 0 & \rho A(x) & 0 \\ 0 & 0 & \rho I(x) \end{bmatrix} \begin{Bmatrix} [N_u] \\ [N_\theta] \\ [N_w] \end{Bmatrix} dx \tag{3.15}$$

Using the derived element matrices, the discrete equations of motion for the beam can be written in the form

$$\mathbf{M}\ddot{\mathbf{D}} + \mathbf{K}\mathbf{D} = \mathbf{F}_{ex} \tag{3.16}$$

where **M**, **K** are structural mass and stiffness matrices obtained from the element ones **m**, **k**, respectively. $\mathbf{F}_{ex}$ is the external nodal load vector.

3.3.1 Beam subjected to a harmonic moving load

The potential of the external moving load can be written in the form

$$V_P = -P_0 \cos(\Omega t) \mathbf{N}_w^T \delta(x - vt) \tag{3.17}$$

The nodal external load vector consists of all zero components, except for those relating to the element currently under loading.

$$\mathbf{F}_{ex} = \begin{bmatrix} 0 \\ 0 \\ 0 \\ \vdots \\ N_{w1} \\ N_{w2} \\ N_{w3} \\ N_{w4} \\ N_{w5} \\ N_{w6} \\ \vdots \\ 0 \\ 0 \\ 0 \end{bmatrix} \tag{3.18}$$

3.3.2 Beam subjected to multiple moving point loads

The potential of the external moving loads has a simple form:

$$V = -\sum_{i=1}^{nload} P_0 \mathbf{N}_w^T \mathbf{d} \delta(x - s_i(t)) \tag{3.19}$$

The nodal external load vector consists of all zero coefficients, except for the elements currently under loading. In addition, the interpolation functions $N_{w|xi}$ are evaluated at the current position of the i-th load.

$$\mathbf{F}_{ex} = \begin{bmatrix} 0 \\ 0 \\ 0 \\ \vdots \\ 0 \\ 0 \\ \vdots \\ N_{w|x_n} \\ \vdots \\ 0 \\ 0 \\ N_{w|x_i} \\ \vdots \\ 0 \\ 0 \\ \vdots \\ N_{w|x_1} \\ \vdots \\ 0 \\ 0 \\ 0 \end{bmatrix} \tag{3.20}$$

3.4 Buckling analysis

Consider a two-node beam element in a local system *(x, z)*, where the *x*-axis coincides with the neutral axis. Adopting Timoshenko beam theory, the axial and transversal displacements of any arbitrary points are given by

$$\begin{aligned} u(x,z) &= u_0 - z\theta(x) \\ w(x,z) &= w(x) \end{aligned} \tag{3.21}$$

where u_0 is the axial displacement of a point on the neutral axis; z is the distance from the considered point to the *x*-axis, and $\theta(x)$ is the rotation of the cross-section. The axial and shear strains are deduced from Eq. (3.21) as

$$\begin{aligned} \varepsilon &= \frac{\partial u}{\partial x} + \frac{1}{2}\left(\frac{\partial w}{\partial x}\right)^2 - z\frac{\partial \theta}{\partial x} = \varepsilon_m + z\chi \\ \gamma &= \frac{\partial w}{\partial x} - \theta \end{aligned} \tag{3.22}$$

where ε_m, χ and γ are the membrane strain, curvature strain and shear strain, respectively. Assuming elastic behaviour, the axial and shear stresses associated with the strains of Eq. (3.22) are given by

$$\begin{aligned} \sigma &= E(x)\varepsilon \\ \tau &= \kappa G(x)\gamma \end{aligned} \tag{3.23}$$

In order to express the displacement at an arbitrary point in terms of the nodal displacements, it is necessary to introduce shape functions for *u, w* and *θ*.

By using the co-rotational approach here and noting that $\overline{u}_1 = \overline{w}_1 = \overline{w}_2 = 0$, one can write

$$\begin{aligned} u &= N_u \overline{u} \\ w &= N_w \overline{\theta} \\ \theta &= N_\theta \overline{\theta} \end{aligned} \tag{3.24}$$

where $\overline{\mathbf{\theta}} = \{\overline{\theta}_1 \;\; \overline{\theta}_2\}^T$; $\mathbf{N}_u$, $\mathbf{N}_w$, $\mathbf{N}_\theta$ are the matrices of interpolating functions for *u, w* and θ, respectively.

Regularly, these interpolating functions are unbalanced, causing membrane locking for the element formulation. In order to avoid this problem, the membrane strain in Eq. (3.22) is replaced by the effective strain, defined as

$$\varepsilon_{eff} = \frac{1}{\ell}\int_0^\ell \left(u_x + \frac{1}{2} w_{,x}^2 \right) dx \tag{3.25}$$

Substituting Eqs. (3.21), (3.22) and (3.24) into Eq. (3.25), one gets

$$\varepsilon_{eff} = \mathbf{b}_u \bar{\mathbf{u}} + \frac{1}{2\ell} \bar{\boldsymbol{\theta}}^T \left(\int_0^\ell \mathbf{b}_w^T \mathbf{b}_w dx \right) \bar{\boldsymbol{\theta}} \tag{3.26}$$

where $b_u = \frac{\partial N_u}{\partial x}$ and $b_w = \frac{\partial N_w}{\partial x}$.

Using the concept of effective strain, one can express the virtual work in the form

$$\begin{aligned} \delta U &= \int_V (\sigma \delta\varepsilon_{eff} + \tau\delta\gamma)\, dV \\ &= \int_0^\ell (N\delta\varepsilon_{eff} + M\,\delta\chi + Q\delta\gamma)\, dx \\ &= \int_0^\ell \left\{ N b_u \delta\bar{u} + \left[N\mathbf{e}_\theta^T + M\mathbf{b}_\theta^T + Q\left(\mathbf{b}_w^T - \mathbf{N}_\theta^T\right)\right] \delta\bar{\theta} \right\} dx \end{aligned} \tag{3.27}$$

where

$$\begin{aligned} & N = E(x)A\varepsilon_{eff} \\ & M = E(x)I\chi \\ & Q = \psi G(x)A\gamma \\ & \mathbf{b}_u = \frac{\partial \mathbf{N}_u}{\partial x}, \quad \mathbf{e}_\theta = \frac{\partial \varepsilon_{eff}}{\partial \bar{\theta}}, \quad \mathbf{b}_\theta = -\frac{\partial \mathbf{N}_\theta}{\partial x} \end{aligned} \tag{3.28}$$

Eq. (3.27) gives the components of the local internal force vector as

$$\begin{aligned} \bar{f}_u &= \int_0^\ell N\mathbf{b}_u\, dx \\ \bar{\mathbf{f}}_\theta &= \int_0^\ell [N\mathbf{e}_\theta + M\mathbf{b}_\theta + Q(\mathbf{b}_w - \mathbf{N}_\theta)]\, dx \end{aligned} \tag{3.29}$$

The tangent stiffness matrix in the local system can be expressed by sub-matrices as follows:

$$\overline{\mathbf{k}}_t = \begin{bmatrix} \overline{\mathbf{k}}_{uu} & \overline{\mathbf{k}}_{u\theta} \\ \overline{\mathbf{k}}_{u\theta}^T & \overline{\mathbf{k}}_{\theta\theta} \end{bmatrix} \tag{3.30}$$

where

$$\begin{aligned} \overline{\mathbf{k}}_{uu} &= \overline{f}_{u,\overline{u}} = \frac{1}{\ell^2}\int_0^\ell E(x)A\,dx \\ \overline{\mathbf{k}}_{u\theta} &= \overline{f}_{u,\overline{\theta}} = \frac{1}{\ell}\int_0^\ell E(x)A\mathbf{e}_\theta^T dx \end{aligned} \tag{3.31}$$

$$\overline{\mathbf{k}}_{\theta\theta} = \overline{\mathbf{f}}_{\theta,\overline{\theta}} = \int_0^\ell \begin{bmatrix} E(x)A\mathbf{e}_\theta\mathbf{e}_\theta^T + N\mathbf{B} + E(x)I\;\mathbf{b}_\theta\mathbf{b}_\theta^T \\ +G(x)A\,\psi(\mathbf{b}_w - \mathbf{N}_\theta)(\mathbf{b}_w^T - \mathbf{N}_\theta^T) \end{bmatrix} dx \tag{3.32}$$

where $\mathbf{B} = \dfrac{\partial \mathbf{e}_\theta}{\partial \overline{\theta}}$

Chapter 4: Technique for solving FGM beam

4.1 Co-rotational approach

The co-rotational approach is a convenient way to formulate geometrically non-linear finite elements. The central idea of the approach is to introduce a local coordinate system that continuously moves and rotates with the element during its deformation process. By using such a local system, the element deformation can be decomposed into a rigid body and pure deformation parts, and the geometrically non-linear configuration induced by the large body motion is incorporated in transformation matrices.

In the co-rotational formulation which will be adopted in this sub-section, the kinematics is described in an element-attached local coordinate system. The finite element formulation is first formulated in this local system and then transferred to a global system with the aid of transformation matrices. Among others, the elements proposed by Hsiao and Huo [48], Meek and Xue [82], Pacoste and Eriksson [97], and Nguyen [89] are some of the co-rotational beam elements for analysis of planar beams and frames which can be cited in this work.

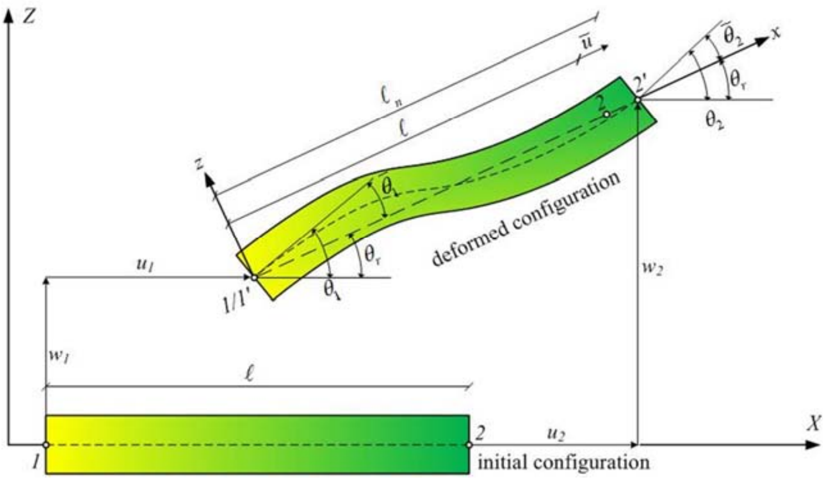

Figure 4.1: A two-node planar beam element and its kinematics in a global coordinate system *(X, Z)*

A local system *(x, z)* attached to the element is chosen, where its origin is always at node *1* and the *x* axis directs to node *2*. By choosing such a local system, the axial displacement at node *1* and transverse displacement at both the nodes in the local system are always zero. The local and global vectors of nodal displacements are respectively given by

$$\bar{\mathbf{d}} = \{\bar{u} \quad \bar{\theta}_1 \quad \bar{\theta}_2\}^T \tag{4.1}$$

$$\mathbf{d} = \{u_1 \quad w_1 \quad \theta_1 \quad u_2 \quad w_2 \quad \theta_2\}^T \tag{4.2}$$

In Eqs. (4.1) and (4.2), the superscript T denotes the transpose of a vector or a matrix, and the bar is used to indicate that the variable is defined in the local system. The vectors of nodal forces and moments associated with the nodal displacements of Eqs. (4.1) and (4.2) are as follows:

$$\bar{\mathbf{f}}_{in} = \{\bar{N} \quad \bar{M}_1 \quad \bar{M}_2\}^T \tag{4.3}$$

$$\mathbf{f}_{in} = \{N_1 \quad Q_1 \quad M_1 \quad N_2 \quad Q_2 \quad M_2\}^T \tag{4.4}$$

The components of the local vector $\bar{\mathbf{d}}$ in Eq. (4.1) can be computed as

$$\begin{aligned} \bar{u} &= \ell_n - \ell \\ \bar{\theta}_1 &= \theta_1 - \theta_r \\ \bar{\theta}_2 &= \theta_2 - \theta_r \end{aligned} \tag{4.5}$$

In Eq. (4.5), l, l_n *and* θ_r are respectively the initial, current length and rigid rotation of the elements, and they can be computed from coordinates of the nodes.

Assuming the strain energy U of the element has been derived, the element nodal force vector $\mathbf{f}_{\mathrm{in}}$ and the tangent stiffness matrix $\mathbf{k}_{\mathrm{t}}$ in the global system can be obtained by successive differentiation of the strain energy with respect to the nodal displacements:

$$\mathbf{f}_{in} = \frac{\partial U}{\partial \mathbf{d}} = \frac{\partial U}{\partial \bar{\mathbf{d}}} \frac{\partial \bar{\mathbf{d}}}{\partial \mathbf{d}} = \mathbf{T}_1^T \, \bar{\mathbf{f}}_{in} \tag{4.6}$$

$$\mathbf{k}_t = \frac{\partial^2 U}{\partial \mathbf{d}^2} = \frac{\partial}{\partial \mathbf{d}} \left(\frac{\partial U}{\partial \bar{\mathbf{d}}} \frac{\partial \bar{\mathbf{d}}}{\partial \mathbf{d}} \right) = \mathbf{T}_1^T \, \bar{\mathbf{k}}_t \, \mathbf{T}_1 + \bar{N} \, \mathbf{T}_2 + \left(\bar{M}_2 + \bar{M}_3 \right) \mathbf{T}_3 \tag{4.7}$$

In Eqs. (4.6) and (4.7), $\bar{\mathbf{f}}_{in} = \partial U / \partial \bar{\mathbf{d}}$, $\bar{\mathbf{k}}_t = \partial^2 U / \partial \bar{\mathbf{d}}^2$ are the local nodal force vector and tangent stiffness matrix, respectively.

$\mathbf{T}_1$, $\mathbf{T}_2$ and $\mathbf{T}_3$ are the transpose matrices which can be computed from Eq. (4.5) as

$$\mathbf{T}_1 = \frac{\partial \bar{\mathbf{d}}}{\partial \mathbf{d}} \quad ; \quad \mathbf{T}_2 = \frac{\partial^2 \bar{u}}{\partial \mathbf{d}^2} \quad ; \quad \mathbf{T}_3 = -\frac{\partial^2 \theta_r}{\partial \mathbf{d}^2} \tag{4.8}$$

4.2 Arc-length control method

The element internal force vector and tangent stiffness matrix are assembled to construct structural equilibrium equations, which can be written in the form

$$\begin{aligned}\mathbf{R}(\mathbf{D},\lambda) &= \mathbf{F}_{in}(\mathbf{D}) - \mathbf{F}_{ex}(\lambda) \\ &= \mathbf{F}_{in}(\mathbf{D}) - \lambda\mathbf{f}_{ex} = \mathbf{0}\end{aligned} \tag{4.9}$$

where the out-of-balance force vector **R** is a function of the current structural nodal displacements **D** and the load-level parameter λ; $\mathbf{F}_{\mathrm{in}}$ is the structural internal nodal force vector, constructed from the element force vector **F**in in standard way of the finite element method; $\mathbf{f}_{\mathrm{ef}}$ is the fixed external loading vector.

The non-linear equations (4.9) can be solved by an incremental/iterative procedure based on the Newton–Raphson method, in which the norm of vector **R**(**D**, λ) is guided towards zero.

The success of the incremental-iterative solution process relies on the constraint strategy used. Load control methods have difficulty at limit points, such as in snap-through buckling when the tangent matrix becomes singular.

Displacement control methods overcome problems at limit points (maximum and minimum loads) but subsequently experience convergence difficulty at turning points when the response curve turns back on itself, as in snap-back behaviour. In order to trace complete equilibrium paths for the possible complex behaviours mentioned above, the arc-length control method developed by Crisfield [22] is employed.

For this method, a constraint equation is introduced:

$$a = \left(\Delta\mathbf{D}^T\Delta\mathbf{D} + \Delta\lambda^2\phi^2\mathbf{f}_{ef}^T\mathbf{f}_{ef}\right) - \Delta l^2 = 0 \tag{4.10}$$

where Δl is the fixed value chosen by the analyst. The vector Δ**D** and the scalar Δλ are incremental and relate back to the last converged equilibrium state; ϕ is the scaling parameter.

For $\phi = 1$, Eq. (4.10) defines a spherical surface with a radius Δl in the load–displacement space, and it defines a cylindrical surface when $\phi = 0$.

With the constraint equation (4.10), instead of solving the equilibrium equations (4.9) directly, we find the intersection of the equilibrium path with the surface defined by Eq. (4.10).

The iterative procedure is obtained from the truncated Taylor expansion of the vector **R** and *a* around the current equilibrium point as

$$\begin{aligned}\mathbf{R} &= \mathbf{R}\big|_0 + \frac{\partial \mathbf{R}}{\partial \mathbf{D}}\Big|_0 \delta\mathbf{D} + \frac{\partial \mathbf{R}}{\partial \lambda}\Big|_0 \delta\lambda \\ &= \mathbf{R}\big|_0 + \mathbf{K}_t\big|_0 \delta\mathbf{D} + \mathbf{f}_{ef}\big|_0 \delta\lambda = \mathbf{0}\end{aligned} \tag{4.11}$$

$$a = a\big|_0 + 2\Delta\mathbf{D}^T\delta\mathbf{D} + 2\Delta\lambda\delta\lambda\phi^2\mathbf{f}_{ef}^T\mathbf{f}_{ef} = \mathbf{0} \tag{4.12}$$

where $\mathbf{R}|_0$ and $a|_0$ are defined from the current equilibrium point.

Eq. (4.11) gives the iterative displacement δ**D** and iterative load parameter δλ as

$$\begin{Bmatrix}\delta\mathbf{D}\\ \delta\lambda\end{Bmatrix} = -\begin{bmatrix}\mathbf{K}_t\big|_0 & \mathbf{f}_{ef}\\ 2\Delta\mathbf{D}^T & 2\Delta\lambda\phi^2\mathbf{f}_{ef}^T\mathbf{f}_{ef}\end{bmatrix}^{-1}\begin{Bmatrix}\mathbf{R}\big|_0\\ a\big|_0\end{Bmatrix} \tag{4.13}$$

As seen from Eq. (4.13), the augmented Jacobian matrix within the square brackets remains non-singular even when the K_t is singular. However, the Jacobian matrix in Eq. (4.13) is neither symmetric nor banded, and the computation based on the arc-length control method is expensive. The cylindrical arc-length method ϕ=0 is adopted in this work.

4.3 Implicit average constant acceleration Newmark method

The Newmark method is a method of numerical integration used to solve differential equations. It is widely used in numerical evaluation of the dynamic response of structures and solids such as in finite element analysis to model dynamic systems.

The finite difference approximations for the Newmark method are

$$\begin{aligned} D_{n+1} &= D_n \Delta t \dot{D}_n + \frac{\Delta t^2}{2}\left[(1-2\beta)\ddot{D}_n + 2\beta\ddot{D}_{n+1}\right] \\ \dot{D}_{n+1} &= \dot{D}_n + \Delta t\left[(1-\gamma)\ddot{D}_n + \gamma\ddot{D}_{n+1}\right] \end{aligned} \tag{4.14}$$

In the case where $\beta = 1/4$ and $\gamma = 1/2$, the Newmark method is implicit and unconditionally stable. In this case, the acceleration within the time interval $t \in [t_n\ t_n+1)$ is presumed to be constant.

Chapter 5: Static analysis of FGM structures

5.1 Using consistent shape functions

5.1.1 Cantilever beam with concentrated load

In the first example, a cantilever tapered beam loaded at the tip end, as shown in Fig. 5.1, is considered.

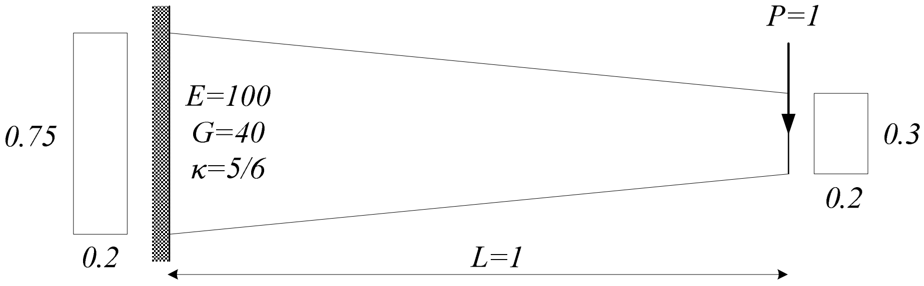

Figure 5.1: Cantilever having a variable cross-section

The beam is analyzed by using *one element* with the shape functions derived previously. The results of the tip end transverse displacements with and without considering shear deformation are compared with the theoretical solution of [27]. The results of analyses are shown in Table 5.1, where w_2 is the transverse displacement at the tip end. In Table 5.1, (a) denotes a case where shear deformation is considered; (b) denotes a case where shear deformation is not considered.

As shown in the table, both results using the formulated shape function are in good agreement with the theoretical results from the reference.

Table 5.1: Analysis of variable cross-section cantilever

			Present	**[27]**
	Q	***M***	w_2	
(a)	1.0	1.0	1.203	1.203
(b)	1.0	1.0	0.8977	0.897

5.1.2 Clamped-clamped beam with concentrated load

In the second example, the effect of shear deformation is further investigated. To this end, two clamped-clamped (C-C) beams with geometric data shown in Fig. 5.2 are employed in the calculation with various values of L. The beam is analyzed by using *two element* divisions.

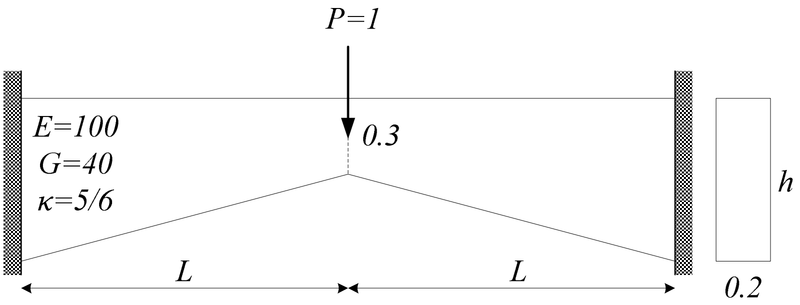

Figure 5.2: Clamped-clamped beam with height variation

Deflection including shear deformation w_s and neglecting shear deformation w_{ns} at the middle of the beams axes are listed in Tables 5.2 and 5.3, respectively. They are also compared with the results of [29]. Very good agreement can be observed from the tables.

Table 5.2: Reaction forces and deflections of C-C tapered beam ($h = 0.6$)

			w_s		w_{ns}	
L	***Q***	***M***	**Present**	**[29]**	**Present**	**[29]**
1	0.5	0.25	0.4651	0.468	0.2939	0.294
2	0.5	0.5	2.6929	2.700	2.3541	2.354
3	0.5	0.75	8.4629	8.464	7.9360	7.944
4	0.5	1.00	19.5208	19.524	18.8113	18.831
5	0.5	1.25	37.6446	37.645	36.7407	36.779

Table 5.3: Reaction forces and deflections of C-C tapered beam ($h = 0.9$)

			w_s		w_{ns}	
L	***Q***	***M***	**Present**	**[29]**	**Present**	**[29]**
1	0.5	0.25	0.2702	0.274	0.1362	0.137
2	0.5	0.5	1.3694	1.370	1.0894	1.096
3	0.5	0.75	4.1027	4.110	3.6777	3.698
4	0.5	1.00	9.3041	9.315	8.7666	8.766
5	0.5	1.25	17.7839	17.807	17.1216	17.120

5.1.3 Cantilever beam with distributed load

The third example refers to another cantilever tapered Bernoulli beam (Fig. 5.3) with a length of 10 *m*, subjected to a uniformly distributed load $q = 1$ *t/m*.

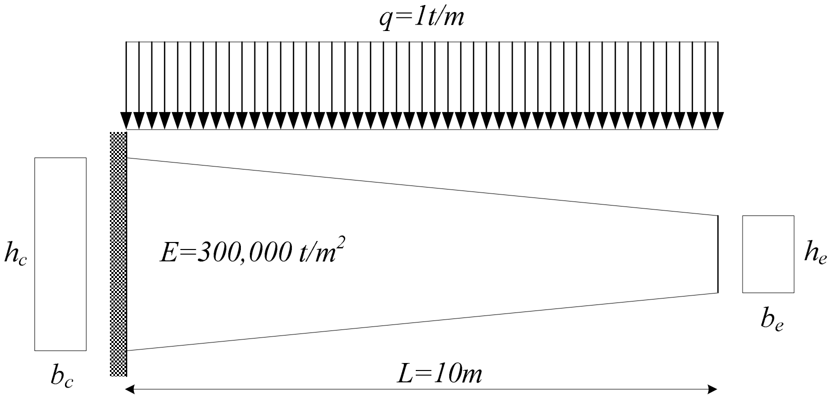

Figure 5.3: Simply-supported beam subjected to distributed load

The transverse displacements at the tip end are listed in Table 5.4.

Table 5.4: Reaction forces and transverse displacements of cantilever beam at the tip (*n*=number of element)

Case	**Present**				**[32]**		**Classical**	
	Q	***M***	***n* = 1**	***n* = 2**	***n* = 1**	***n* = 2**	***n* = 10**	***n* = 200**
A	10	50	3.1572	3.1572	3.1572	3.1572	3.1574	3.1572
B	10	50	1.5431	1.5431	1.5431	1.5431	1.5683	1.5432

The first row refers to a beam with unit depth and linearly varying width from 2 *m* at the clamped end to 0.25 *m* at the free end (Case A). The second row refers to a beam with unit width and varying depth between 2 *m* at the clamped end and 0.25 *m* at the free end (Case B). Let Young's modulus E=300,000 t/ m^2 for all cases. These displacements are compared to the numerical results of [32] and the classical, stepped rectangular cubic hermitian element approach.

5.1.4 Simply-supported beam with distributed load

The fourth example relates to a simply-supported (S-S) Bernoulli beam (Fig. 5.4) with the length of 10 *m*, also subjected to a distributed load *q*=1 *t/m*.

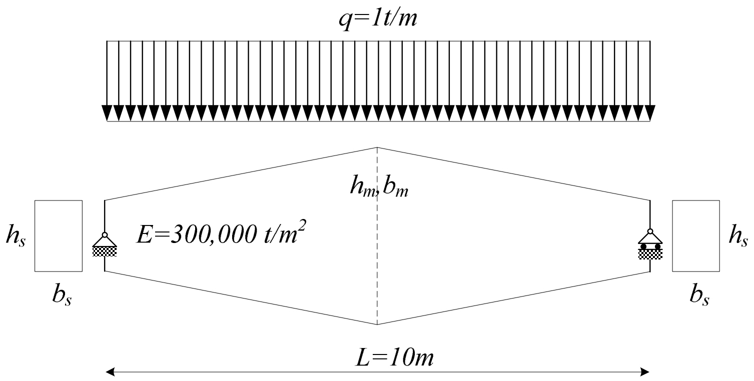

Figure 5.4: Cantilever beam subjected to distributed load

The mid-span vertical displacement is reported in Table 5.5, where the first row refers to a beam with constant depth and linearly varying width from 2 *m* at the mid-span to 0.25 *m* at the supported ends (Case A). The second row refers to a beam with constant width and varying depth between 2 *m* at the mid-span and 0.25 *m* at the supported ends (Case B). Let Young's modulus E=300,000 t/m^2 for all cases.

Table 5.5: Reaction forces and transverse displacements of S-S beam at the mid span (*n*=number of element)

Case	**Present**				**[32]**		**Classical**	
	QL	***QR***	***n* = 1**	***n* = 2**	***n* = 1**	***n* = 2**	***n* = 10**	***n* = 200**
A	5	5	3.7342	3.7350	3.7351	3.7351	3.7355	3.7351
B	5	5	2.8679	2.8681	2.8682	2.8682	2.8714	2.8684

5.2 Using the exact shape functions

By using the exact shape functions constructed following section 2.3.5, the results for Example 2 mentioned above, shown in Tables 5.6–5.7, are obtained by only *two element* divisions.

Table 5.6: Reaction forces and deflections of C-C tapered beam (h = 0.6)

L	***Q***	***M***	w_s	w_{ns}
1	0.5	0.25	0.4670	0.2943
2	0.5	0.5	2.700	2.3541
3	0.5	0.75	8.464	7.9376
4	0.5	1.00	19.524	18.831
5	0.5	1.25	37.645	36.779

Table 5.7: Reaction forces and deflections of C-C tapered beam (h = 0.9)

L	***Q***	***M***	w_s	w_{ns}
1	0.5	0.25	0.2748	0.1368
2	0.5	0.5	1.3708	1.0950
3	0.5	0.75	4.1105	3.6991
4	0.5	1.00	9.315	8.7668
5	0.5	1.25	17.8088	17.1203

5.3 Conclusions

- The consistent shape functions from sub-section 2.3.2 and the exact shape functions from sub-section 2.3.5 were applied in some numerical examples of the static analysis of tapered elements.
- The accuracy was verified through comparison with published works.
- The numerical results show that significant accuracies can be reached with least element division by using the consistent shape functions and the exact shape functions.

Chapter 6: Free vibration of FGM structures

6.1 Using consistent shape functions

By using the consistent shape functions, a tapered beam shown in Fig. 6.1 with various boundary conditions at both ends is analysed.

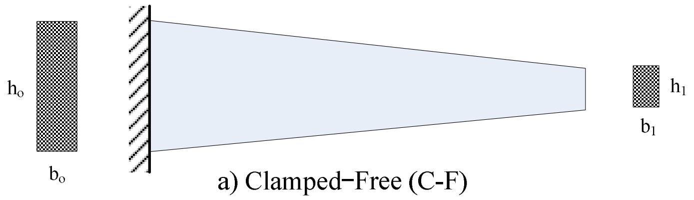

a) Clamped−Free (C-F)

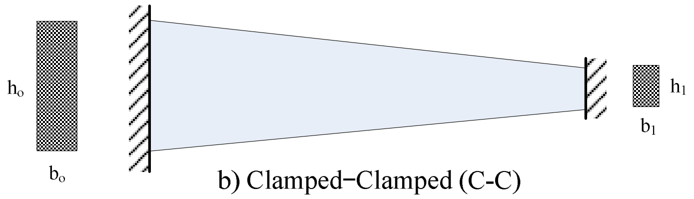

b) Clamped−Clamped (C-C)

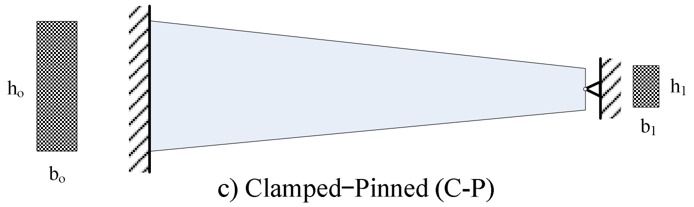

c) Clamped−Pinned (C-P)

Figure 6.1: Various boundary conditions of tapered beams

6.1.1 Clamped–free tapered beam

Consider a clamped–free tapered beam shown in Fig. 6.1, referred to as case (a). The geometry and material data of the steel beam are as follow: $r^2 = \frac{I_0}{A_0 L^2} = 0.08$, $m = 0.5$, $p = 0.3$, $L = \frac{25p}{4\sqrt{3}}$, $\frac{E}{\kappa G} = 3.059$, $\kappa = \frac{2}{3}$, $E = 210 GPa$, $\rho = 7850 kg/m^3$. The non-dimensional frequencies of the beam is defined as

$$\mu = \omega \sqrt{\frac{\rho A_0 L^4}{E I_0}} \tag{6.1}$$

with different values of taper ratios α and β are listed in Table 6.1 in comparison with those of [5].

Table 6.1: Non-dimensional natural frequencies of C–F tapered Timoshenko beam

β		***α = 0.0***		***α = -0.4***		***α = -0.6***		***α = -0.8***	
		Presen	**[5]**	**Presen**	**[5]**	**Presen**	**[5]**	**Presen**	**[5]**
0.	***μ***	3.3241	3.3240	3.9112	3.8605	4.4307	4.2883	5.0656	5.0062
	μ	16.294	16.288	17.228	17.127	18.011	17.786	19.034	18.902
	μ	36.773	36.707	37.531	37.360	38.215	37.921	39.064	38.984
	μ	58.538	58.277	59.313	58.877	60.009	59.432	61.008	60.546
-	***μ***	3.4343	3.4247	4.0254	3.9544	4.5492	4.3953	5.1944	5.1198
	μ	15.858	15.890	16.734	16.681	17.481	17.311	18.464	18.391
	μ	35.391	35.430	36.110	36.070	36.770	36.614	38.005	37.645
	μ	57.077	56.891	57.721	57.455	58.351	57.963	59.103	58.981
-	***μ***	3.5881	3.5605	4.1840	4.0941	4.7127	4.5386	5.2870	5.2703
	μ	15.255	15.352	16.075	16.097	16.784	16.696	17.890	17.742
	μ	33.543	33.787	34.251	34.418	34.894	34.949	35.960	35.954
	μ	54.620	54.756	55.243	55.302	55.835	55.781	56.776	56.737
-	***μ***	3.8299	3.7623	4.4327	4.3011	4.9670	4.7498	5.5329	5.4887
	μ	14.446	14.644	15.209	15.341	15.882	15.910	17.088	16.922
	μ	31.038	31.623	31.737	32.248	32.365	32.768	33.800	33.750
	μ	50.891	51.622	51.511	52.166	52.084	52.630	53.568	53.547
-	***μ***	4.2137	4.1177	4.6301	4.6655	5.0703	5.1194	5.8328	5.8629
	μ	13.767	13.757	14.172	14.405	14.808	14.943	15.918	15.922
	μ	28.636	28.636	29.116	29.251	29.348	29.762	30.714	30.725
	μ	46.818	46.828	47.449	47.381	47.719	47.843	48.735	48.739

Table 6.1 showing the results of non-dimensional frequencies in the clamped–free tapered example, the present formulation is in good agreement with the results reported by Attarnejad [5]. In both formulations, *four element* divisions for the beam were employed to obtain the results.

6.1.2 Clamped–clamped tapered beam

The following data of a tapered Timoshenko beam made of steel, shown in Fig. 6.1 case (b), are employed in the following computation: $E = 210GPa$, $G = 80GPa$, $\rho = 7800kg/m^3$, $m = p = 2.54cm$, $\alpha = 0$, $\beta = -0.5$, $\kappa = 0.667$, $L = 25cm$,

$A_0 = 6.45cm^2$, $A_1 = 0.5A_0$ in which A_0 and A_1 are the cross-sectional areas at the left end and the right end of the beam, respectively.

For comparison, the first five natural frequencies of the present formulation and the results by Cleghorn [20] are listed in Table 6.2 by varying the number of element divisions, *nELE*. The result shows the superior rate of convergence of the natural frequency in the present work.

Table 6.2: Natural frequencies of a C–C tapered Timoshenko beam

nELE		ω_1	ω_2	ω_3	ω_4	ω_5
2	**[20]**	0.93856E+4	0.34163E+5			
	Present	0.95200E+4	0.25770E+5			
3	**[20]**	0.92332E+4	0.25050E+5	0.59150E+5	0.11991E+6	
	Present	0.94300E+4	0.25260E+5	0.48360E+5	0.74550E+5	
4	**[20]**	0.91972E+4	0.24561E+5	0.47191E+5	0.91471E+5	0.15040E+6
	Present	0.92700E+4	0.24390E+5	0.45380E+5	0.71120E+5	0.10098E+6
5	**[20]**	0.91845E+4	0.24359E+5	0.46219E+5	0.74565E+5	0.12980E+6
	Present	0.92000E+4	0.24200E+5	0.44900E+5	0.69900E+5	0.98400E+5
6	**[20]**	0.91788E+4	0.24261E+5	0.45701E+5	0.72990E+5	0.10616E+6
	Present	0.92000E+4	0.24200E+5	0.44900E+5	0.69900E+5	0.98400E+5
7	**[20]**	0.91758E+4	0.24208E+5	0.45389E+5	0.72051E+5	0.10389E+6
	Present	0.92000E+4	0.24200E+5	0.44900E+5	0.69900E+5	0.98400E+5
8	**[20]**	0.91740E+4	0.24176E+5	0.45195E+5	0.71395E+5	0.10248E+6
	Present	0.92000E+4	0.24200E+5	0.44900E+5	0.69900E+5	0.98400E+5
9	**[20]**	0.91728E+4	0.24155E+5	0.45067E+5	0.70944E+5	0.10138E+6
	Present	0.92000E+4	0.24200E+5	0.44900E+5	0.69900E+5	0.98400E+5
10	**[20]**	0.91720E+4	0.24141E+5	0.44979E+5	0.70628E+5	0.10057E+6
	Present	0.92000E+4	0.24200E+5	0.44900E+5	0.69900E+5	0.98400E+5
11	**[20]**	0.91714E+4	0.24131E+5	0.44916E+5	0.70398E+5	0.99963E+5
	Present	0.92000E+4	0.24200E+5	0.44900E+5	0.69900E+5	0.98400E+5
12	**[20]**	0.91710E+4	0.24123E+5	0.44869E+5	0.70226E+5	0.99506E+5
	Present	0.92000E+4	0.24200E+5	0.44900E+5	0.69900E+5	0.98400E+5

From Table 6.2, the results of the first five natural frequencies of the present work give better results than those in [20]. Furthermore, with only *six element* divisions, the present formulation shows faster convergence results compared to the 12 elements required in [20].

6.1.3 Various boundary conditions of tapered beam

Let us consider a tapered beam in Fig. 6.1 with $r^2 = \frac{I_0}{A_0 L^2} = 0.08$, $m = 0.05$, $p = 0.3$, $L = \frac{5p}{\sqrt{3}}$, $\frac{E}{\kappa G} = 3.12$, $\kappa = \frac{2}{3}$, $E = 210 GPa$, $\rho = 7850 kg / m^3$ under various boundary conditions: clamped–free, clamped–clamped, and clamped–pinned. The cross-session is rectangular with constant width and linear-varying height. The non-dimensional frequencies of the beam that are defined as

$$\mu = \omega \sqrt{\frac{\rho A_0 L^4}{E I_0}} \tag{6.2}$$

with two height ratio values (*0* and *-0.2*), are shown in Table 6.3 in comparison with those of Attarnejad [5].

From Table 6.3, the results of the non-dimensional frequencies of the present formulation show lower convergence results under various boundary conditions compared to the results in [5]. In both formulations, *four element* divisions for the beam were employed to obtain the results.

Table 6.3: Non-dimensional natural frequencies of tapered Timoshenko beams with various boundary conditions

β	**BC**		**μ1**	**μ2**	**μ3**	**μ4**	**μ5**
0	***C-F***	**Present**	3.22720	14.47780	31.50240	48.19680	62.87280
		[5]	3.22713	14.46893	31.50254	47.90902	62.34702
	C-P	**Present**	11.08680	27.17590	45.11830	59.44520	63.59720
		[5]	11.08250	27.11438	44.84353	59.20303	63.33950
	C-C	**Present**	13.83890	28.58680	45.95580	61.42410	68.86960
		[5]	13.83476	28.51793	45.66595	61.86205	68.28361
-0.2	***C-F***	**Present**	3.34530	14.32890	30.91900	48.13030	65.05240
		[5]	3.33065	14.28921	30.71080	47.75021	64.99695
	C-P	**Present**	10.75020	26.31190	44.03880	62.05360	68.56940
		[5]	10.68689	26.10717	43.59072	61.65596	68.42075
	C-C	**Present**	13.31860	27.95770	45.12020	61.90550	72.36990
		[5]	13.22227	27.77822	44.69713	61.80658	72.55473

6.2 Using the exact shape functions

Consider a prismatic FGM beam with a rectangular cross-section. The beam is made of two materials with a constant value of mass density while the effective Young's modulus and shear modulus are assumed to vary in the longitudinal direction according to

$$\begin{aligned} E(x) &= (E_{left} - E_{ight})\left(1 - \frac{x}{L}\right) + E_{right} \\ G(x) &= (G_{left} - G_{ight})\left(1 - \frac{x}{L}\right) + G_{right} \end{aligned} \tag{6.3}$$

The simply-supported beam with geometric data: width b=0.4 *m*; height h=0.9 *m* and the total length L=20 *m* is employed in the computation of the fundamental frequencies. The results (with *one element* division) are compared with reference [38], which is computed with 10 element divisions. The very good agreement between the frequencies obtained in this work with those of the reference is shown in Table 6.4, where $E_r = \frac{E_{left}}{E_{right}}$; μ_1, μ_2 are respectively the first and the second fundamental frequency of the beam.

Table 6.4: Frequencies of prismatic FGM beam

μ_1			μ_2	
E_r	**Present**	**[38]**	**Present**	**[38]**
1	0.5	0.25	0.2748	0.1368
2	0.5	0.5	1.3708	1.0950
3	0.5	0.75	4.1105	3.6991
4	0.5	1.00	9.315	8.7668
5	0.5	1.25	17.8088	17.1203

6.3 Conclusions

- The consistent shape functions from sub-section 2.3.2 and the exact shape functions from sub-section 2.3.5 were applied in the calculation of a non-prismatic homogeneous beam and a prismatic FGM beam.
- The accuracy was compared with references.
- By using the derived shape functions in this work, the solutions of vibration problems with least element divisions can approximate the results with high accuracy in both a homogeneous non-prismatic beam and a non-homogeneous prismatic beam.

Chapter 7: Dynamic analysis of FGM structures

The problems of moving loads on an elastic beam are often met in the design of bridges, railways, highways and in many modern machining operations. A large number of investigations concerning the dynamic analysis of beams subjected to a moving load can be found in the literature. In the early and excellent monograph of Fryba [37], a number of closed-form solutions for moving load problems have been derived by using Fourier and Laplace transforms. In 1984, Hino [47] derived the finite element formulation of a non-linear beam subjected to a moving load by using the Galerkin finite element method. Two years laters, Rieker [105] discussed the effect of discretization and boundary conditions on the accuracy of the finite element solution of beams subjected to moving loads. Lin and Trethewey [78], in 1990, formulated a two-node beam element and used it to compute the dynamic response of a beam subjected to different types of moving load. Later, based on the analytical and finite element solutions to the fundamental moving load problem, Olsson [95] provided an interesting discussion and the reference data for studies of the moving load problem. In 1996, Thambiratnam and Zhuge [124] presented a finite element procedure for studying the dynamic behaviour of a Bernoulli beam resting on a Winkler foundation under a moving load, and then applied the method to investigate the dynamic response of railway tracks. One year later, Henchi [45] presented the dynamic stiffness method, followed by the modal fast Fourier transform approach for the moving load problem of a multi-span beam subjected to multiple moving point loads. Zheng [142], in 1998, studied the vibration of non-uniform beams and bridges under the action of moving loads by using the modified beam vibration functions. Later, Ichikawa [54] investigated the dynamic behaviour of a multi-span continuous beam subjected to a constant speed moving mass. Recently, Nguyen [86] derived a finite element formulation for computing the dynamic response of a Timoshenko beam on a two-parameter elastic foundation by using the solution of the governing differential equations of a Timoshenko beam to interpolate the transverse displacement and rotation.

7.1 Multiple spans with single moving load

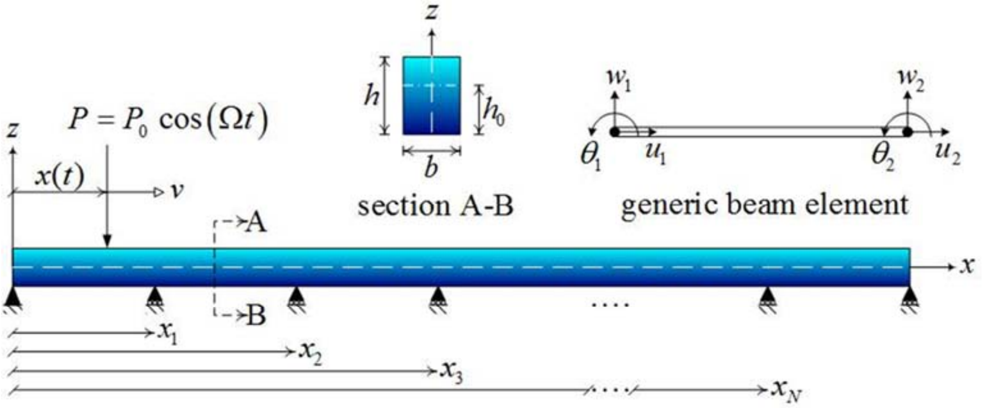

Figure 7.1: A multi-span FGM beam traversed by a moving harmonic load and a generic beam element

Fig. 7.1 shows a multi-span beam with length L subjected to a harmonic load, $P=P_0cos(\Omega t)$, moving at a constant speed from left to right. In the figure, $x_1, x_2,..., x_N$ are the abscissas of the N intermediate supports. The prismatic beam made of steel and alumina is computed in this section. It is assumed that the beam is formed from spans having the same length. The Young's modulus, mass density and Poisson's ratio of steel are respectively 210 MPa, 7800 kg/m^3, 0.3177, and those of alumina are 390 MPa, 3960 kg/m^3 and 0.3, respectively.

Except for the mentioned cases, beams with L=20 m, h=1 m and b=0.5 m are chosen in the computation. Using the derived finite element formulation in sub-section 2.2.1 with the shape functions obtained from sub-section 2.3.4, the dynamic response of multi-span FGM beams is computed.

7.1.1 Formulation validation

Firstly, the natural frequencies of a multi-span homogeneous beam are computed, and the obtained numerical results are listed in Table 7.1, where the corresponding results obtained by Ichikawa [54] are also given.

The dimensionless natural frequency parameter, μ_i, in Table 7.1 is defined as

$$\mu_i^2 = \omega_i L_S^2 \sqrt{\frac{\rho_0 A}{E_0 I}} \tag{7.1}$$

where ω_i is the natural frequency; L_S is the length of a span; E_0, ρ_0 are the Young's modulus and mass density of the homogeneous beam, respectively.

It should be noted that since the Bernoulli beam theory is used in Ichikawa [54], and in order to ensure that the numerical results are comparable, the frequencies in Table 7.1 have been computed with an aspect ratio $L_S/h = 100$, which is large enough to omit the effect of the shear deformation. As seen from Table 7.1, good agreement between the frequencies computed in the present work and those of reference [54] is noted.

Table 7.1: Comparison of first five natural frequencies of multi-span homogeneous beams

Number of spans		μ_1	μ_2	μ_3	μ_4	μ_5
1	**Present**	3.1413	6.2811	9.4182	12.5522	15.6838
	[54]	π	2π	3π	4π	5π
2	**Present**	3.1413	3.9258	6.2811	7.0648	9.4181
	[54]	π	3.9266	2π	7.0686	3π
3	**Present**	3.1413	3.5559	4.2965	6.2811	6.7045
	[54]	π	3.5564	4.2975	2π	6.7076
4	**Present**	3.1413	3.3928	3.9258	4.4621	6.2811
	[54]	π	3.3932	3.9266	4.4633	2π

Secondly, the fundamental frequency of a one-span FGM beam composed of aluminium (Al) and alumina (Al2O3), previously studied in [118] and [116], is computed. The Young's modulus, mass density and Poisson's ratio of alumina are 70 GPa, 2707 kg/m^3 and 0.23, respectively.

The computed fundamental frequency parameters of this work are listed in Table 7.2 for various values of the aspect ratio, L/h. The corresponding values obtained by using an analytical method in [118] and a numerical method in [116] are also given in the table. The non-dimensional fundamental frequencies, μ in Table 7.2, have been defined according to [118] as

$$\mu = \omega L^2 \sqrt{\frac{I_{11}}{h^2 \int_0^L E(z)dz}} \tag{7.2}$$

where ω is the fundamental frequency of the FGM beam.

As seen from Table 7.2, the fundamental frequencies computed in this work are in good agreement with those of [118] and [116], regardless of the aspect ratio.

Table 7.2: Comparison of non-dimensional fundamental frequency of one-span FGM beam

n	***L/h***	**10**	**30**	**100**
0.3	**Present**	2.692	2.737	2.742
	[118]	2.695	2.737	2.742
	[116]	2.701	2.738	2.742

Thirdly, the maximum dynamic deflection factor at the mid-span and the corresponding speed of one-span FGM beams composed of steel and alumina with L=20 m, h=0.9 m and b=0.4 m, previously studied in [117], are computed.

The obtained results are listed in Table 7.3. In the table, the dynamic deflection factor f_D is defined as $f_D=max(w(L/2, t)/w_0)$ where w_0 is the static deflection of the steel beam under static load P_0 acting at the mid-span.

Table 7.3: Maximum deflection factor and corresponding speed of one-span FGM beam under a moving load

n	**Present**		**[117]**	
	$\boldsymbol{max(f_D)}$	$\boldsymbol{v(m/s)}$	$\boldsymbol{max(f_D)}$	$\boldsymbol{v(m/s)}$
0.2	1.0346	222	1.0344	222
0.5	1.1445	197	1.1444	198
1	1.2505	178	1.2503	179
2	1.3776	164	1.3776	164
Pure alumina	0.9328	252	0.9328	252
Pure steel	1.7324	132	1.7324	132

Very good agreement between the numerical results of this work with those of the reference [117] is seen from the table. The numerical results listed in Tables 7.1–7.3 have been computed by using *14 elements* for each span.

7.1.2 Natural frequencies

Table 7.4 lists the first three non-dimensional natural frequencies of the multi-span FGM beam for different values of the index *n* and for an aspect ratio $L_S/h=30$.

Table 7.4: The first three non-dimensional frequencies of a multi-span FGM beam for various values of index *n* (for $L_S/h=30$)

n	**Number of element**	μ_1	μ_2	μ_3
0.3	**1**	3.9819	7.9423	11.8624
	2	3.9819	4.9707	7.9423
	3	3.9819	4.5046	5.4370
	4	3.9819	4.2990	4.9707
1	**1**	3.6546	7.2893	10.8867
	2	3.6546	4.5621	7.2893
	3	3.6546	4.1343	4.9901
	4	3.6546	3.9456	4.5621
5	**1**	3.3682	6.7171	10.0302
	2	3.3682	4.2041	6.7171
	3	3.3682	3.8100	4.5982
	4	3.3682	3.6362	4.2041

The first three non-dimensional natural frequencies computed with various values of the aspect ratio are listed in Table 7.5 for an index *n*=0.5.

It should be noted that the numerical results in Tables 7.4 and 7.5 are computed for multi-span beams composed of steel and alumina and the frequencies have been normalized according to Eq. (7.1). The influence of the number of spans, the index *n*, and the aspect ratio on the natural frequencies of the beam is clearly seen from the tables.

Irrespective of the index *n* and the aspect ratio, the first frequency is unchanged, while the second and third frequencies of the beam reduce when increasing the number of spans, and this result is in agreement with that of the homogeneous beam reported in [54]. The natural frequencies, as seen from Table 7.4, are smaller for a beam associated with a larger index *n*, regardless of the number of spans.

This is due to the fact that, as seen from Eq. (2.22), the beam with higher index *n* contains more steel and thus it is softer, and as a result, its fundamental frequency is lower.

The effect of the aspect ratio on the natural frequencies of the beam is clearly seen from Table 7.5, where the frequencies slightly reduce for the beam having a lower aspect ratio, regardless of the number of spans. In other words, the shear deformation slightly reduces the natural frequencies of the FGM beam.

Table 7.5: Non-dimensional frequencies of a multi-span FGM beam for various aspect ratios L_S/h (for n=0.5)

Number of spans	L_S/h	μ_1	μ_2	μ_3
2	10	3.8177	4.7215	6.4510
	20	3.8411	4.7877	7.6360
	100	3.8488	4.8100	7.6958
3	10	3.8177	4.2963	5.1416
	20	3.8411	4.3416	5.2330
	100	3.6546	4.3567	5.2641
4	10	3.8177	4.1081	4.5613
	20	3.8411	4.1447	4.7877
	100	3.8488	4.1569	4.8100

7.1.3 Dynamic deflection

The normalized deflections at the midpoint of the first and second spans of a four-span FGM beam are shown in Figs. 7.2–7.4 for various values of the index n, speed parameter f_v and excitation frequency.

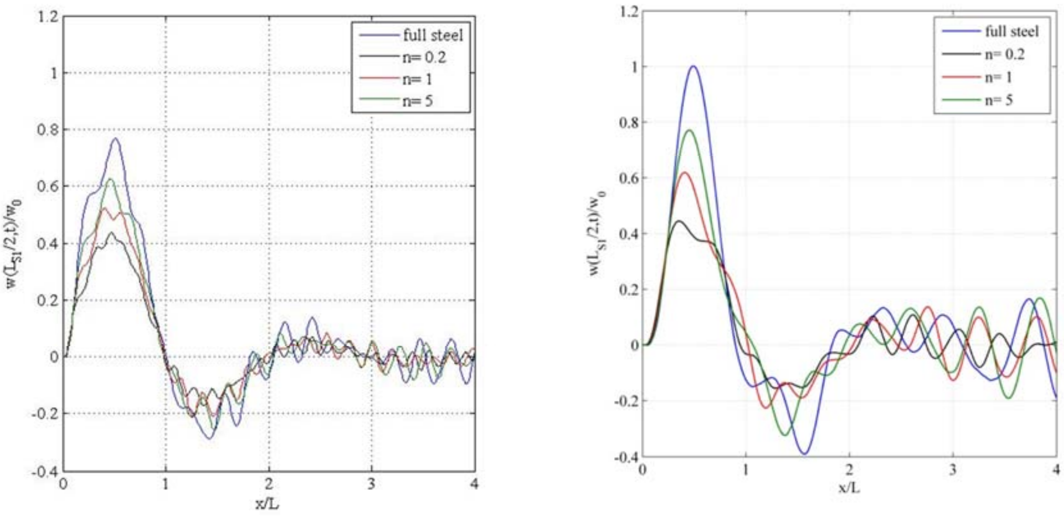

(a) f_V = 0.5

(b) f_V = 1.2

Figure 7.2: Normalized deflection at midpoint of the first span with $\Omega = 0$ (four-span beam)

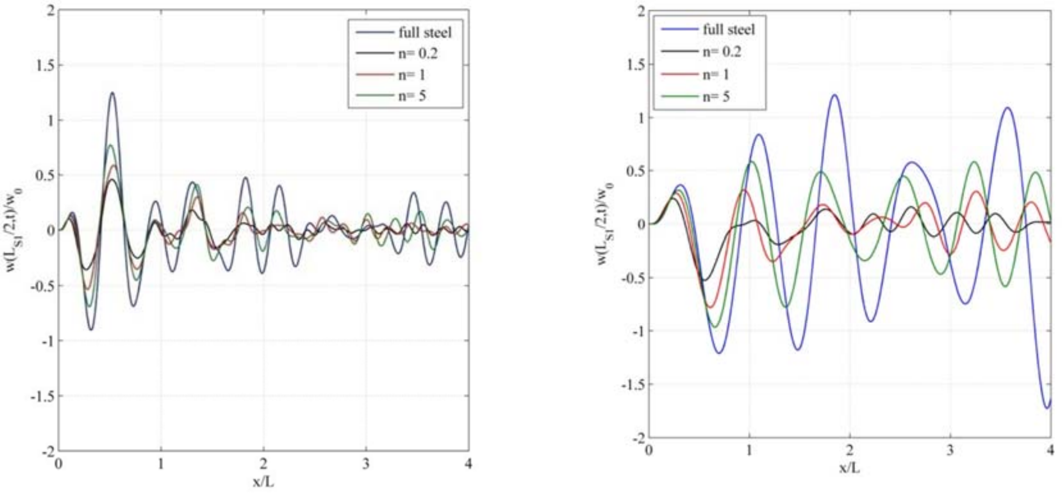

(a) $f_V = 0.5$ (b) $f_V = 1.2$

Figure 7.3: Normalized deflection at midpoint of the first span with $\Omega = 20$ (four-span beam)

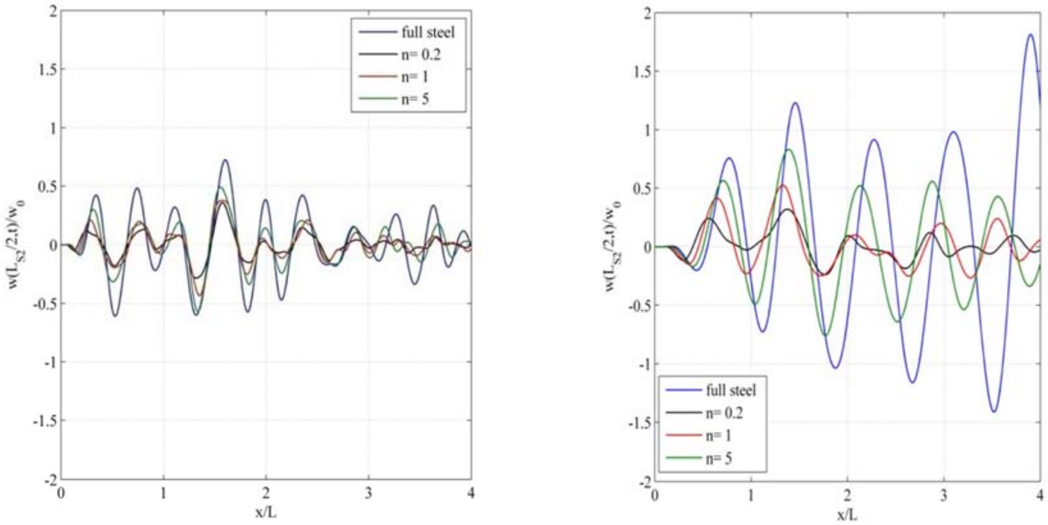

(a) $f_V = 0.5$ (b) $f_V = 1.2$

Figure 7.4: Normalized deflection at midpoint of the second span with $\Omega = 20$ (four-span beam)

In the figures, $w(L_S/2,t)$ denotes the dynamic deflection at the midpoint of the i-th span, and $w_S = P_0 L_{Si}/48 E_b I$ is the static deflection of a simply supported beam with length L_S under a static load P_0 at the midpoint.

The speed parameter f_v is defined in accordance with [54], $f_v = vL_S\sqrt{\frac{\rho_b A}{E_b I}}$, and thus for the given data of the beam and for f_v =0.5 and f_v =1.2, the equivalent speed of the moving load is 37.5 m/s and 90 m/s for the beam with a span length of 20 m, respectively.

As seen from the figures, the material heterogeneity which is governed by the index *n* clearly affects the dynamic deflection of the beam. The maximum normalized deflection of the beam associated with a higher index *n* is higher than that of the beam with lower index *n*.

In Fig. 7.5, the relation between the speed parameter f_D and the maximum dynamic deflection at the midpoint of the first span is shown for various values of the index n.

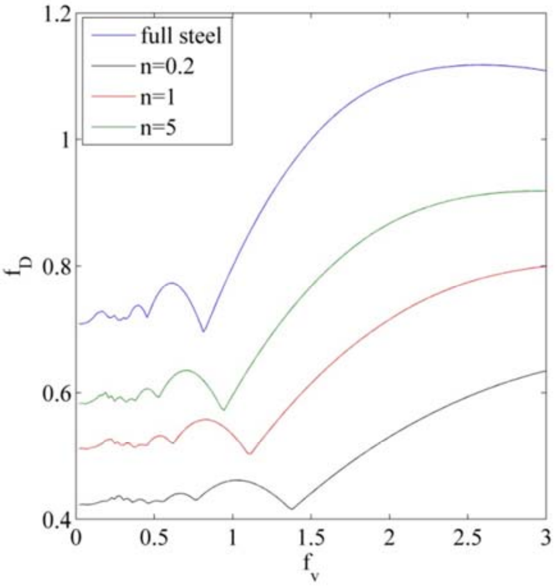

Figure 7.5: Maximum normalized deflection at midpoint of the first span (**Ω** = *0*, four-span beam)

The effect of the material heterogeneity and the moving speed is clearly seen from the figure, and the maximum dynamic deflection is higher for the beam associated with a higher index *n*, regardless of the moving speed. This is due to the fact that, as seen from Eq. (2.22), the beam with higher index *n* contains more steel and thus it is softer.

The normalized dynamic deflections at the first and second spans of the FGM beam with different numbers of spans computed with various values of the speed parameters are shown in Fig. 7.6 for **Ω**=0, n=1 and f_v =1.2.

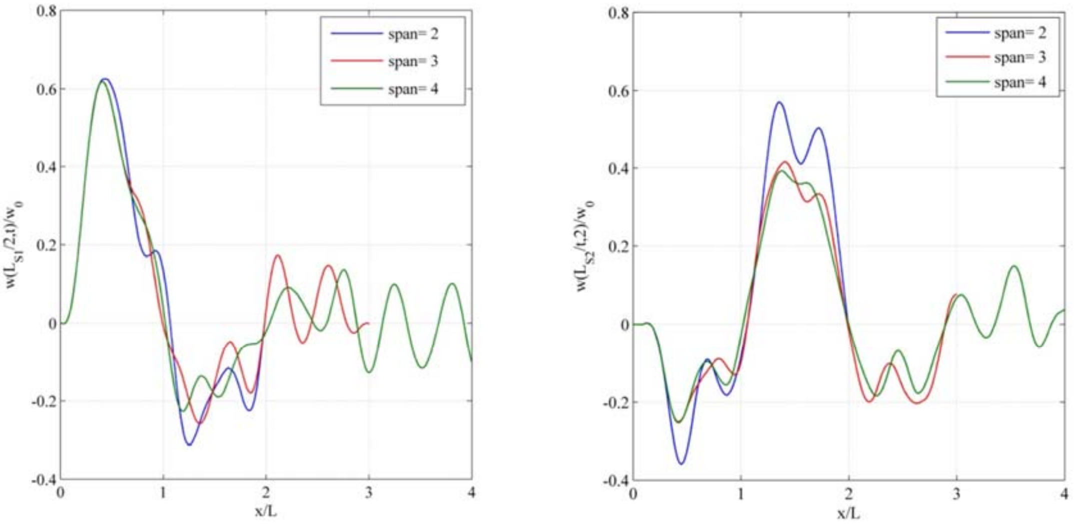

First span

Second span

Figure 7.6: Normalized deflection at midpoint of the first and second spans for FGM beam with different numbers of spans (n = 1, **Ω** = 0, f_v = 1.2)

As seen from the figure, the maximum deflection at the midpoint of the first and second spans of the beam slightly reduces for the beam with the greater number of spans. The difference in the maximum dynamic deflection at the midpoint of the second span due to different numbers of spans tends to be larger than that of the first span. In Fig. 7.7, the normalized dynamic deflections at the midpoint of the first and second spans of a four-span beam are respectively depicted for various values of the excitation frequency **Ω**, and for $n = 1, f_v = 0.5$.

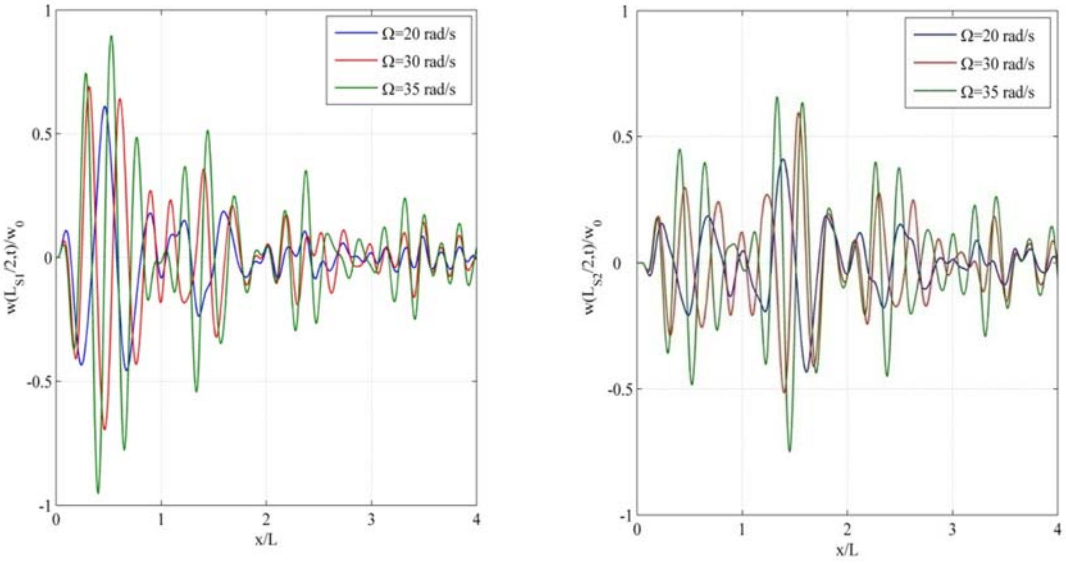

First span

Second span

Figure 7.7: Normalized deflection at midpoint of the first and second spans of four-span beam with various values of excitation frequency $f_v = 0.5, n = 1$

It should be noted that the fundamental frequency of the FGM beam is ω_1=49.8981 rad/s for n=1. As seen from the figure, the beam executes more vibration cycles when it subjected to a moving load with a higher frequency. The maximum dynamic deflection steadily increases when raising the excitation frequency towards the fundamental frequency of the beam. Thus, the resonant phenomenon tends to occur when the excitation frequency approaches the fundamental frequency.

7.1.4 Beam with different aspect ratios

The effect of the aspect ratio, defined as a ratio of the span length to the beam height, L_S/h, is investigated in this sub-section. To this end, keeping all the data above, the computation is performed with L_S = 5, 10 and 50.

Fig. 7.8 shows the midpoint normalized deflection at the first and second spans of the beam for various values of the aspect ratios and for f_v= 0.5, n=1, Ω = 0, respectively.

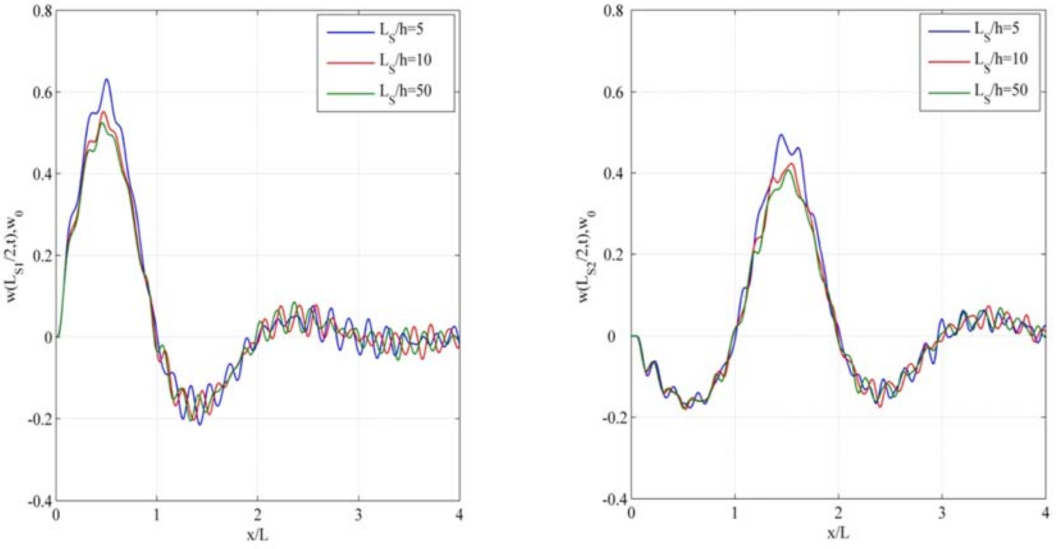

First span

Second span

Figure 7.8: Normalized deflection at midpoint of the first and second spans of four-span beam with various values of aspect ratio $f_v = 0.5$, $n = 1$, $\Omega = 0$

The effect of the aspect ratio is clearly seen from the figures, where the maximum dynamic deflection slightly increases by reducing the aspect ratio. Since the shear deformation is more pronounced for a beam with a lower aspect ratio, one can say that the shear deformation, which has been taken into consideration in the present work, increases the dynamic deflection of the beam. The numerical results depicted in the figures show the capability of the formulated element in modelling the shear deformation effect of the FGM beam.

7.1.5 Conclusions

- The dynamic response of the multi-span FGM beam subjected to a moving harmonic load was presented.
- The shift of the neutral axis position was taken into account in the calculation with the aid of the Newmark method.
- A parametric study was carried out to highlight the influences of the material distribution, the number of spans, loading parameter, and the aspect ratio on the dynamic characteristics of the beam:
    - The material distribution and the aspect ratio affect the natural frequencies of the beam. The frequencies are smaller for a beam with a larger index *n* or a smaller aspect ratio *L/h*, regardless of the number of spans.
    - The material heterogeneity shows a clear influence on the dynamic deflection of the beam. In the beam with a higher index *n* it is bigger than that of the beam with a lower index *n*, regardless of moving speed.
    - The deflection of the beam slightly increases by reducing the aspect ratio *L/h*, or shear deformation can increase the deflection of the beam.

7.2 In thermal environment due to a moving harmonic load

7.2.1 Numerical results

This section investigates the FGM beam in sub-section 2.2.2 due to a moving harmonic load, as shown in Fig. 7.9.

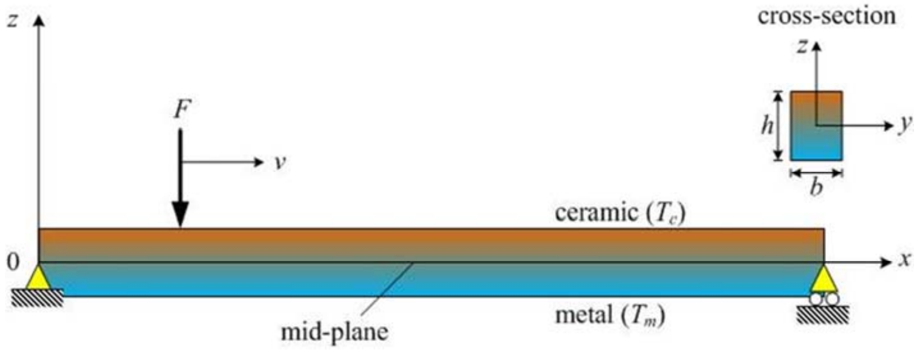

Figure 7.9: A simply supported FGM beam under a moving load $F = F_0 cos(\Omega t)$

The material properties are considered to be temperature-dependent. Two types of temperature distribution, namely uniform and non-linear temperature rises, are considered. The temperature is assumed to vary in the beam thickness only, and its distribution is obtained from the steady-state Fourier equation. A simply supported FGM beam with rectangular cross-section under a load $F=F_0 cos(\Omega t)$ with F_0 =100 kN, moving from right to left, as shown in Fig. 7.9, is considered.

An aspect ratio L/h=20 is assumed, and a uniform increment time step, $\Delta T = \sum T / 500, \sum T = L / v$ as the total time for the load F to across the beam, is employed for computation.

The investigation is carried out based on the following assumptions:

- the load F is always in contact with the beam, and its velocity (v) is constant
- the beam is initially at rest, and the inertial effect of the load F is negligible.

The investigated beam is assumed to be composed of alumina (Al_2O_3) and steel

(SUS304). Table 7.6 lists the coefficients of the constituents of the beam considered in this work.

Table 7.6: Temperature-dependent coefficients of Al_2O_3 and SUS304

Material	**Property**	P_0	P_{-1}	P_1	P_2	P_3
Al2O3	$E(Pa)$	349.55×10^{9}	0	-3.853×10^{-4}	4.027×10^{-7}	-1.673×10^{-10}
	$\rho(kg/m^{3})$	3800	0	0	0	0
	$\alpha(K^{-1})$	6.8269×10^{-6}	0	1.838×10^{-4}	0	0
	$K(Wm/K)$	-14.087	-1123.6	-6.227×10^{-3}	0	0
SUS304	$E(Pa)$	201.04×10^{9}	0	3.079×10^{-4}	-6.534×10^{-7}	0
	$\rho(kg/m^{3})$	8166	0	0	0	0
	$\alpha(K^{-1})$	12.330×10^{-6}	0	8.085×10^{-4}	0	0
	$K(Wm/K)$	15.379	0	-1.264×10^{-3}	2.092×10^{-6}	-7.223×10^{-10}

Validation of the derived formulation is first confirmed by comparing the numerical results of the present paper with the data available in the literature. In Table 7.7, the frequency parameters, $\bar{\omega}=\omega L^2/h\sqrt{\rho_S/E_s}$ (where ω is the fundamental frequency and E_S, ρ_S are the Young's modulus and mass density of steel), at various values of the *UTR* and *NLTR* of this work, are compared to the results obtained by the differential transform method in [25].

Table 7.7: Comparison of frequency parameter $\bar{\omega}$ of FGM beam in thermal environment

		n=0.1		**n=0.2**		**n=0.5**		**n=1**	
ΔT		**[25]**	**Pr.**	**[25]**	**Pr.**	**[25]**	**Pr.**	**[25]**	**Pr.**
20*K*	***UTR***	4.6536	4.6053	4.3867	4.3514	3.8974	3.8767	3.5193	3.5046
	NLTR	4.7018	4.6598	4.4334	4.4089	3.9354	3.9384	3.5474	3.5678
40*K*	***UTR***	4.4516	4.3944	4.1782	4.1350	3.6779	3.6510	3.2925	3.2726
	NLTR	4.6020	4.5603	4.3279	4.3093	3.8141	3.8380	3.4114	3.4659
80*K*	***UTR***	4.0148	3.9377	3.7212	3.6610	3.1834	3.1441	2.7693	2.7399
	NLTR	4.3956	4.3546	4.1087	4.1031	3.5591	3.6292	3.1216	3.2531

As observed from the table, the results of the present work are in good agreement with those of [25]. To verify the formulation in evaluating the dynamic response of an FGM beam, the maximum dynamic amplification factor, *max*(*DAF*), and the corresponding velocity of a beam made of Al_2O_3 and aluminum (Al), previously investigated in [114], are computed and the result is given in Table 7.8.

Table 7.8: Comparison of maximum amplification factor and corresponding velocity of FGM beam at room temperature

n	**Present**		**[114]**	
	***max*(*DAF*)**	***v*(*m/s*)**	***max*(*DAF*)**	***v*(*m/s*)**
0.2	1.0361	222	1.0344	222
0.5	1.1447	198	1.1444	198
1	1.2503	179	1.2503	179
2	1.3377	164	1.3376	164
Al2O3	0.9329	252	0.9328	252
SUS304	1.7326	132	1.7324	132

Note that the beam with data given in [114] was used in the analysis and *DAF* is defined in the same way as that of an isotropic beam carrying a moving load, i.e.

$$DAF = \max\left[w_0(L/2,t)/w_{ost} \right] \tag{7.3}$$

where $w_{0st} = F_0L^3/48E_mI$ is the maximum static deflection of the pure metal beam under a load F_0. As seen from Table 3.24, the maximum *DAF* and the corresponding velocity of the present work are in good agreement with those of [114]. It is worth mentioning that the results in Tables 7.7 and 7.8 are converged by using 20 elements, and this number of elements will be utilized for all the numerical examples. The effect of material distribution on the dynamic behaviour of FGM beams in the thermal environment can be seen from Fig. 7.10, where the time histories for the normalized deflection are illustrated for various values of the grading index *n* and *v*=20 m/s, Ω=15 rad/s, $\Delta T = 50$K.

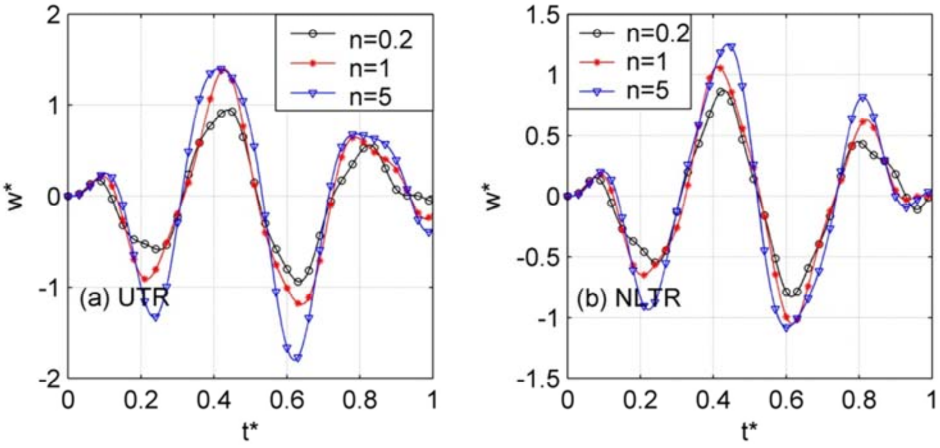

Figure 7.10: Time histories for normalized mid-span deflection for various values of index *n* ($v = 20$ m/s, $\Omega = 15$ rad/s, $\Delta T = 50$K)

In the figure and hereafter, the travelling time and the mid-span deflection are normalized by the total time and the maximum static deflection, that is $t^* = t/\sum T$ and $w^* = w_0(L/2, t)/w_{0st}$.

As seen from Fig. 7.10, at the given values of the moving load velocity, excitation frequency and temperature rise, the maximum mid-span deflection increases with the increase of the index *n*, regardless of the temperature. The curves for the time histories obtained in the *UTR* are similar to those obtained in the *NLTR*, except for the higher amplitude. The increase of the mid-span deflection by raising the grading index *n* can also be seen from Fig. 7.11, where the relation between the *DAF* and the index *n* is depicted for different temperature rises.

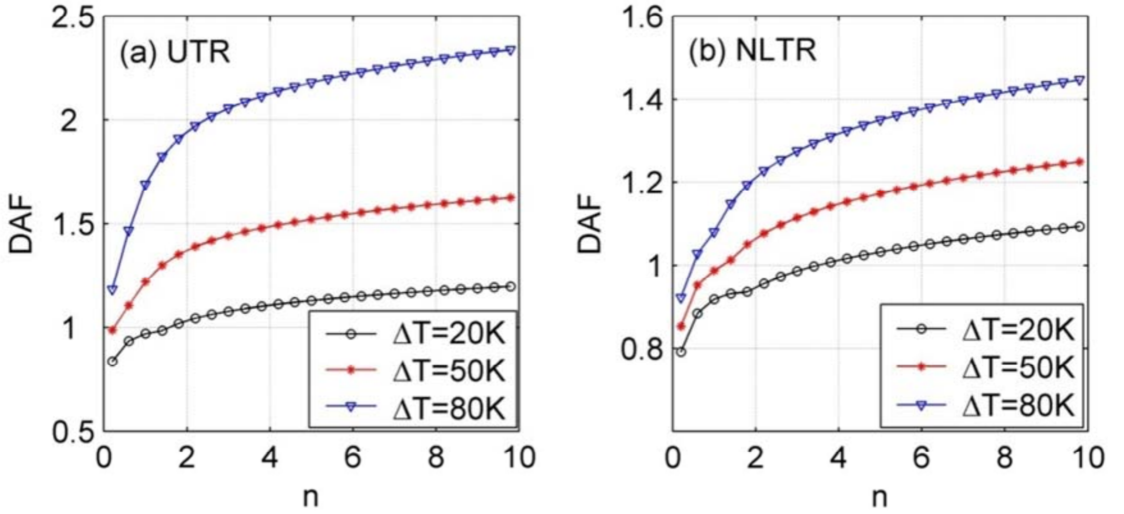

Figure 7.11: Relation between *DAF* and grading index *n* with different temperature rises ($v = 30$ m/s, $\Omega = 0$)

The *DAF* values steadily increase with the increase in the index *n*, irrespective of the temperature distribution. The *DAF* of the beam subjected to *NLTR* is smaller than that of the beam under *UTR*, but the relations between *DAF* and *n* for the two temperature distributions are very similar. The influence of the temperature rise on the dynamic behaviour of the FGM beam is illustrated in Figs. 7.12–7.14. The maximum mid-span deflection of the beam, as seen from Fig. 7.12, increases by both the *UTR* and *NLTR*.

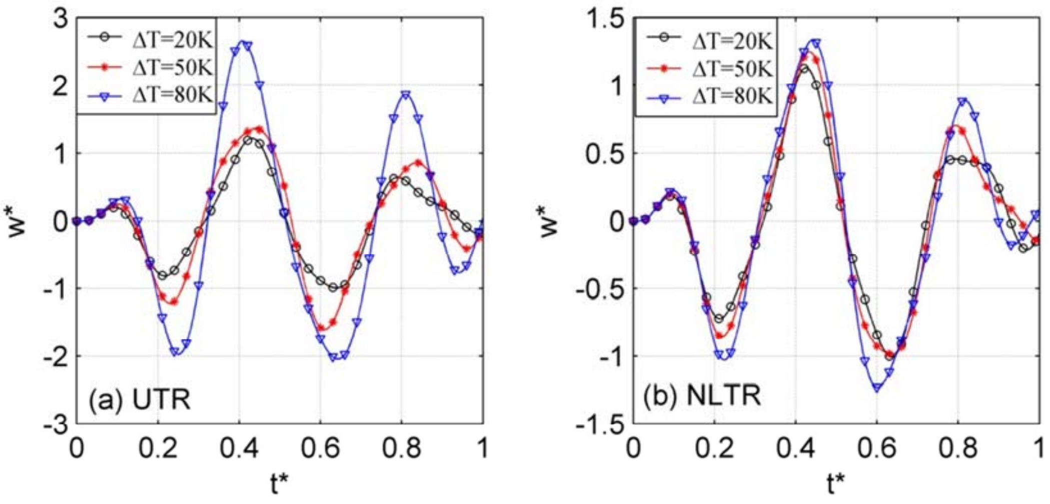

Figure 7.12: Effect of temperature rise on time histories for normalized mid-span deflection for $n = 3$, $v = 20$ m/s, $\Omega = 15$rad/s

The situation for the *DAF*, as can be seen in Fig. 7.13, is similar, and the *DAF* increases with increasing temperature. The influence of the *UTR* is more significant than that of the *NLTR*, and the *DAF* increases more significantly by the *UTR*.

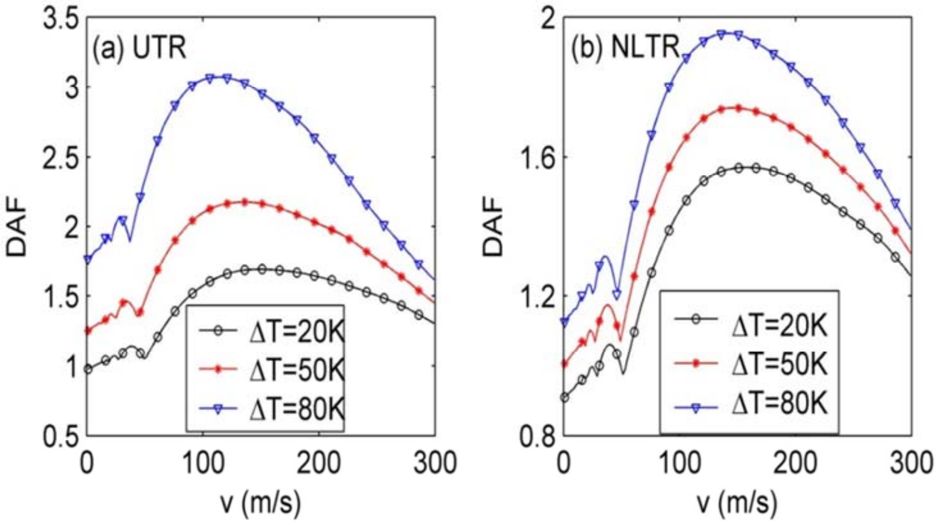

Figure 7.13: Relation between *DAF* and moving load velocity v for various temperature rises and $n = 3$, $\Omega = 0$

The curves exhibit that the relation between the *DAF* and the moving load velocity has similar forms to that of a homogeneous beam subjected to a moving force [101], and the *DAF* experiences a repeated increase and decrease period before reaching a peak value, regardless of the temperature rise. The increase of the *DAF* with the temperature rise can also be seen from Table 7.9, where the *DAF* is given for various values of the moving load velocity, the temperature rise and the grading index n.

Table 7.9: *DAF* for different values of moving load velocity, temperature rise and index n

	***v*(*m/s*)**	**Δ*T* (*K*)**	***n* =0.1**	***n* = 0.2**	***n* = 0.5**	***n* = 1**	***n* = 2**	***n* = 5**
UTR	**25**	**50**	0.9173	0.9562	1.1114	1.2334	1.3043	1.4525
		100	1.2536	1.3929	1.6645	2.1392	2.6394	3.1685
	50	**50**	1.0034	1.0633	1.1657	1.2114	1.3902	1.6104
		100	1.3454	1.4349	1.7777	2.4255	3.1721	4.1644
NLTR	**25**	**50**	0.814	0.8442	0.9223	1.0174	1.083	1.1336
		100	0.9097	0.9404	1.0823	1.1994	1.2767	1.4233
	50	**50**	0.8761	0.9222	1.0056	1.0551	1.0671	1.1749
		100	0.9937	1.0473	1.1415	1.1883	1.3397	1.5744

Irrespective of the moving load velocity and the index *n*, the *DAF* in the table clearly increases with the temperature rise. The axial stress at the mid-span section, as seen from Fig. 7.14, also increases with the temperature rise, and the increase of the stress by the *UTR* is more significant than by the *NLTR*.

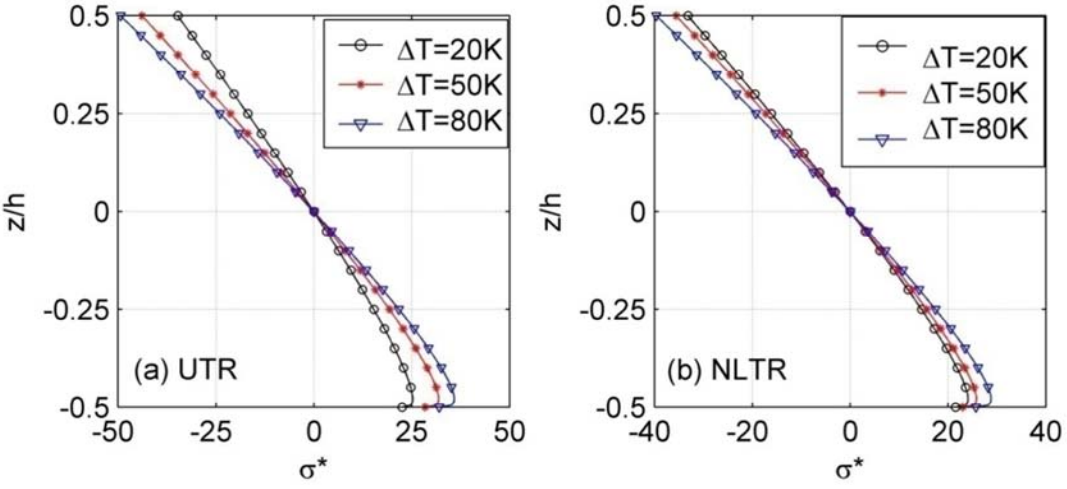

Figure 7.14: Effect of temperature rise on thickness distribution of normalized axial stress for $n = 0.3$, $v = 20$ m/s, $\Omega = 0$

The stress in Fig. 7.14 is calculated at the time when the load arrives at the mid-span and it is normalized by F_0/A.

In Fig. 7.15, the time histories for the normalized mid-span deflection are depicted for various values of the excitation frequency Ω and $n = 3$, $v = 20$ m/s, $\Delta T = 50$K.

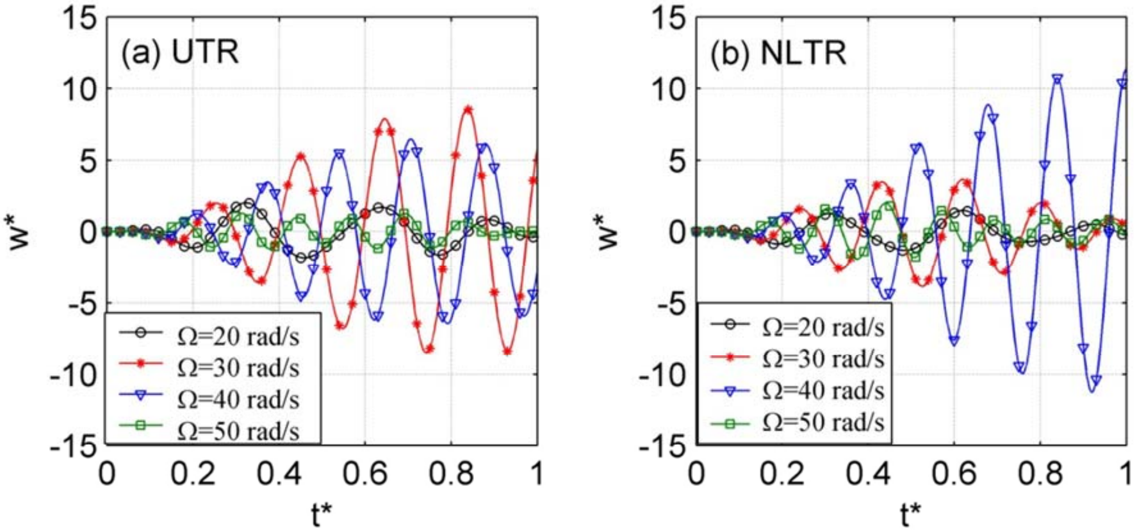

Figure 7.15: Time histories for normalized mid-span deflection for various values of excitation frequency $n = 3$, $v = 20$ m/s, $\Delta T = 50$K

The effect of the excitation frequency on the dynamic behaviour of the beam is clearly seen from the figure. The number of vibrations which the beam executes increases with the increasing excitation frequency. The vibration amplitude is much higher for the excitation frequency near the fundamental frequency, which is equal to 34.4359 rad/s and 38.4791 rad/s for the *UTR* and *NLTR* of the figure, respectively. The influence of the excitation frequency on the dynamic behaviour of the beam can be seen more clearly from Fig. 7.16, where the relation between the *DAF* and the excitation frequency is illustrated for different temperature rises and $n = 3$, $v = 20$m/s.

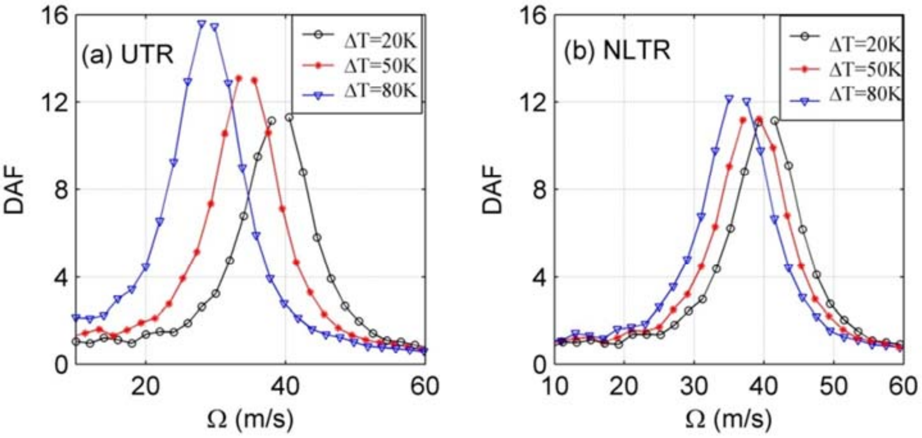

Figure 7.16: Relation of *DAF* and excitation frequency for different temperature rises ($n = 3$, v =20 m/s)

The *DAF* rapidly increases when the excitation frequency approaches the fundamental frequency, irrespective of the temperature rise. Since the damping effect is ignored in the present work, resonance will occur, and the *DAF* becomes infinity when the excitation frequency equals the fundamental frequency. The excitation frequency at which the resonance can occur, as seen from Fig. 7.16, changes with the temperature of the environment, and this should be taken into consideration in designing FGM beams subjected to moving harmonic loads.

The resonant frequencies corresponding to the curves in Fig. 7.16 are 39.0262 rad/s, 34.4359 rad/s, 28.9872 rad/s for the *UTR* and 40.4788 rad/s, 38.4791 rad/s and 36.3454 rad/s for the *NLTR*.

7.2.2 Conclusions

The two main conclusions of the sub-section can be summarized as follows:

- The dynamic characteristics of FGM beams under a moving load, including the mid-span dynamic deflection, *DAF* and axial stress are significantly influenced by the temperature, and they are increased by the increase of the temperature rise. Of the two types of temperature distribution considered in the present work, the *UTR* has a stronger effect on the dynamic response than the *NLTR* does.
- The excitation frequency plays an important role in the dynamic behaviour of the FGM beams due to the moving harmonic load, and resonance can occur when the excitation frequency and the fundamental frequency are identical. The resonant frequency, however, changes with the change of the environment temperature, and this should be taken into account in designing FGM beams in a thermal environment subjected to moving harmonic loads.

7.3 Single span with multiple moving loads

A simply-supported beam made of axially FGM (as in section 2.2.3) subjected to multiple moving loads is investigated, as shown in Fig. 7.17.

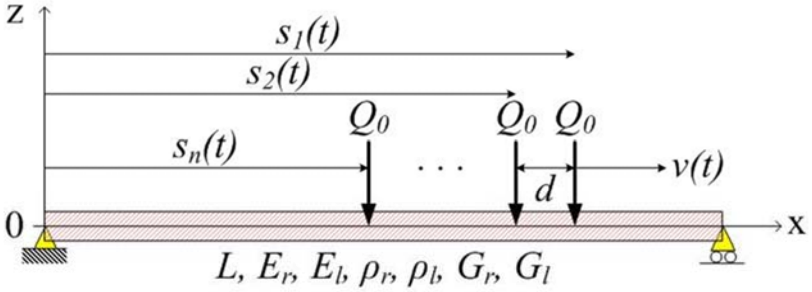

Figure 7.17: Simply-supported FGM beam subjected to multiple moving loads

Linear and Kosmatka shape functions are employed in this section as interpolation functions.

$$N_{u1} = \frac{l-x}{l} \quad , \quad N_{u2} = \frac{x}{l} \tag{7.4}$$

$$\begin{aligned}
N_{w1} &= \frac{1}{1+\lambda}\left[2\left(\frac{x}{l}\right)^3 - 3\left(\frac{x}{l}\right)^2 - \lambda\left(\frac{x}{l}\right) + (1+\lambda)\right] \\
N_{w2} &= \frac{l}{1+\lambda}\left[\left(\frac{x}{l}\right)^3 - \left(2+\frac{\lambda}{2}\right)\left(\frac{x}{l}\right)^2 + \left(1+\frac{\lambda}{2}\right)\left(\frac{x}{l}\right)\right] \\
N_{w3} &= -\frac{1}{1+\lambda}\left[2\left(\frac{x}{l}\right)^3 - 3\left(\frac{x}{l}\right)^2 - \lambda\left(\frac{x}{l}\right)\right] \\
N_{w4} &= \frac{l}{1+\lambda}\left[\left(\frac{x}{l}\right)^3 - \left(1-\frac{\lambda}{2}\right)\left(\frac{x}{l}\right)^2 - \frac{\lambda}{2}\left(\frac{x}{l}\right)\right]
\end{aligned} \tag{7.5}$$

$$\begin{aligned}
N_{\theta 1} &= \frac{6}{(1+\lambda)l}\left[\left(\frac{x}{l}\right)^2 - \left(\frac{x}{l}\right)\right] \\
N_{\theta 2} &= \frac{l}{1+\lambda}\left[3\left(\frac{x}{l}\right)^2 + (4+\lambda)\left(\frac{x}{l}\right) + (1+\lambda)\right] \\
N_{\theta 3} &= -\frac{6}{(1+\lambda)l}\left[\left(\frac{x}{l}\right)^2 - \left(\frac{x}{l}\right)\right] \\
N_{\theta 4} &= \frac{l}{1+\lambda}\left[3\left(\frac{x}{l}\right)^2 - (2-\lambda)\left(\frac{x}{l}\right)\right]
\end{aligned} \tag{7.6}$$

where $\lambda = \frac{12}{l^2}\frac{E_0\, I_0}{\psi\, G_0\, A_0}$ with A_0, I_0, E_0, G_0 are the cross-section area, moment of inertia, Young's and shear moduli of the homogeneous uniform beam, respectively.

Otherwise stated, the geometric data for the beam are: b_m=0.5m, h =1m, L=5m and 20m, where b_m, h, and L are the width of the mid-span cross section, height and total length of the beam, respectively.

The beam is assumed to be composed of steel and alumina with data about the Young's modulus and mass density as in section 7.1. The beam material is graded, with pure alumina at the left end and pure steel at the right end. The amplitude of each load is Q_0 =100 kN. A Poisson's ratio ν=0.3 and a shear correction factor κ=5/6 are used in all the computation in this section. The total time ΔT necessary for a constant moving speed load to cross the beam is L/v, where v is the moving speed of the load. In the computation, a prismatic time increment of $dt = \Delta T/500$ is used for the Newmark method.

The dimensionless parameters representing the maximum mid-span deflection and moving load speed are introduced as

$$f_D = \max\left(\frac{w(L/2,t)}{w_0}\right) \qquad f_v = \frac{\pi v}{w_1^0} \tag{7.7}$$

where $w_0 = Q_0L^3/48E_rI_m$ is the static deflection of a prismatic steel beam under a static load Q_0 acting at the mid-span, and $\omega_1^0 = \left(\frac{\pi^2}{L^2}\right)\sqrt{\frac{E_rI_m}{\rho_rA_m}}$ is the fundamental frequency of the simply supported prismatic steel beam. f_D is called the dynamic deflection factor.

7.3.1 Verification of formulation

In order to verify the accuracy of the non-prismatic FGM beam in sub-section 2.2.3 within the derived formulation in section 3.3, the fundamental frequencies of a prismatic FGM beam composed of steel and alumina are computed and compared with the numerical results of reference [117].

To this end, for consistency with [117], an FGM beam with width $b = 0.4$ m, height $h = 0.9$ m and length $L = 20$ m is employed in the computation.

Tables 7.10–7.11 list the values of the first two non-dimensional fundamental frequencies of the beam with various values of the modulus ratio, $E_{ratio} = E_l/E_r$, and the power law index n for an assumed constant value of mass density, $\rho_{ratio} = \rho_l/\rho_r = 1$.

Table 7.10: First dimensionless frequency parameter of prismatic FGM beam

	Power law index *n*					
	1		**2**		**5**	
E_{ratio}	**Present**	**[117]**	**Present**	**[117]**	**Present**	**[117]**
0.25	2.7482	2.7532	2.9220	2.9278	3.0772	3.0834
0.5	2.9056	2.9104	3.0069	3.0122	3.0997	3.1052
1	3.1350	3.1399	3.1350	3.1399	3.1350	3.1399
2	3.4554	3.4611	3.3193	3.3243	3.1877	3.1922
4	3.8866	3.8937	3.5737	3.5794	3.2625	3.2667

Table 7.11: Second dimensionless frequency parameter of prismatic FGM beam

	Power law index *n*					
	1		**2**		**5**	
E_{ratio}	**Present**	**[117]**	**Present**	**[117]**	**Present**	**[117]**
0.25	5.4372	5.4729	5.7283	5.7675	6.0213	6.0639
0.5	5.7685	5.8047	5.9359	5.9739	6.1060	6.1459
1	6.2317	6.2703	6.2317	6.2703	6.2317	6.2703
2	6.8599	6.9030	6.6372	6.6782	6.4094	6.4482
4	7.6893	7.7399	7.1755	7.2208	6.6495	6.6900

Very good agreement between the frequencies obtained in the present work and those of the reference [117] is shown in the tables. The non-dimensional fundamental frequency in the tables is defined as

$$\mu^2 = \frac{\omega^2 \rho_r A_m L^2}{E_r I_m} \tag{7.8}$$

where ω is the natural frequency of the beam.

To verify the element formulation further, the maximum dynamic deflection factor and its corresponding speed of an axially FGM beam are evaluated and compared with the published data [117]. The computed result is listed in Table 7.12 for various values of the index n, where the numerical results from [117] are also given.

Table 7.12: Maximum normalized dynamic deflection factors of the beam and corresponding speeds for $\alpha = 0$, $L/h = 20$

index *n*	***v* [*m/s*]**		***max*(*fD*)**	
	Present	**[117]**	**Present**	**[117]**
0.3	219	220	1.0195	1.01947
1	178	179	1.2064	1.20435
3	144	144	1.5146	1.51669
Pure Steel	132	132	1.7386	1.73247

The numerical results shown in Table 7.12 were obtained by varying the moving speed with an increment of 1m/s. Very good agreement between the results is achieved. It should be noted that the numerical results listed in Tables 7.10–7.12 have been obtained by using *10 elements*.

In order to verify the formulation and numerical procedure in modelling multiple moving loads, the time history for mid-span deflection of a prismatic homogeneous beam subjected to three point loads Q_0=5324.256 N , moving with a constant speed v=22.5 m/s, is computed and the result is shown in Fig. 7.18, where the numerical result obtained by using the dynamic stiffness method in [45] is depicted by small circles.

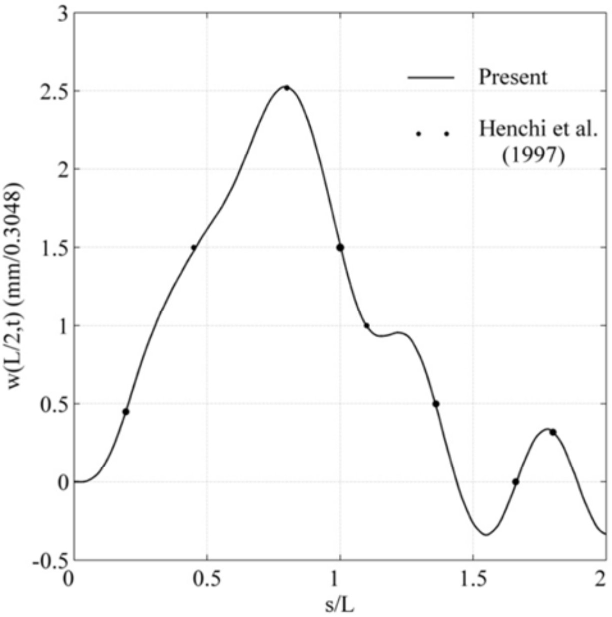

Figure 7.18: Time history for mid-span deflection of uniform homogeneous beam under three moving loads $d = L/4$

The beam material properties and geometric data in this computation, adopted from

[45], are as follows: L= 24.384 m, m=9.576×10^3 kg/m, A =0.576 m, I=2.95×10^{-3} m^4, E=19×10^{11} N/m^2, where L, m, A, I, E are the total length, mass per unit length, section area, moment of inertia and Young's modulus, respectively. Good agreement between the numerical results of the present work and those of [45] is observed from the figure.

7.3.2 Fundamental frequency

The effect of the section parameter α on the non-dimensional fundamental frequency μ_1 of the Type A FGM beam having the aspect ratio, L/h, is shown in Fig. 7.19 for an index n =3.

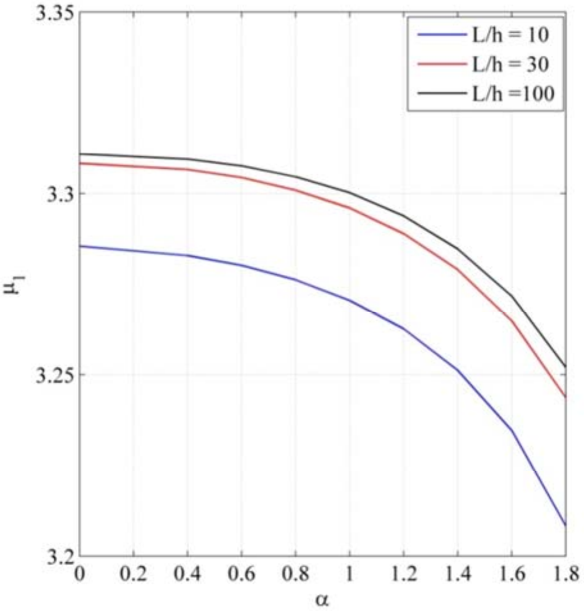

Figure 7.19: Effect of section parameter on the dimensionless fundamental frequency of type A FGM beam with different values of the aspect ratio (n=3)

It can be observed that the fundamental frequency of the beam is considerably affected by the section parameter and the aspect ratio. The frequency μ_1 steadily reduces by raising the section parameter α, regardless of the aspect ratio. In addition, the frequency is smaller for a beam associated with a lower aspect ratio. In other words, the shear deformation which has been taken into account in the present work reduces the fundamental frequency of the FGM beam. Thus, the numerical result obtained in this sub-section shows the good ability of the proposed formulation in modelling the shear deformation of the FGM beam.

It should be noted that the frequency parameter shown in Fig. 7.19 has been obtained by using *28 elements*, which is much more than the number of elements previously used for the prismatic beam.

As seen from Table 7.13, the convergence of the fundamental frequency of the non-prismatic FGM beams depends on the section parameter, and the beam with a higher section parameter requires a greater number of elements in evaluating the fundamental frequencies.

Table 7.13: Convergence of present elements in evaluation of fundamental frequency μ_1 of non-prismatic FGM beam with various values of α (n=1, L/h =20)

Number of elements *nel*	α			
	0.5	**1**	**1.5**	**1.8**
4	3.5007	3.4923	3.4706	3.4427
8	3.4993	3.4902	3.4668	3.4369
12	3.4991	3.4898	3.4657	3.4346
14	3.4991	3.4897	3.4654	3.4338
16	3.4991	3.4896	3.4652	3.4333
18	3.4990	3.4895	3.4650	3.4328
20	3.4990	3.4894	3.4648	3.4322
22	3.4990	3.4894	3.4647	3.4319
24	3.4990	3.4894	3.4646	3.4315
26	3.4990	3.4894	3.4646	3.4313
28	3.4990	3.4894	3.4646	3.4313

7.3.3 Effect of material non-homogeneity

The material non-homogeneity distribution along the longitudinal direction is defined through the power law index n in Eq. (2.37), and the effect of this index on the dynamic response of the beam is examined in this sub-section.

In Fig. 7.20, the relation between the deflection factor and the speed parameter of the Type A beam subjected to a single moving load is depicted for a non-prismatic section parameter α = 0.5, and for two aspect ratios, L/h = 5 and L/h = 20.

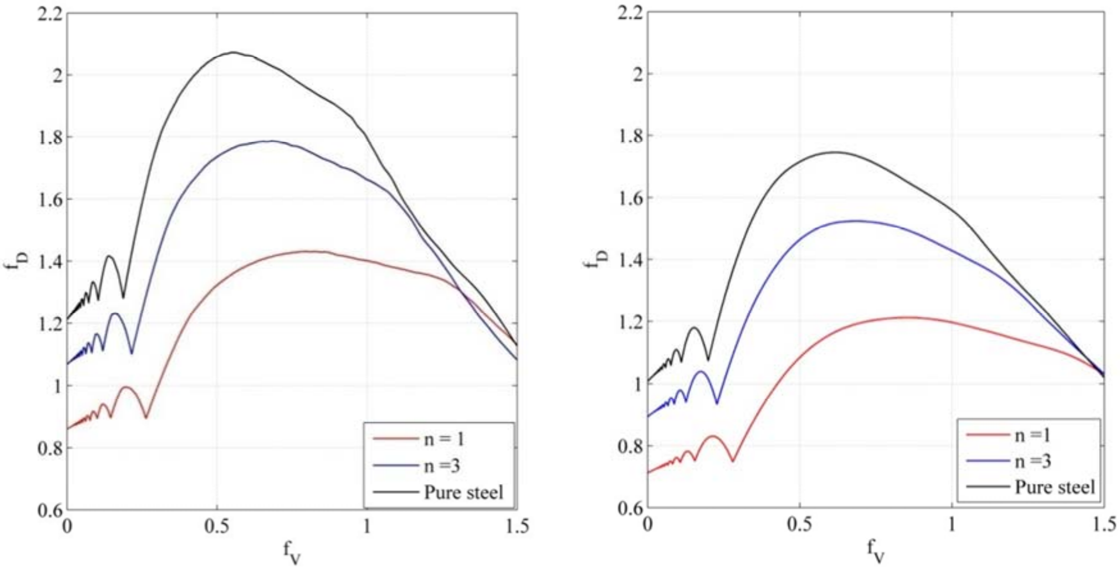

One load with *L/h*=5 One load with *L/h*=20

Figure 7.20: Relations of deflection factor and moving speed parameter of Type *A* beam ($\alpha = 0.5$)

As depicted in the figure, the dynamic deflection f_D is higher for a beam associated with a higher index *n*, regardless of the moving speed and the aspect ratio. This is due to the fact that, referring to Eq. (2.37), the beam with a higher index *n* contains more steel and thus it is softer. The dependency of the deflection factor f_D upon the speed parameter f_v observed from Fig. 7.20 is similar to that of the homogeneous beams in [95], where f_D increases when increasing the speed parameter f_v, and it then reduces after reaching a peak value, regardless of the index *n* and the aspect ratio. The effect of the material non-homogeneity and the moving speed on the dynamic deflection factor can also be observed clearly from Fig. 7.21, where the relation between f_D and the index *n* of the Type *A* beam are shown for various values of the speed parameter f_v and for a section parameter $\alpha = 0.5$.

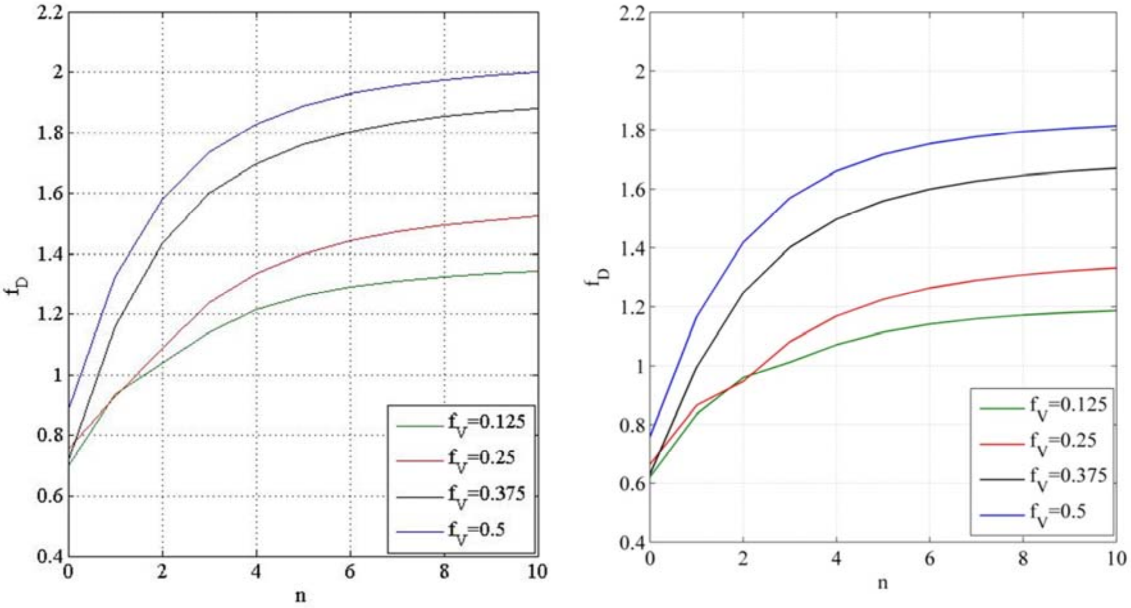

One load with *L/h*=5 One load with *L/h*=20

Figure 7.21: Relations of deflection factor and power law index of Type *A* beam ($\alpha = 0.5$)

The effect of the aspect ratio on the dynamic response of the beam can be seen from Figs. 7.20 and 7.21, where f_D is higher for a beam having a smaller aspect ratio. The dynamic deflections in this sub-section have been computed by using *28 elements*.

7.3.4 Effect of section profile

The time histories for mid-span deflection of the Type *A* beam under a single moving load are shown in Fig. 7.22 for various values of the section parameter α, and for $n = 5, f_v = 0.25$.

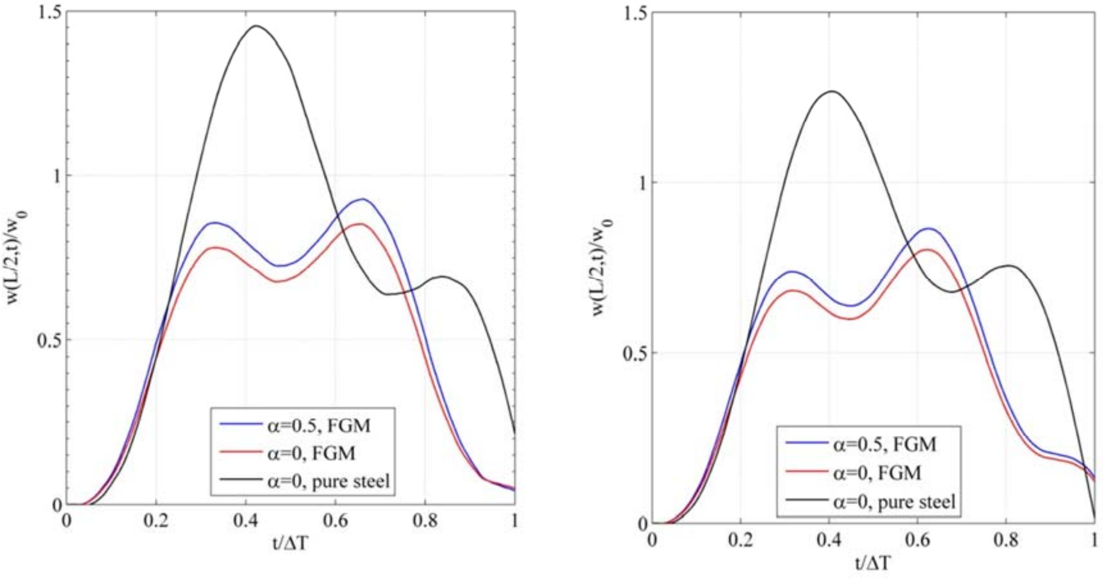

One load with *L/h*=5 One load with *L/h*=20

Figure 7.22: Time histories of normalized mid-span deflection of Type *A* beam under a single moving load (*n*= 5, f_v = 0.25)

The dynamic response of the beam, as clearly observed from Fig. 7.22, is greatly affected by the section parameter, where the maximum dynamic deflection is higher for a beam having a larger parameter α, regardless of the aspect ratio. Except for the amplitude of the dynamic deflection, the aspect ratio hardly changes the dynamic behaviour of the beam. In Fig. 7.23, the relation between the maximum deflection parameter, $max(f_D)$, and the section parameter α of the beam having different aspect ratios is depicted for the two types of section profile and for n = 5, f_v = 0.25.

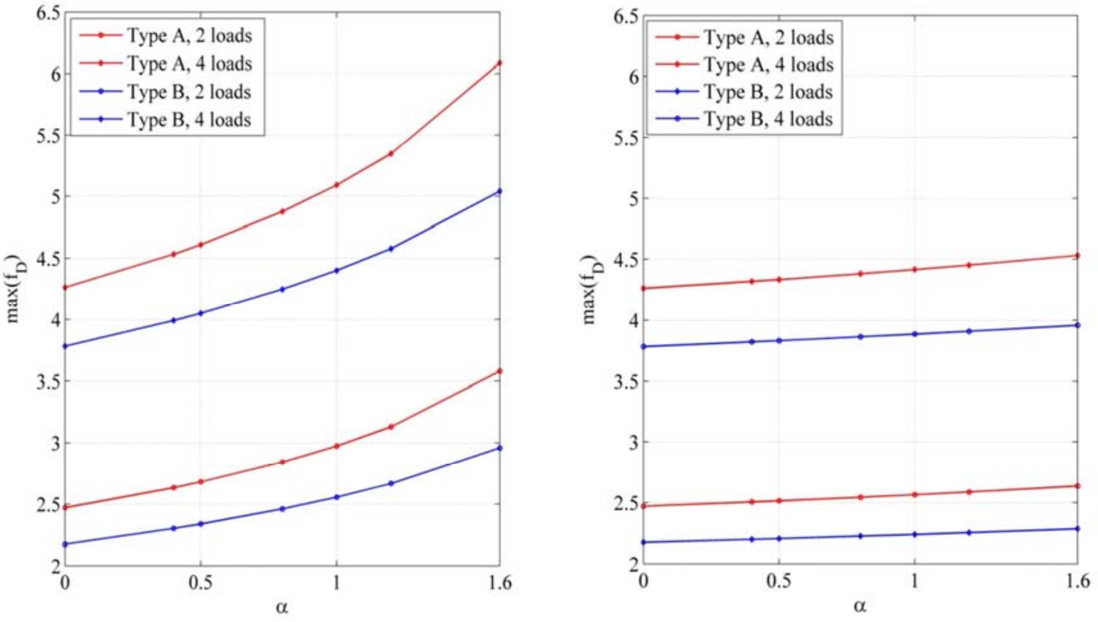

L/h=5*, d*=*L*/10 *L/h*=20*, d*=*L*/10

Figure 7.23: Effect of section profile on relation between maximum deflection factor and non-uniform parameter (n = 5, f_v = 0.25)

As shown in Fig. 7.23, the maximum deflection factor of the beam with the Type *A* section is more sensitive to the non-prismatic section parameter α compared to that of the Type *B* beam, regardless of the number of moving loads. For a given value of the parameter α and number of moving loads, the maximum deflection factor of the Type *A* beam is higher than that of the Type *B* beam and the difference becomes larger for a higher value of α. The aspect ratio affects the amplitude of the maximum deflection factor, but it hardly changes the relation between this factor and the non-prismatic parameter. This maximum deflection factor of the beam associated with a lower aspect ratio is much more sensitive to the change of the section parameter compared to the beam having a higher aspect ratio.

7.3.5 Effect of distance between loads

The time histories for mid-span deflection of the Type *A* beam under four moving loads are depicted in Fig. 7.24 for various values of the distance between the loads and for n=3, f_v = 0.25, *L/h* = 20.

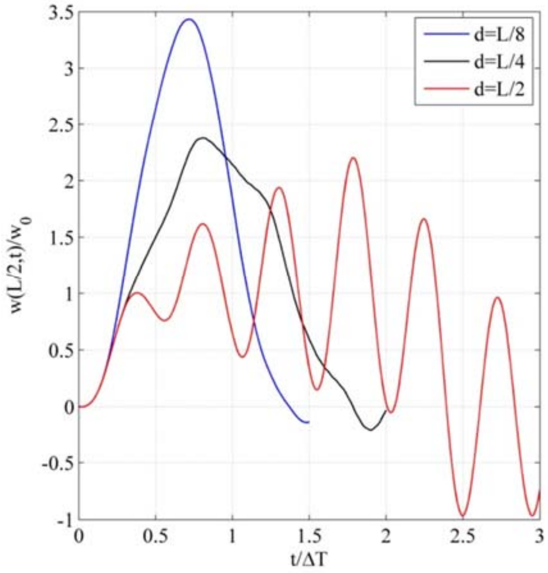

Figure 7.24: Time histories for mid-span deflection of Type *A* beam under 4 loads (n = 3, f_v = 0.25, L/h = 20, α = 0.5)

In Fig. 7.25, the relation between the deflection parameter f_D and the moving speed f_v of the Type *A* beam is shown for various values of the distance between the loads, and for n =3, α=0.5, L/h=20.

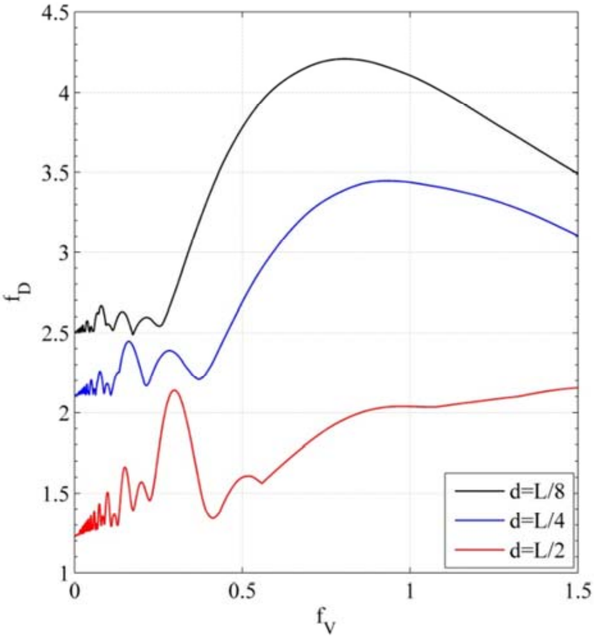

Figure 7.25: Deflection of factor-speed parameter of Type *A* beam under 3 loads (n = 3, L/h = 20, α = 0.5)

The effect of the distance between the moving loads on the dynamic behaviour of the beam is clearly depicted in the figures. The dynamic deflection factor is much larger when the distance between the loads is smaller, regardless of the moving speed.

7.3.6 Conclusions

The sub-section studied the dynamic response of non-prismatic axially FGM Timoshenko beams subjected to multiple moving point loads. The following conclusions can be drawn:

- The section profile and the aspect ratio have a considerable effect on the fundamental frequency and the dynamic deflection of the beam. The frequency steadily reduces by raising the section parameter and is smaller for a beam with a lower aspect ratio, while the dynamic deflection is higher for a beam with a larger parameter α and a lower aspect ratio.
- The dynamic deflection of the beam is also affected by the material distribution and the distance between moving loads. This deflection is higher for a beam with a higher index n and is much larger when the distance between loads is smaller.

Chapter 8: Post-buckling analysis of FGM structures

The post-buckling behaviour of structures is very important information for design engineers. Meanwhile, establishing equilibrium paths is the most common way of understanding a structure's behaviour in the post-buckling state. However, a major difficulty is the geometric non-linearity when the structure undergoes large displacement. Due to this challenge, it is difficult to understand the post-buckling problem using analytical methods, and a numerical method, especially the finite element method, is often employed instead. In order to analyze the large displacements of structures by the finite element method, a non-linear finite element which makes it possible to model the non-linear behaviour of the structures accurately is required. Many non-linear finite elements in general and beam elements in particular are available in the literature, some of which have been documented in well-known textbooks [143], [8]. The non-linear beam elements can be classified into three types, namely the total Lagrange formulation, the updated Lagrange formulation, and the co-rotational formulation. The co-rotational approach which is described in sub-section 4.1 will be used for the post-buckling analysis in this work.

8.1 Axially FGM structures

8.1.1 Rod

The effects of support conditions on the post-buckling behaviour of a Williams toggle frame consisting of rod structures made of axially FGM are presented in this section.

The shape functions used to interpolate the rod structures are displayed in subsection 2.3.3. Fig. 8.1 shows various support conditions of the Willams toggle frames for studying the effects on the post-buckling behaviour of axially FGM rods.

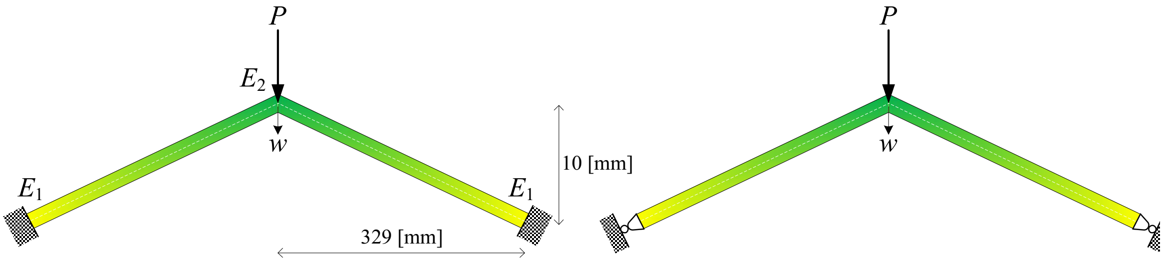

a) Fixed-Fixed support condition

b) Pinned-Fixed support condition

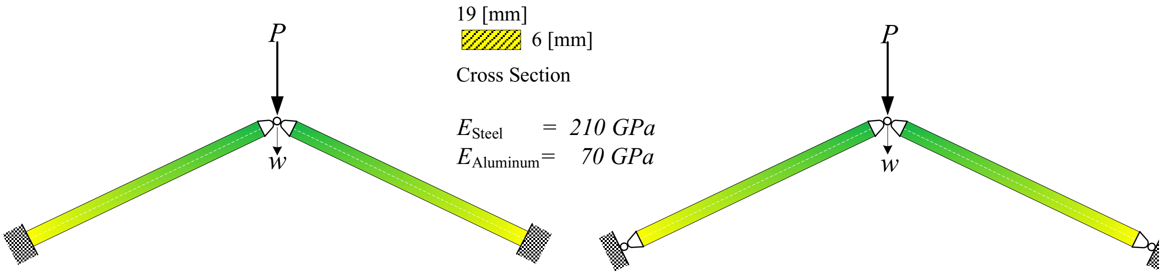

c) Fixed-Pinned support condition

d) Pinned-Pinned support condition

Figure 8.1: Various support conditions

The effects of the various support conditions on the axially FGM material distribution in the rods are shown in Figs. 8.2–8.5.

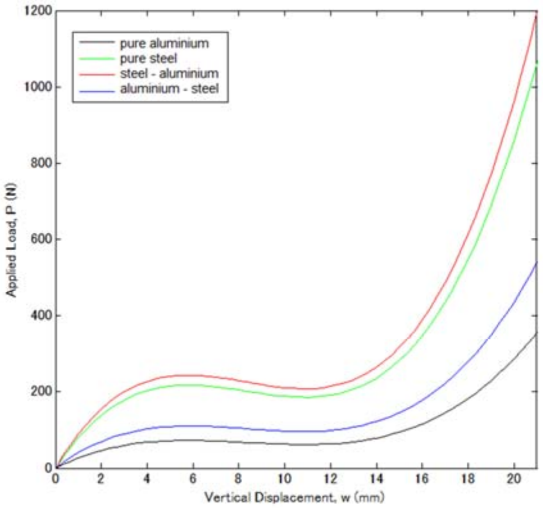

Figure 8.2: Fixed–Fixed support conditions

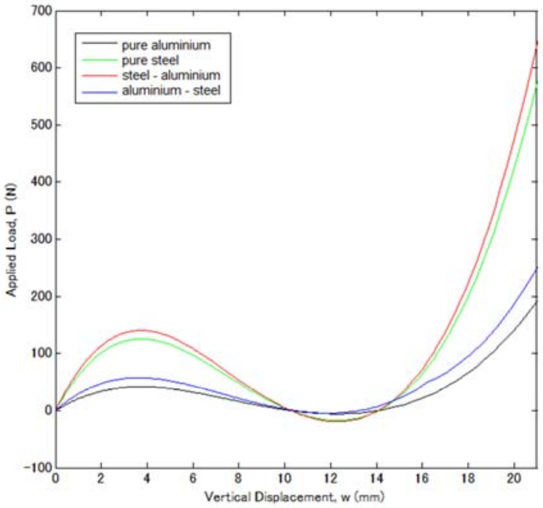

Figure 8.3: Pinned–Fixed support conditions

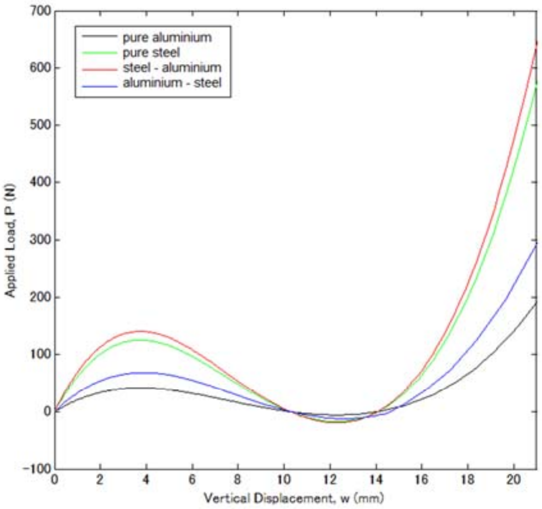

Figure 8.4: Fixed–Pinned support conditions

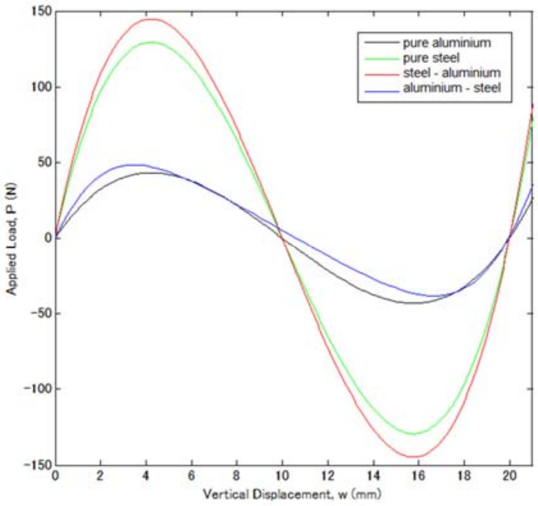

Figure 8.5: Pinned–Pinned support conditions

From these figures, the following conclusions can be drawn:

- The mixture of two constituents can increase the post-buckling behaviour of the axially FGM rod element compared with their pure constituents, regardless of the support conditions.
- The post-buckling behaviour of aluminium–steel axially FGM showed greater improvements compared with the steel–aluminium axially FGM

improvements. Therefore, the orientation of the material distributions combined with the supporting conditions can be used to maximize the performance of axially FGM rods in their post- buckling behaviour.

- It can be observed that the steel–aluminium axially FGM increased the performance of the rod element in the post-buckling behaviour, regardless of the variety of support conditions.

The effects of axially FGM material distributions in the rods for various support conditions are shown in Figs. 8.6–8.9.

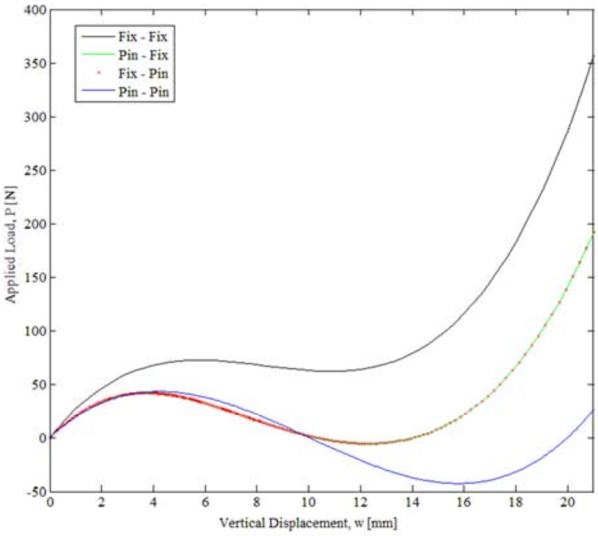

Figure 8.6: Pure aluminium material

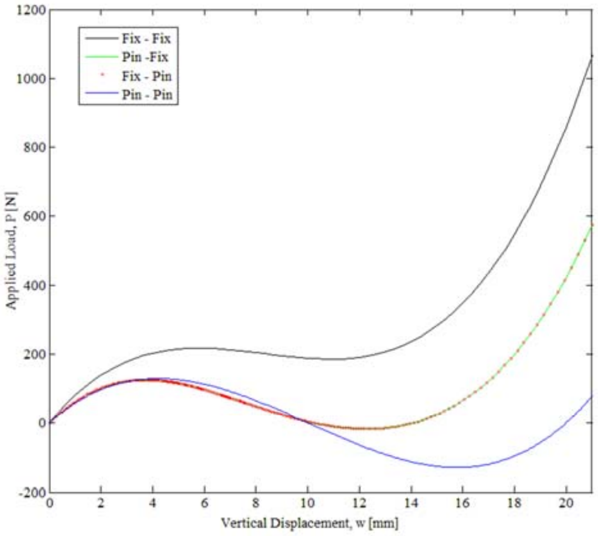

Figure 8.7: Pure steel material

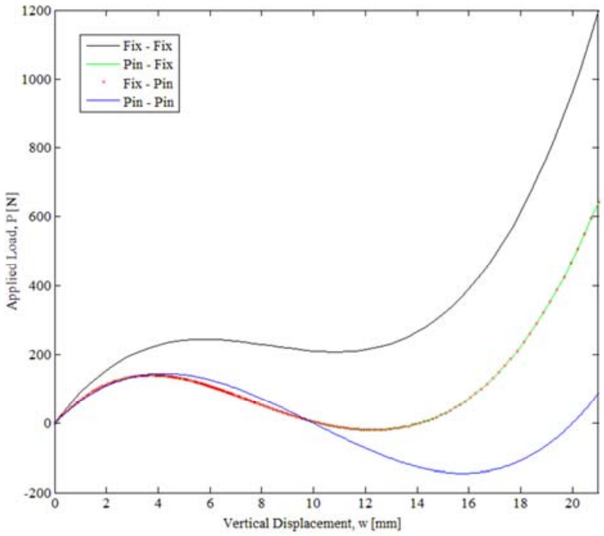

Figure 8.8: Steel–aluminium axially FGM

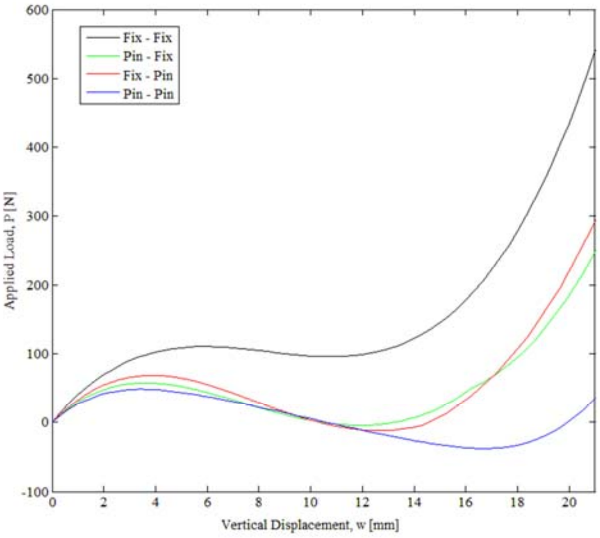

Figure 8.9: Aluminum–steel axially FGM

From these figures, the following conclusions can be drawn:

- In the post-buckling behaviour, the Fixed–Fixed support condition showed better performance of the axially FGM rod regardless of the material distributions.
- Similar performances were observed for pure aluminium, pure steel and steel–aluminium axially FGMs with Fixed–Pinned and Pinned–Fixed support conditions. However, the aluminium–steel axially FGM showed slight deviation of the response curves.

8.1.2 Beam and frame

8.1.2.1 Material verification

In order to facilitate the presentation of results, the following dimensionless parameters are introduced as

$$\mu^2 = \frac{\omega^2 \rho_0 A L^4}{E_0 I}$$
$$\bar{P} = \frac{P_{cr} L^2}{E_0 I}, \quad r = \frac{I}{A L^2} \tag{8.1}$$

Firstly, in Table 8.1, the paper verifies the accuracy of the proposed formulation and the numerical procedure in homogeneous beams under various boundary conditions of Clamped–Clamped, Clamped–Fixed and Hinged–Hinged, in which r is set to 0.01, shear correction factor $\kappa = 5/6$, Poisson's ratio $\nu = 0.3$, P=1, $E_0 = 70$ GPa, $\rho_0 = 2702\ \text{kg/m}^3$.

Table 8.1: Dimensionless critical load of uniform homogeneous Timoshenko beam

Boundary condition	**C-C**	**H-H**	**C-F**
Present	17.6901	7.5464	2.2910
[22]	17.7056	7.5472	2.2911
[137]	17.6896	7.5460	2.2910

Uniform axially FGM beams with Young's modulus and mass density of the beams vary as follows:

$$E(x) = E_0\left(1 + \frac{x}{L}\right)$$
$$\rho(x) = \rho_0\left[1 + \frac{x}{L} + \left(\frac{x}{L}\right)^2\right] \tag{8.2}$$

are also employed for further verification in Table 8.2.

Table 8.2: Dimensionless critical load of uniform axially FGM Bernoulli beam

Boundary condition	**C-C**	**H-H**	**C-F**
Present	57.3942	14.5113	3.1177
[22]	57.3940	14.5112	3.1177
[113]	57.3948	14.5113	3.1177

Very good agreement between the critical loads obtained in this work and those of the comparison reference can be seen in the tables.

8.1.2.2 Cantilever beam under tip moment

Consider a cantilever beam with total length $L = 6$ m, width $b = 0.15$ m and height $h = 0.1$ m subjected to a tip moment M.

The problem was investigated analytically by Kang and Li [60] with the expressions for the tip displacements as follows:

$$\begin{aligned} u &= \frac{E\big|_{x=L} I}{M} \sin\left(\frac{M}{E\big|_{x=L} I} L \right) - L \\ w &= \frac{E\big|_{x=L} I}{M} \left[1 - \cos\left(\frac{M}{E\big|_{x=L} I} L \right) \right] \end{aligned} \tag{8.3}$$

Table 8.3 displays the tip displacement of cantilever beams made of steel and alumina under tip moments computed by different shape functions.

Table 8.3: Tip displacement of cantilever beam under tip moment

ML/E_0I	**nELE**	**Kosmatka functions**		**New shape functions**	
		|u/L|	**w/L**	**|u/L|**	**w/L**
3	**1**	0.3919	0.6561	0.3816	0.6466
	2	0.3900	0.6521	0.3816	0.6466
	4	0.3876	0.6506	0.3816	0.6466
	6	0.3872	0.6488	0.3816	0.6466
	8	0.3865	0.6472	0.3816	0.6466
	10	0.3858	0.6470	0.3816	0.6466
	12	0.3842	0.6468	0.3816	0.6466
	14	0.3835	0.6467	0.3816	0.6466
	16	0.3820	0.6466	0.3816	0.6466
	20	0.3817	0.6466	0.3816	0.6466
6	**1**	1.1324	0.6306	1.0278	0.6179
	2	1.1289	0.6293	1.0276	0.6178
	4	1.1251	0.6289	1.0276	0.6178
	6	1.1203	0.6272	1.0276	0.6178
	8	1.1187	0.6267	1.0276	0.6178
	10	1.1151	0.6253	1.0276	0.6178
	12	1.0781	0.6241	1.0276	0.6178
	14	1.0512	0.6212	1.0276	0.6178
	16	1.0318	0.6190	1.0276	0.6178
	20	1.0278	0.6178	1.0276	0.6178

As can be seen from the table, quicker convergence can be reached by using the new shape functions compared to the linear and Kosmatka functions.

8.1.2.3 Cantilever beam subjected to eccentric axial load

Consider a cantilever beam subjected to an eccentric axial load, shown in Fig. 8.10.

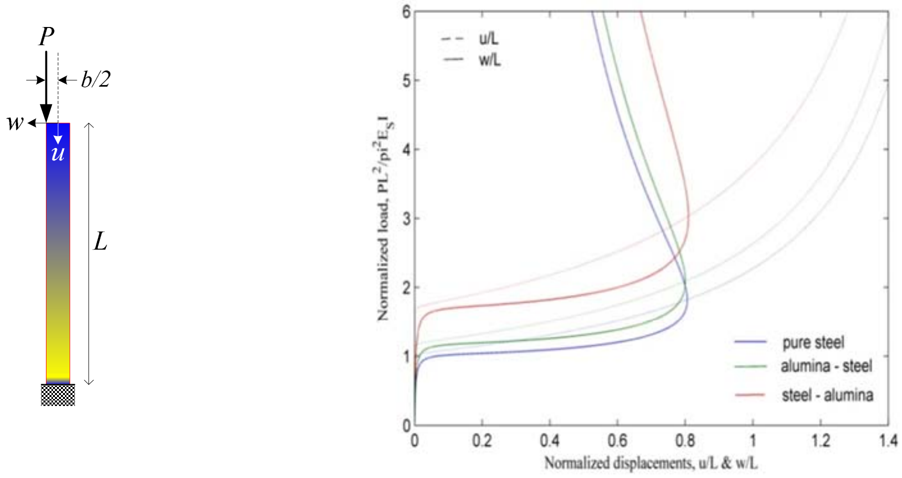

Figure 8.10: Load–displacement relation for cantilever beam under eccentric axial load

The beam data are: L=100 m, b=1 m, h =1 m and G= $E/2$.

The load–displacement curves are obtained by using a mesh of *three elements*. Good agreement between the curves computed in this work with those obtained by the references can be seen in the figure. The critical loads of the simply-supported beams made of steel and alumina with different numbers of elements are listed in Table 8.4.

Table 8.4: Dimensionless critical load of uniform steel–alumina beam

nELE	**Kosmatka functions**	**New shape functions**
1	16.5059	13.8780
2	14.0246	13.8763
3	13.9041	13.8752
4	13.8838	13.8745
5	13.8782	13.8745
6	13.8762	13.8745
7	13.8754	13.8745
8	13.8749	13.8745
9	13.8747	13.8745
10	13.8746	13.8745
11	13.8745	13.8745

The first row includes the number of elements, the second row shows the critical loads of the beam using the linear and Kosmatka functions for interpolation, and the last row displays the critical loads of the beam using the new derived shape functions. As can be seen from the table, the beam element based on the derived shape functions converges faster than the one based on the linear and Kosmatka functions.

8.1.2.4 Williams toggle frame

The Williams toggle frame (Fig. 8.11), which has been employed by many authors to test their non-linear beam elements is considered.

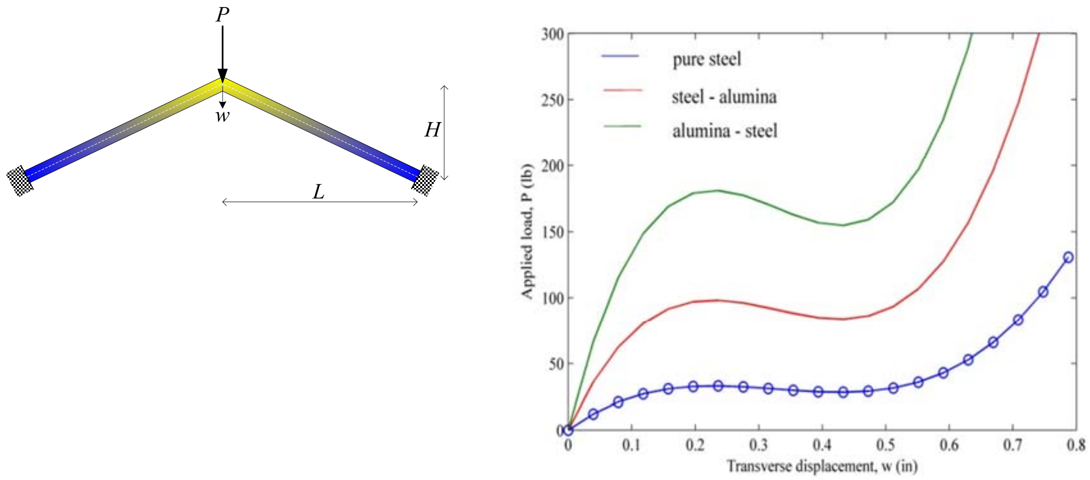

Figure 8.11: Load–displacement curves for Williams toggle frame

The data for computation are as follows: L=12.943 in (0.329 m), H=0.386 in (0.01 m), b= 0.753 in (0.019 m), h = 0.243 in (0.006 m), E_0 = 10.3×10^6 lb (7.1×10^4 MPa). In Fig. 8.11, the load–displacement curves for the frame are obtained by using only two beam elements. The blue curve corresponding to the homogeneous material shows a good agreement with the results obtained by Nguyen [89] which is shown in round blue circles. The effect of the material distribution on the limit load of the FGM frame is clearly seen from the figure. The pure steel material has the lowest limit load compared with the graded steel–alumina material. Putting the graded distribution of alumina at the fixed ends and the steel at the peak of the frame will give the highest limit load of the frame subjected to a vertical loading P.

8.1.2.5 Asymmetric frame

An asymmetric frame under a concentrated load is shown in Fig. 8.12. The frame is also known in the literature as Lee's frame, is investigated.

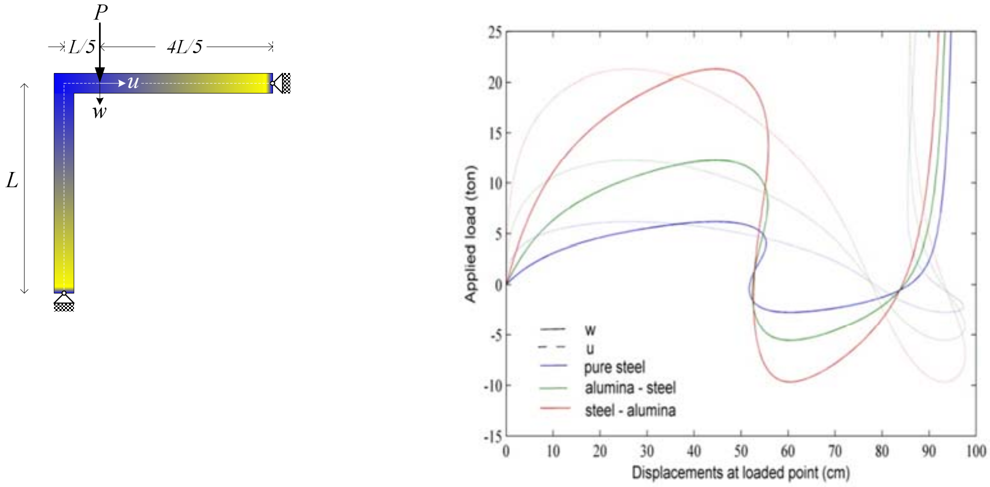

Figure 8.12: Load–displacement curves for asymmetric frame

The frame shows highly non-linear curves with snap-through and snap-back behaviour, and thus this problem is a good example to test the behaviour of the beam element and the proposed numerical algorithm. The frame is assumed to be composed of steel and alumina, where the geometric data are: L =120 cm, b = 3 cm and h = 2 cm.

Fig. 8.12 displays the load–displacement curves for the frame in two cases: blue for the pure steel frame and red for the steel–alumina frame.

The curves for the homogeneous frame are also depicted in the figure for comparison. Similarly to the previous example, placing the graded distribution with alumina at both hinged ends and steel at the joint of the frame will give the highest limit load of the frame subjected to a vertical loading P.

8.1.2.6 Conclusions

The following conclusions can be drawn:

- Consistency in using accurate shape functions which incorporate material in-homogeneity results in high efficiency in the finite element context, since the number of element divisions required can be significantly suppressed.
- FGM beams subjected to axial loading show improvements in limit of loading and non-linear behaviour in the post-buckling region.
- Gradation between two or more materials, i.e. FGM, is expected to give prospects of material optimization in structural designs.

Chapter 9: Elastic-plastic analysis of FGM structures

The elastic-plastic behaviour of FGM structures is very important phenomena for researchers. To establish the equilibrium paths after the material yield is a major difficulty because the structure undergoes large displacement. In order to analyze the large displacements of structures the co-rotational approach which is described in sub-section 4.1 will be used for the elastic-plastic analysis of FGM structures.

9.1 Elastic–plastic FGM beam subjected to eccentric axial load

9.1.1 Introduction

The analysis of elastic–plastic FGM structures has attracted some attention from researchers in recent years. In 2011, Gunes [42] employed the finite element code LS-DYNA to study the elastic–plastic response of FGM circular plates under low-velocity impact loads. A year later, Jahromi [55] adopted a bilinear stress–strain model in studying the elastic–plastic behaviour of an FGM rotating disk. The stress field of the disk is computed with the aid of the finite element package ABAQUS. In 2014, Huang [51], [52] used a multi-linear hardening elastic–plastic material to study the elastic–plastic buckling of FGM cylindrical shells under the axial and torsion loads, respectively. Also using the multi-linear hardening elastic–plastic material model, in 2015, Zhang [139] studied the buckling behaviour of elastic–plastic FGM cylindrical shells under a combination of the axial compressive load and external pressure. A detailed examination of the effects of dimensional parameters and elastic–plastic material properties on the stability region and elastic–plastic interface of the shells is given in [139] with the aid of the Galerkin method.

9.1.2 Numerical examples

The derived finite element formulation in sub-section 2.2.4 and the described numerical algorithm in sub-section 3.4 were implemented into a computer code for investigating the post-buckling behaviour of the FG beams.

The numerical result reported in this section has been performed for an FGM beam with length $L = 5\ m$, height $h = 0.1\ m$ and width $b = 0.2\ m$.

The properties of the constituent materials are adopted from [61] as follows: E_C = 80 GPa for ceramic, E_m = 56 GPa, σ_{Y_m}= 106 MPa, E_{tm} =12 GPa for metal, and q=17.2 GPa.

Figs. 9.1–9.2 show the variation of the Young's modulus and the yield stress in the thickness direction of the FG beam, respectively.

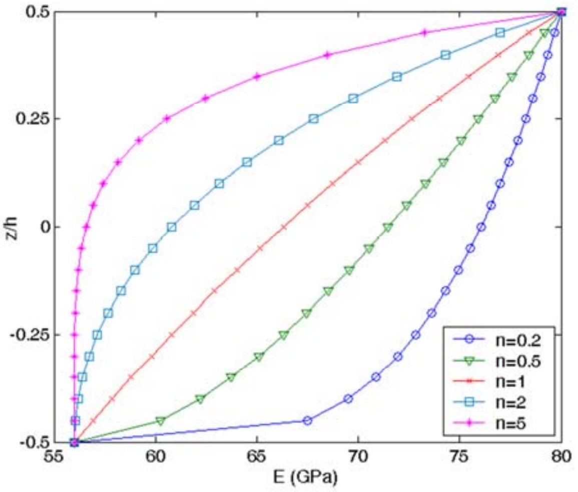

Figure 9.1: Variation of Young's modulus in thickness of FGM beam

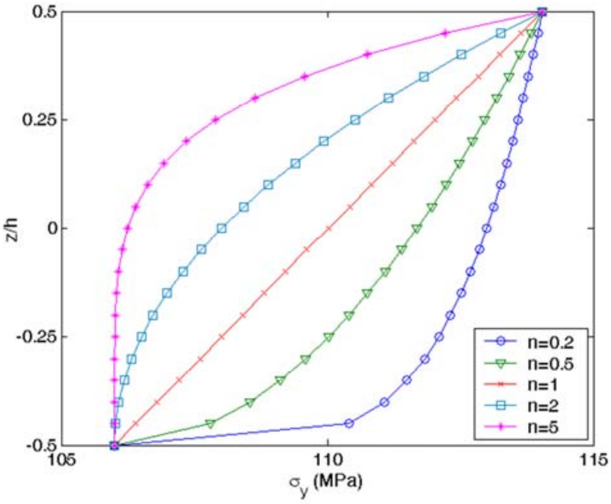

Figure 9.2: Variation of yield stress in thickness of FGM beam

Two kinds of boundary condition, namely clamped–free (*CF*) and simply-supported (*SS*), are considered herein. Ten elements have been used to discretize the beam.

Fig. 9.3 shows the load–displacement curves of the *CF* beam for various values of the volume fraction exponent *n* and an eccentric ratio $ec/r^2 = 0.005$.

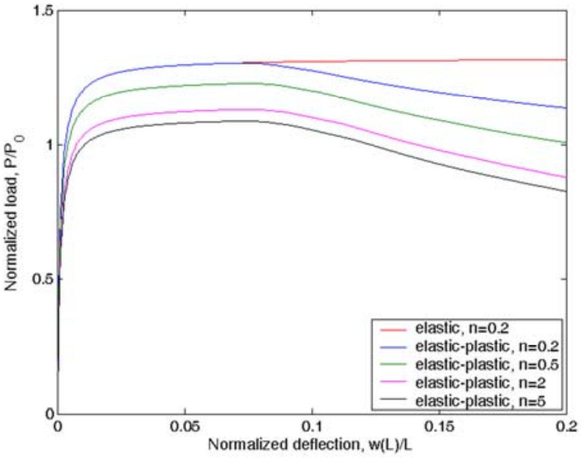

Figure 9.3: Load–displacement curves for *CF* beam with various values of exponent *n* ($ec/r^2 = 0.005$)

In the figure, the deflection *w* is computed at the free end, and the applied load was normalized by the Euler buckling load of the homogeneous metal cantilever beam, that is, $P_0 = \pi^2 E_m I/4L^2$. The eccentric ratio, ec/r^2 (where *r* is the radius of gyration) is defined according to [41], but *c* is now measured from the top surface to the neutral surface, and thus $c = h/2 - h_0$. As seen from the figure, similar to the homogeneous beam [88], the post-buckling of the beam is greatly affected by the plastic deformation, and post-buckling of the beam becomes unstable when the effect of plastic deformation is taken into consideration. The volume fraction exponent *n* alters the limit load of the beam, but it hardly affects the post-buckling behaviour of the beam. It should be noted that the elastic curve in the figure was obtained by setting the yield stress σ_Y in the computer code to a large value so that yielding will not occur. The effect of the eccentric ratio on the post-buckling behaviour of the *CF* beam is depicted in Fig. 9.4 for a value of a volume fraction exponent *n*=3.

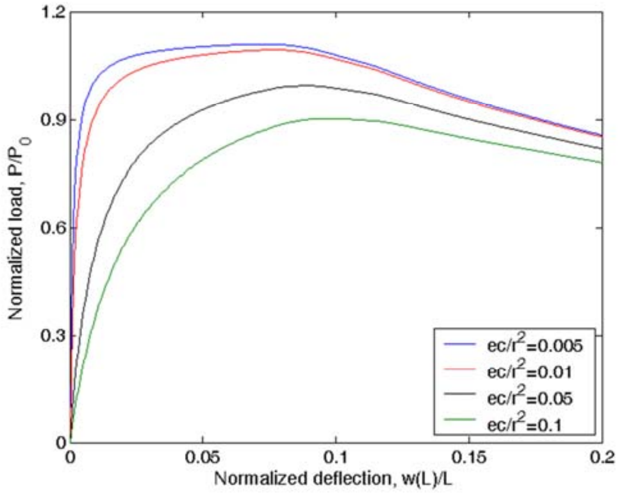

Figure 9.4: Effect of eccentric ratio on the post-buckling behaviour of *CF* beam ($n = 3$)

As seen from the figure, the post-buckling behaviour of the beam is very sensitive to the eccentric ratio, and the limit load gradually reduces when increasing the eccentric ratio. This phenomenon is similar to the post-buckling behaviour of the homogeneous elastic–plastic beams subjected to an axial load [88]. In Fig. 9.5, the load–displacement curves of the *SS* beam are illustrated for various values of the volume fraction exponent n and an eccentric ratio $ec/r^2 = 0.005$.

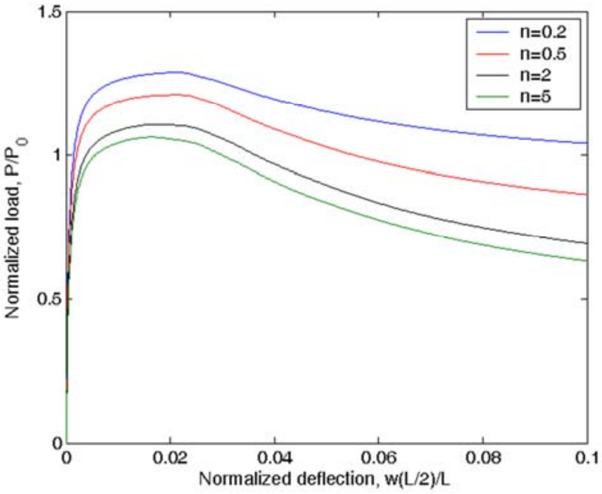

Figure 9.5: Load–displacement curves for *SS* beam with various values of exponent n ($ec/r^2 = 0.005$)

In the figure, P_0 is the buckling load of the simply supported metal beam, i.e., $P_0 = \pi^2 E_m I/L^2$. As in the case of the *CF* beam, the volume fraction exponent changes the limit load of the beam, and the limit load reduces when the volume fraction exponent n increases. In addition, the post-buckling strength of the beam in the post-buckling region, measured in terms of the ratio of applied load to the critical load P_0 of the metal beam, reduces, regardless of the exponent n. This means that the post-buckling of the beam is unstable.

The effect of the eccentric ratio to the post-buckling behaviour of the SS beam as depicted in Fig. 9.6 is similar to the *CF* beam, and the limit load considerably reduces with increase of the eccentric ratio.

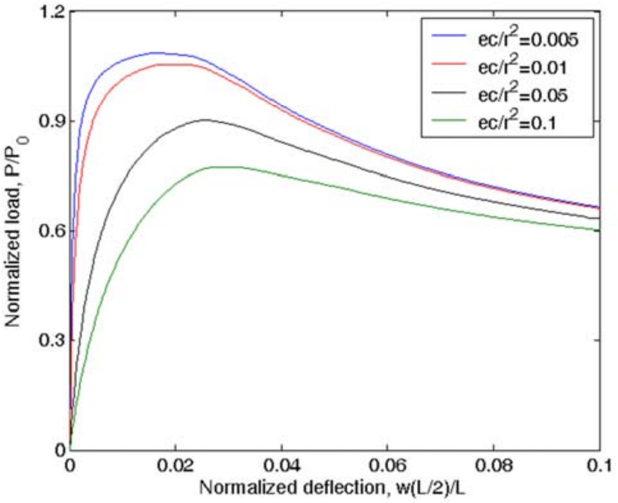

Figure 9.6: Effect of eccentric ratio on the post-buckling behaviour of *SS* beam ($n = 3$)

9.1.3 Conclusions

The following conclusions can be obtained from the sub-section:

- Numerical examples were demonstrated for beams with clamped–free and simply-supported end conditions during the investigation of the post-buckling behaviour of elastic–plastic FGM beams subjected to eccentric axial load.
- The results show that the plastic deformation greatly affects the post-buckling behaviour of the FGM beams, in which the post-buckling of the beam is unstable when the effect of plastic deformation is taken into consideration.
- The post-buckling behaviour is also considerably affected by the volume fraction distribution as well as the eccentric ratio. The volume fraction exponent n alters the limit load of the beam but hardly affects the post-buckling behavior, while the post-buckling behaviour is very sensitive to the eccentric ratio. The limit load gradually reduces as the eccentric ratio increases.

9.2 Elastic–plastic FGM beam on non-linear elastic foundation

9.2.1 Introduction

Analysis of beams resting on an elastic foundation is an important topic in the field of structural mechanics, and it has attracted much attention from many researchers for a long time.

A large number of studies of beams on elastic foundations are referred to in the excellent monograph by [46]. Nearly four decades later, Zhaohua and Cook [141] studied the bending problem of beams on a two-parameter elastic foundation by using the exact interpolation in the derivation of the stiffness matrix. In 1991, Razaqpur and Shah [104] derived the exact stiffness matrix and nodal force vector for assessing the deflection and internal forces of beams resting on a two-parameter elastic foundation. Later, Budkowska and Szymczak [14] used a simple finite element model in studying the post-buckling behaviour of beams partially embedded in a Winkler foundation. In 2006, Kounadis [70] have shown that the post-buckling behaviour of elastic beams resting on a Winkler foundation is stable. The equilibrium paths, computed by Patel [98] and Nguyen [85] by using the finite element method, have also confirmed the stable behaviour in the post-buckling region of axially loaded beams resting on a two-parameter elastic foundation. However, due to the increase of the critical load by the elastic foundation support, the stress in beams on an elastic foundation may exceed the yield stress when the deflection is still very small, even before buckling. Thus, the effect of plastic deformation is an important factor for the buckling behaviour of beams resting on an elastic foundation. In this line of work, based on Hill's variational principle, Cheb and Neal [18] developed a finite element procedure for investigating the buckling and post-buckling behaviour of elastic-plastic beams resting on a non-linear elastic foundation. They then showed that the post-buckling behaviour of the elastic–plastic beams on the foundation is unstable, and the maximum load that the beams can withstand is sensitive to the imperfection and the foundation stiffness. Also using a finite element procedure, recently, Nguyen and his co-workers [93] confirmed that the post-buckling behaviour of beams on an elastic foundation subjected to an eccentric axial load is unstable, and the post-buckling strength, measured in terms of the ratio between the axial load and the critical load, increases with an increment in the foundation stiffness.

9.2.2 Formulation

The elastic–plastic FGM beam shown in Fig. 9.7 which is described in sub-section 2.2.4 is again adopted in this section.

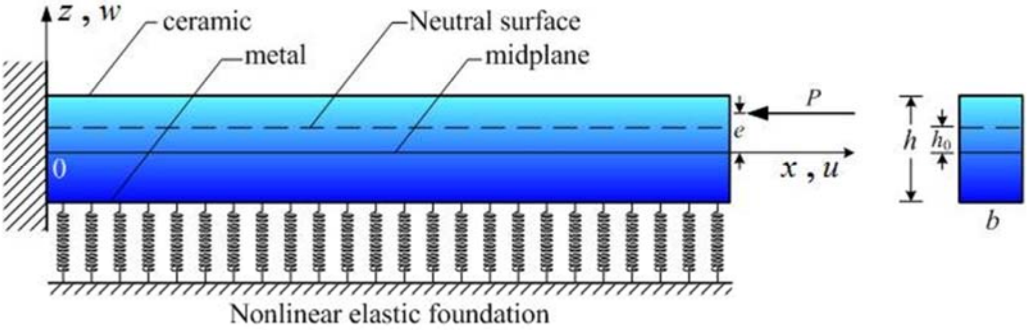

Figure 9.7: Cantilever FGM beam on non-linear elastic foundation under eccentric axial load

To this end, we have to determine the value of q in Eq. (2.43). Various values of q for FGMs formed from different ceramics and metals are given in the papers by Gunes [42] and Huang [52]. In this section, SiC and aluminum (Al) are employed as the ceramic and metal phases of the FGM beam. The Young's moduli of the SiC and Al are 302 GPa and 67 GPa respectively; and the yield stress of Al is 24 MPa. This Al/SiC FGM has $q = 91.6$ GPa, which has been experimentally determined by Bhattacharyya [9]. Figs. 9.9 and 9.10 show the variation of the Young's modulus and the yield stress in the beam thickness direction of the Al/SiC FGM beam according to Eq. (2.44).

The elastic foundation is assumed to be a non-linear model with its reaction force as given by Rajasekhara and Venkateswara [103]:

$$r(x) = k_L w + k_{NL} w^3 \tag{9.1}$$

where w is the transverse displacement of the beam; k_L and k_{NL} are the linear and non-linear foundation stiffness, respectively. The element formulation, namely the internal nodal force vector $\mathbf{f}_{in}$ and the tangent stiffness matrix $\mathbf{k}_t$, can be derived from the expression of the internal virtual work.

For a beam element with length l, the internal virtual work is a contribution from the beam bending and the foundation deformation as

$$\delta W_{in} = \int_V \sigma \delta \varepsilon_v dV + \int_0^l r(x) \delta w_v dx \tag{9.2}$$

where the subscript v stands for *virtual*; V is the element volume; δE_{xv} is the small virtual axial strain, and δw_v is the virtual transverse displacement.

Linear and cubic polynomials can be adopted to interpolate the axial and transverse displacements as

$$u = \mathbf{N}_u^T \mathbf{u}, \; w = \mathbf{N}_w^T \mathbf{w} \tag{9.3}$$

with

$$\begin{aligned} \mathbf{N}_u^T &= \frac{1}{2}\left\{ (1-\xi) \quad (1+\xi) \right\} \\ \mathbf{N}_w^T &= \left\{ \frac{1}{4}\left(2-3\xi+\xi^3\right) \quad \frac{1}{8} l\left(\xi^2-1\right)\left(\xi-1\right) \right. \\ &\qquad \left. \frac{1}{4}\left(2+3\xi-\xi^3\right) \quad \frac{1}{8} l\left(\xi^2-1\right)\left(\xi+1\right) \right\} \end{aligned} \tag{9.4}$$

where $\xi = 2x/l - 1$ is the dimensionless parameter, and with $0 \leq x \leq l$ then $-1 \leq \xi \leq 1$.

9.2.3 Numerical results

An FGM beam composed of SiC and Al with $L = 5$ m; $b = 0.2$ m; and $h = 0.1$ m is employed in the numerical investigation in this computation.

Different values of tangent modulus for Al are available in the literature, and the computations reported below are carried out with $E_0 = 0.2\, E_m$.

Gauss quadrature with nine points in the beam thickness and five points along the element length is employed in computing the element nodal force vector and tangent stiffness matrix. The beam is discretized by ten uniform elements. Two kinds of boundary conditions, namely clamped–free (CF) and simply-supported (SS) are considered.

In order to facilitate the numerical discussion, the following dimensionless parameters, which will be called the linear and non-linear foundation parameters below respectively, are introduced

$$k_1 = {k_L L^4} / {E_m I}$$
$$r^2 = I / A \tag{9.5}$$
$$k_3 = {k_{NL} L^6} / {E_m I}$$

The eccentric ratio $r_C = ec/r^2$ where $c = h/2 - h_0$ and r is the radius of gyration was introduced by Gere and Timoshenko [41] and is adopted herein.

9.2.3.1 Formulation verification

In the case of homogeneous beams resting on a linear elastic foundation, the finite element formulation applied in this section can be deduced exactly to the one previously derived by Nguyen and his co-workers [88].

Since there is no data on the elastic–plastic response of FGM beams, the validation of the formulations is confirmed by comparing the response of an elastic FGM beam to an eccentric axial load.

Fig. 9.8 shows the load–displacement curves for the Al/SiC cantilever beam under an eccentric tip load with $e=h/2-h_0$ obtained by the present element, where for the sake of comparison, the result obtained by using the co-rotational element derived in [92], [93] is also shown by the dashed lines.

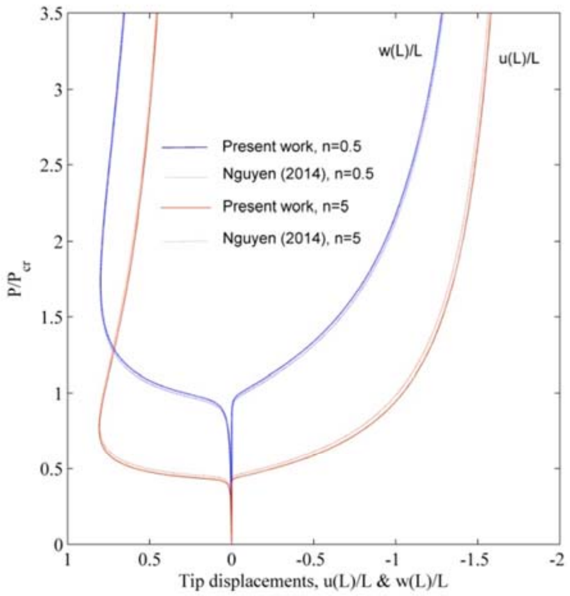

Figure 9.8: Load–displacement curves for elastic FGM cantilever beam under an axial load

In the figure, the tip axial and transverse displacements, u and w, respectively are normalized by the beam length L, and the applied load is normalized by the Euler load of the cantilever full metal beam, i.e. $P_{cr} = \pi^2 E_m I/4L^2$. For the elastic analysis herein, the yield stress of the metal phase is set to a large value, and thus the yielding will not occur. Regardless of the exponent n, a good agreement is noted from the figure.

It should be noted that the effective Young's modulus in this work by Nguyen [93] was evaluated by using the Voigt model, which is slightly different from the one computed by Eq. (2.44).

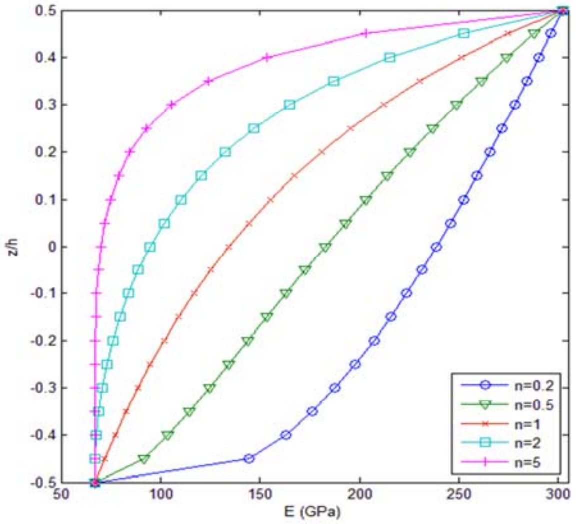

Figure 9.9: Variation of Young's modulus in thickness of FGM beam

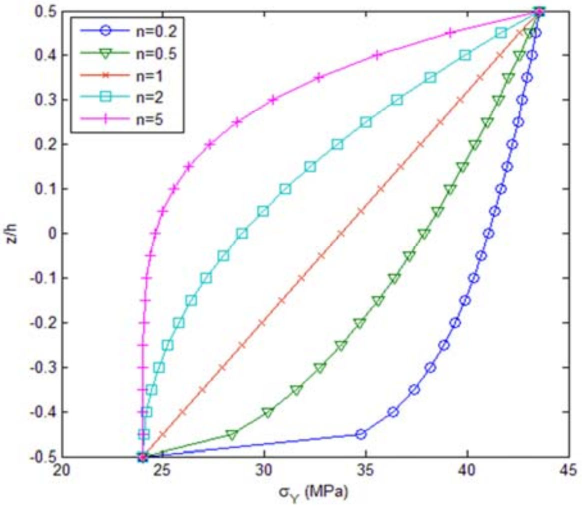

Figure 9.10: Variation of yield stress in thickness of FGM beam

9.2.3.2 Cantilever beam

In Fig. 9.11, the load–displacement curves representing the equilibrium paths of the *CF* beam without the foundation support obtained by the elastic and elastic–plastic analyses are depicted for $r_C = 0.01$, and for two values of the fraction exponent n = 0.5 and n =5.

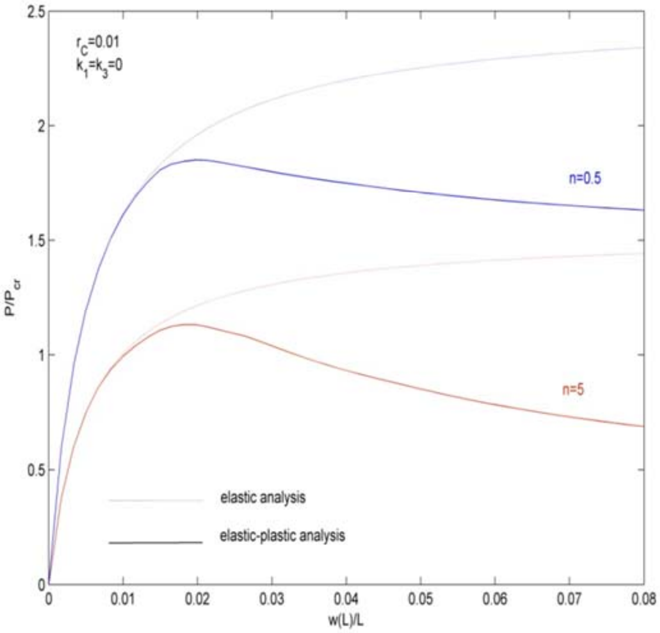

Figure 9.11: Load–displacement curves of *CF* beam obtained by elastic and elastic–plastic analyses

In the figure, P_{cr} is the Euler buckling load of the Al beam.

The effect of plastic deformation is clearly seen from the figure, where the post-buckling of the FGM beam changes from stable to unstable when the effect of plastic deformation is taken into account.

The effect of the material distribution is also clearly seen from the figure, where the post-buckling strength of the beam, measured in terms of the ratio between the applied load P and the critical load P_{cr}, is higher for the beam associated with the lower exponent n.

In other words, the post-buckling strength of the elastic–plastic FGM beam is higher for the beam associated with a higher ceramic content.

The effect of the linear and non-linear foundation parameters is illustrated in Figs. 9.12 and 9.13 for an eccentric ratio $r_C = 0.01$ and an exponent $n = 5$, respectively.

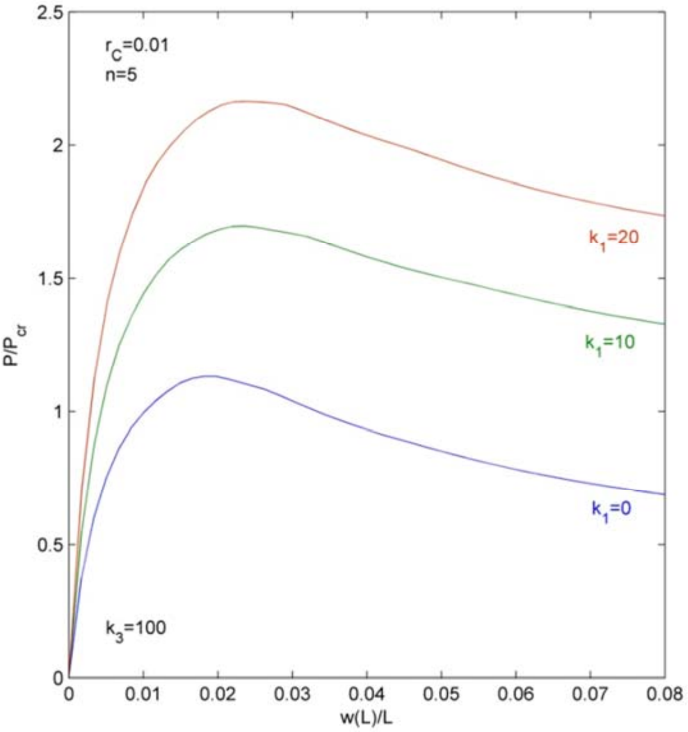

Figure 9.12: Effect of linear foundation parameter on elastic–plastic response of *CF* beam

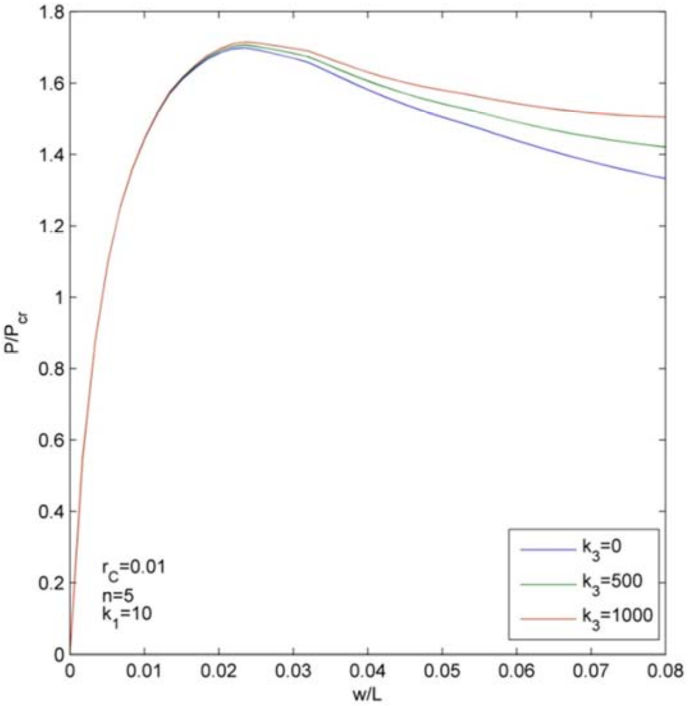

Figure 9.13: Effect of non-linear foundation parameter on elastic–plastic response of *CF* beam

The limit yield point of the beam, as seen from Fig. 9.12, increases considerably by increasing the linear foundation stiffness, but the post-buckling strength of the beam is hardly recognized. On the other hand, the non-linear foundation parameter as seen in Fig. 9.13 , contributed to an increase in the post-buckling strength, but it hardly alters the limit load of the beam.

As seen in Fig. 9.11, the post-buckling strength of the beam on the elastic foundation is higher for the beam associated with a lower exponent *n*.

The post-buckling strength of the beam is, however, slightly improved by the foundation support.

To investigate the effect of plastic deformation on the behaviour of the beam in more detail, the stresses and strains at lower and upper Gauss points near the clamped end at various values of the applied load are given in Table 9.1.

Table 9.1: Axial stress, strain at lower, upper Gauss points corresponding to points P_i,P'_i (i = 1..3) in Fig. 9.14

	n	**Loading stages**	***P/Pcr***	σ_M (10^7)	σ_C (10^7)	ε_M (10^{-4})	ε_C (10^{-4})
$k_1 = 20$ $k_3 = 10$	**0.5**			2.7125	4.3340		
		P'_1	2.4674	0.9244	-5.8667	1.1045	-2.0036
		P'_2	2.9887	2.8862	-12.607	4.0498	-4.3466
		P'_3	2.9877	2.9428	-13.080	4.3135	-4.5111
	5			2.4000	4.1220		
		P_1	2.1460	0.9764	-7.4189	1.4574	-3.3631
		P_2	2.1480	1.0499	-7.6266	1.5670	-3.4677
		P_3	2.1467	1.1144	-7.8056	1.6632	-3.5580

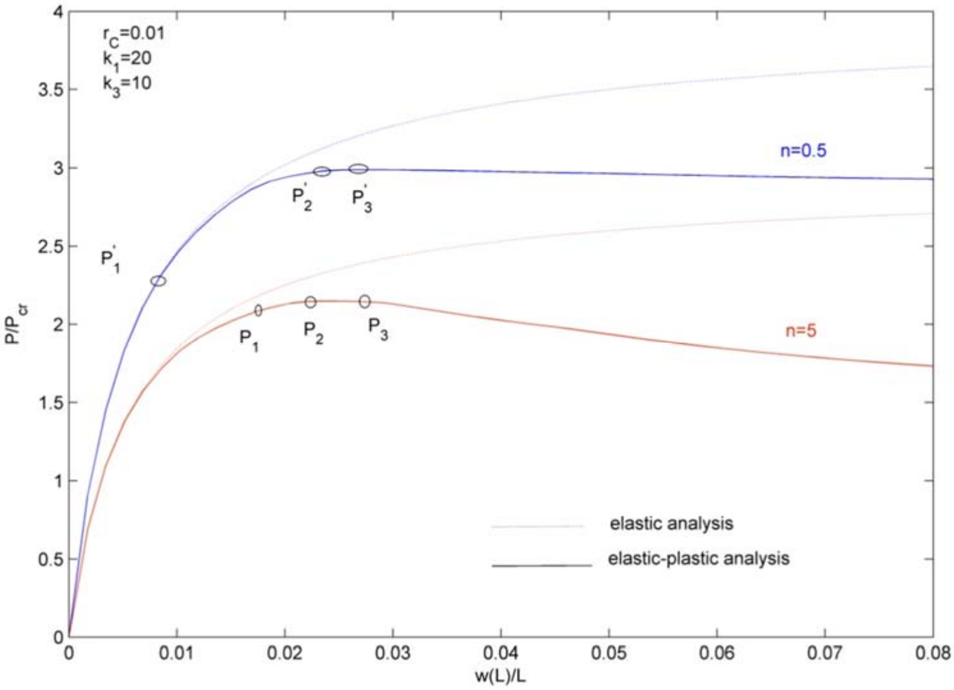

Figure 9.14: Load–displacement curves for CF beam resting on non-linear elastic foundation obtained by elastic and elastic–plastic analyses

The *z* co-ordinates of the lower and upper points are respectively -0.0484 m and 0.0484 m for the Gauss quadrature used herein (five points along the element length and nine points through the thickness). The *x* co-ordinate is 0.0235 *m* for both points. Since these points are near the metal and ceramic surfaces, for the sake of convenience, the subscripts *M* and *C* are used to denote the stress and strain at the points.

These stresses highlighted in red correspond to the applied loading stages where yielding at the points has already occurred.

As seen in Table 9.1, the yielding that occurs in the FGM beam is very different from that of the homogeneous beams where the top and bottom fibres yield symmetrically about the neutral axis at the mid-height of the cross-section.

In the FGM beam, at a given value of the applied load, the stress amplitude near the ceramic surface is considerably higher than that near the metal surface, while the strain is on the opposite side.

The stresses at the applied loading stages P_1', P_1, P_2 and P_3 in Table 9.1 show that yielding has occurred in the layer near the ceramic surface, but it has not occurred in a layer near the metal surface.

This result is totally different from the homogeneous beam, where the yielding occurs in the lower and upper surfaces at the same time.

The effect of the eccentric ratio on the elastic–plastic response of the *CF* beam is illustrated in Fig. 9.15 for an exponent value n=3 and for k_1 =20, k_3 =10.

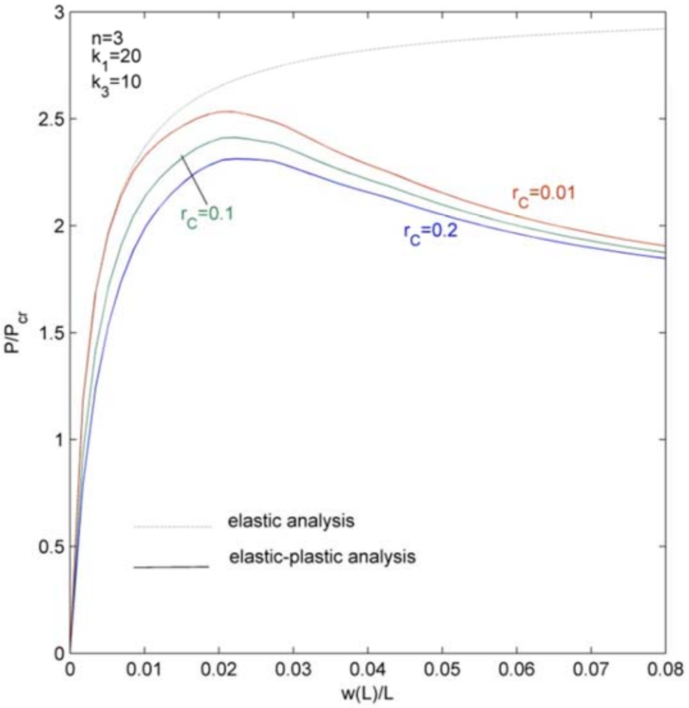

Figure 9.15: Effect of eccentric ratio on elastic–plastic response of *CF* beam on non-linear elastic foundation

The effect of the eccentric ratio on the elastic–plastic behaviour in the post-buckling region of the *CF* beam is similar to that of the homogeneous beams reported by Nguyen in [88], in which the limit load of the beam steadily reduced by increasing the eccentric ratio.

9.2.3.3 Simply-supported beam

In Fig. 9.16, the load–displacement curves of an unsupported SS beam obtained by elastic and elastic–plastic analyses are depicted for $r_C = 0.01$ and two values of the exponents $n = 0.5$ and $n = 5$.

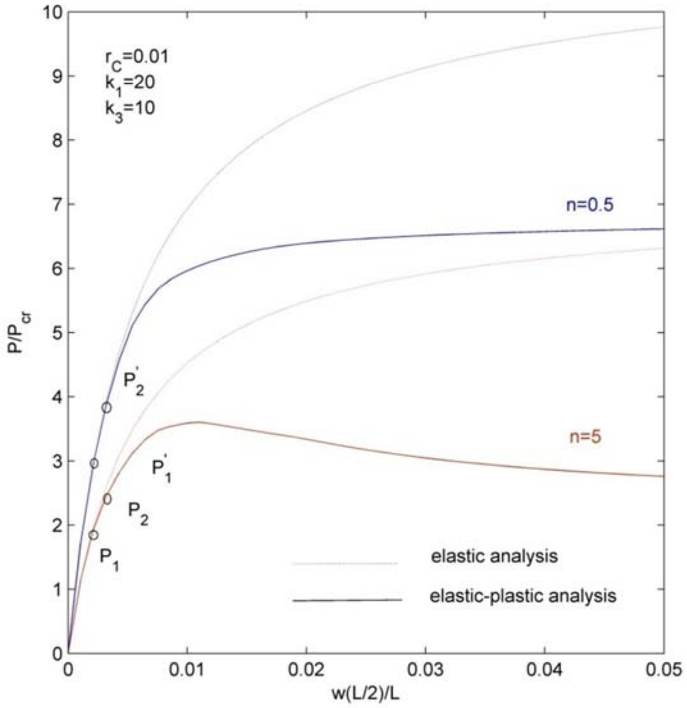

Figure 9.16: Load–displacement curves of SS beam obtained by elastic and elastic–plastic analyses

The effect of the foundation parameters and the eccentric ratio for the SS beam is shown in Figs. 9.17–9.20.

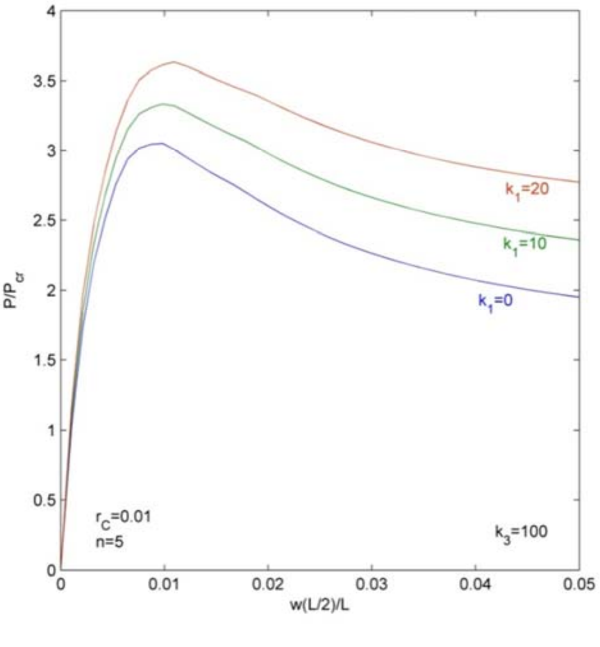

Figure 9.17: Effect of linear foundation parameter on elastic–plastic response of SS beam

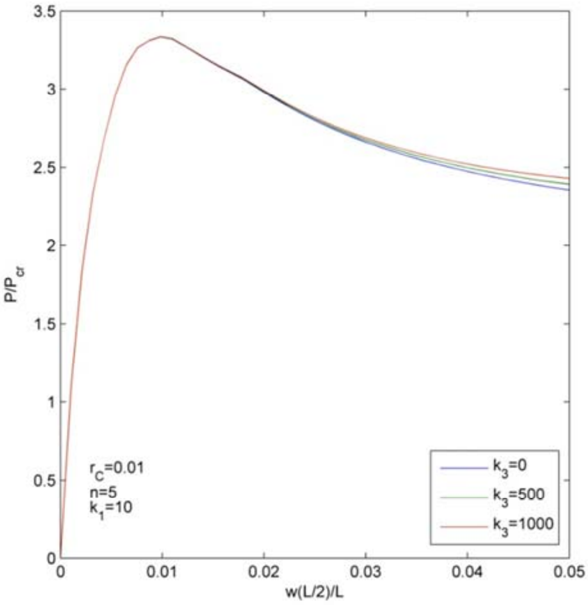

Figure 9.18: Effect of non-linear foundation parameter on elastic–plastic response of SS beam

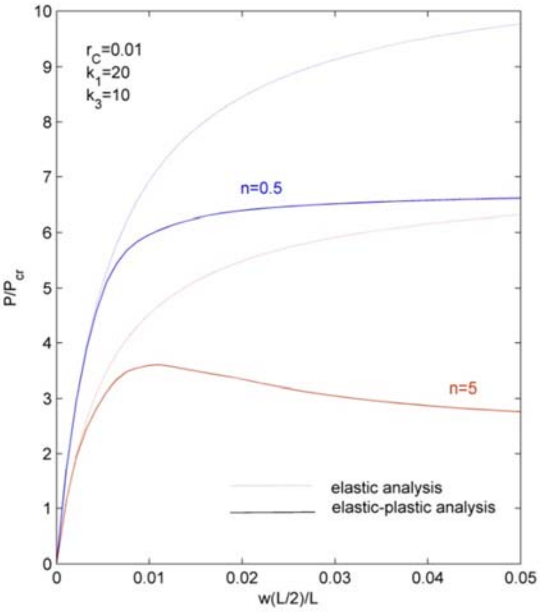

Figure 9.18: Load–displacement curves for SS beam resting on non-linear elastic foundation obtained by elastic and elastic–plastic analyses

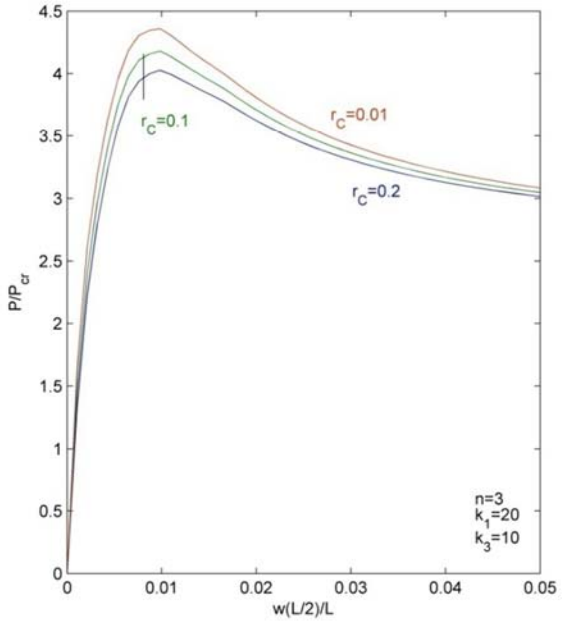

Figure 9.20: Effect of eccentric ratio on elastic–plastic response of SS beam on non-linear elastic foundation

The effects of the plastic deformation, material distribution, linear foundation parameter, non-linear foundation parameter, and eccentric ratio on the elastic–plastic response of the SS beam are similar to those of the CF beam. However, compared to the CF beam, the SS beam is less sensitive to the change in the foundation stiffness and the eccentric ratio.

9.2.4 Conclusions

The following conclusions can be drawn:

- For different fraction exponents, the elastic–plastic analyses curves show a steady reduction of responses beyond the limit load compared to the elastic analyses results.
- The limit point of a beam increases considerably when raising the linear foundation stiffness, but the post-buckling strength of the beam is hardly recognized in the non-linear elastic foundation.
- The post-buckling strength of the beam is, however, slightly improved by the type of foundation support (non-linear elastic foundation).
- The effect of the eccentric ratio on the elastic–plastic behaviour in the post-buckling region of the beams is similar to that of the homogeneous beams.
- The yielding that occurred in the FGM beam is very different from the homogeneous beam.
- The plastic deformation, material distribution, foundation parameters and eccentric ratio have great influences on the elastic–plastic response of the FGM beams.

Chapter 10: Concluding remarks and future directions

10.1 Concluding remarks

- This work shows a new way to build consistent shape functions and exact shape functions. The accuracy of these derived functions is verified through a series of numerical examples of static and free vibration analyses. Significant accuracies with least element division were observed.
- The Newmark method was applied in dynamic analysis while a co-rotational approach and arc-length control method were used in buckling problems.
- The dynamic response of the multi-span FGM beam under a moving harmonic load has been proved to be under the influence of the material heterogeneity, the number of spans, and loading parameters.
- The material non-homogeneity, section profiles, aspect ratio, number of loads, and distance between loads have been proved to greatly affect the dynamic characteristics of a non-prismatic FGM beam subjected to multiple moving loads.
- The effect of the material distribution on the post-buckling response of the axially FGM structures was highlighted through this work.
- The dynamic behaviour of FGM beams in a thermal environment due to a moving harmonic load was investigated.
- The influences of material distribution, foundation support, and eccentric ratio on the elastic–plastic response of FGM beams on a non-linear foundation were also investigated carefully in this work.

10.2 Future directions

Research into the behaviour of functionally graded concrete (FGC) has been conducted and was inspired by the study of the actual compression strength gradation of deep beams. It was concluded that whereas the members were designed to have homogeneous characteristics throughout their entire depth, in reality a member exhibited a gradation in the compression ultimate strength and stiffness. The phenomenon of natural gradation in concrete members was earlier detected by researchers. Recently, a study of the behaviour of the stress distribution within a cantilever FGC beam was conducted numerically. It was shown that the shear-stress distribution followed a parabolic path along the depth of the member. It was also demonstrated that the layer displacement increased linearly, approaching the bottom layers of the beam. The FGC thus has potential to be utilized for optimization purposes.

An experimental study to produce a concrete strength gradation in a laboratory environment was developed. The procedure was conducted by mechanical compacting of fresh concrete layers with differentiations designed in the cylindrical compression strength. The strength and stiffness of the graded specimens were compared to the homogeneous specimens, and the parameters measured were the 28 days compression strength, the Young's modulus E, the Poisson's ratio ν, and the stress–strain behaviour of the specimens as a function of incremental loading. These controlling specimens showed a uniform behaviour throughout their entire depth. All specimens were tested in uniaxial compression.

Further, a numerical model to study the behaviour of these FGC cylinders was developed. The finite element model (FEM) was based on the layer-wise homogenized approach, and the load–displacement responses as predicted by the FEM were confirmed by the laboratory data. The FEM model was used to analyze the response of FGC members in bending. This dissertation looked into the potential advantages of producing an FGC member as part of a structure, and explores the impact of such a member on the overall performance of a two-storey building subjected to vertical and horizontal loads. The prospects of material optimization are looked into, and the capacities of the graded members are compared to the uniform concrete structure.

Bibliography

[1] Alshorbagy, A.E., Eltaher, M.A. and Mahmoud, F.F.: Free vibration characteristics of a functionally graded beam by finite element method, Applied Mathematical Modeling, 35(1), 412-425, 2011

[2] Andrade, A. and Camotim, D.: Lateral-torsional buckling of singly symmetric tapered beams: Theory and applications, Journal of Engineering Mechanics (ASCE), 131(6), 586-597, 2005

[3] Archer, J.S.: Consistent matrix formulations for structural analysis using finite element techniques, AIAA Journal, 3, 1910-1918, 1965

[4] Aristizabal, Ochoa, J.D.: Statics, stability and vibration of non-prismatic beams and columns, Journal of Sound Vibration, 162(3), 441-455, 1993

[5] Attarnejad, R., Semnani, S.J. and Shahba, A.: Basic displacement functions for free vibration analysis of non-prismatic Timoshenko beams, Finite Elements in Analysis and Design, 46, 916-929, 2010

[6] Banerjee, J.R.: Compact computation of buckling loads for plane frames consisting of tapered members, Computational Mechanics Publications, 9(3), 162-170, 1987

[7] Bazeos, N. and Karabalis, D.L.: Efficient computation of buckling loads for plane steel frames with tapered members, Engineering Structures, 28, 771-775, 2006

[8] Belytschko, T., Liu, W.K. and Moran, B.: Nonlinear finite elements for continua and structures, 1st ed., John Wiley & Sons, Chichester, 2000

[9] Bhattacharyya, M., Kapuria, S. and Kumar A.N.: On the stress to strain transfer ratio and elastic deflection behavior for Al/SiC functionally graded material, Mechanics of Advanced Materials and Structures, 14, 295-302, 2007

[10] Birman, V. and Byrd, L.W.: Modeling and analysis of functionally graded materials and structures, Applied Mechanics Reviews, 60(5), 195-216, 2007

[11] Bradford, M.A.: Stability of tapered I-beams, Journal of Constructional Steel Research, 9(3), 195-216, 1988

[12] Bradford, M.A.: Lateral behaviour of tapered steel members, In: Shanmugam, N.E., Wang, C.M., editors, Analysis and design of plated structures, Vol. 1. Stability, Woodhead Publishing Ltd., Cambridge, 1-25, 2006

[13] Bradford, M.A.: Dynamic behaviour of tapered beams. In: Shanmugam, N.E., Wang, C.M., editors, Analysis and design of plated structures, Vol. 2, Dynamics, Woodhead Publishing Ltd., Cambridge, 1-35, 2006

[14] Budkowska, B.B. and Szymczak, C.: Initial post-buckling behavior of piles partially embedded in soil, Computers & Structures, 62(5), 831-835, 1997

[15] Carnegie, W., Thomas, J. and Dokumuci, E.: An improved method of matrix displacement analysis in vibration problems, Aeronautical Quarterly, 20, 321-332, 1969

[16] Chaht, F.L., Kaci, A., Houari, M.S.A., Tounsi, A., Bóg, O.A. and Mahmoud, S.R.: Bending and buckling analyses of functionally graded material (FGM) size-dependent nanoscale beams including the thickness stretching effect, Steel & Composite Structures, 18(2), 425-442, 2015

[17] Chakraborty, A., Gopalakrishnan, S. and Reddy, J.N.: A new beam finite element for the analysis of functionally graded materials, International Journal of Mechanical Sciences, 45(3), 519-539, 2003

[18] Chebl, C. and Neal, K.W.: A finite element method for elastic–plastic beams and columns at large deflections, Computers & Structures, 18(2), 255-261, 1984

[19] Chegenizadeh, A., Ghadimi, B., Nikraz, H. and Şimşek, M.: A novel two–dimensional approach to modeling functionally graded beams resting on a soil medium, Structural Engineering & Mechanics, 51(5), 727-741, 2014

[20] Cleghorn, W.L. and Tabarrok, B.: Finite element formulation of a tapered Timoshenko beam for free lateral vibration analysis, J. Sound and Vibration, 152(3), 461-470, 1992

[21] Cook, R.D., Malkus, D.S. and Plesha, M.E.: Concepts and applications of finite element analysis, John Wiley & Sons, New York, 1989

[22] Crisfield, M.A.: Non-linear finite element analysis of solids and structures, Vol. 1: Essentials, John Wiley & Sons, Chichester, 2010

[23] Davis, R., Henshell, R.D. and Warburton, G.B.: A Timoshenko beam finite element, Journal of Sound and Vibration, 22, 475-487, 1972

[24] Dong, S.B. and Wolf, S.B.: Effect of transverse shear deformation on vibrations of planar structures composed of beam–type elements, Journal of the Acoustical Society of America, 53, 120-127, 1973

[25] Ebrahimi, F., Ghasemi, F. and Salari, E.: Investigating thermal effects on vibration behavior of temperature-dependent compositionally graded Euler beams with porosities, Meccanica, DOI 10.1007/s11012-015-0208-y.

[26] Egle, D.M.: An approximate theory for transverse shear deformation and rotatory inertia effects in vibrating beams, NASA CR–1317, 1969

[27] Eisenberger, M.: Explicit stiffness matrices for non-prismatic members, Computers & Structures, 20(4), 715-720, 1985

[28] Eisenberger, M. and Reich, Y.: Buckling of variable cross-section columns, Steel Structures, Proceedings of Structures Congress, 89 San Francisco, CA, USA, 443-451, 1989

[29] Eisenberger, M.: Stiffness matrices for non-prismatic members including transverse shear, Computers & Structures, 40(4), 831-835, 1991

[30] Eltaher, M.A., Alshorbagy, A.E. and Mahmoud, F.F.: Determination of neutral axis position and its effect on natural frequency of functionally graded macro/nanobeams, Composite Structures, 99, 193-201, 2013

[31] Fallah, A. and Aghdam, M.M.: Nonlinear free vibration and post-buckling analysis of functionally graded beams on nonlinear elastic foundation, European Journal of Mechanics-A/Solids, 30(4), 571-583, 2011

[32] Franciosi, C. and Mecca M.: Some finite elements for the static analysis of beams with varying cross section, Computers & Structures, 69, 191-196, 1998

[33] Erasmo, C., Gaetano, G. and Marco, P.: Beam Structures: Classical and Advanced Theories, John Wiley & Sons, 2011

[34] Friedman, Z. and Kosmatka, J.B.: Exact stiffness matrix of a nonuniform beam–I, extension, torsion, and bending of a Bernoulli–Euler beam, Computers & Structures, 42(5), 671-682, 1992

[35] Friedman, Z. and Kosmatka, J.B.: An improved two-node Timoshenko beam finite element, Computers & Structures, 47(3), 473–481, 1993

[36] Friedman, Z. and Kosmatka, J.B.: Exact stiffness matrix of a nonuniform beam–II, bending of a Timoshenko beam, Computers & Structures, 49(3), 545-555, 1993

[37] Fryba, L.: Vibration of solids and structures under moving loads, Academia, Prague, 1972

[38] Gan, B.S, Trinh, T.H., Le, T.H., Nguyen, D.K.: Dynamic response of non-uniform Timoshenko beams made of axially FGM subjected to multiple moving point loads, Structural Engineering & Mechanics, 53, 981-995, 2015

[39] Garvan, F.: The Maple Book, Chapman & Hall/CRC, Florida, 2002

[40] Geradin, M. and Rixen, R.: Mechanical vibrations, Theory and application to structural dynamics, 2nd ed., John Wiley & Sons, Chichester, 1997

[41] Gere, J.M. and Timoshenko, S.: Mechanics of Materials, 3rd ed., Chapman & Hall, London, 1991

[42] Gunes, R., Aydin, M., Kemak Apalak, M. and Reddy, J.R.: The elastic-plastic impact analysis of functionally graded circular plates under low-velocities, Composite Structures, 93, 860-869, 2011

[43] Gupta, A.K.: Vibration of tapered beams, Journal of Structural Engineering, 111(1), 19-36, 1985

[44] Gutierrez, R.H., Laura, P.A.A. and Rossi, R.E.: Natural frequency of vibration of a Timoshenko beam of non-uniform thickness, Journal of Sound & Vibration, 145(2), 341-344, 1991

[45] Henchi, K., Fafard, M. and Dhatt, G.: Dynamic behavior of multi-span beams under moving loads, Journal of Sound & Vibration, 199(1), 33-50, 1997

[46] Hetenyi, M.: Beams on Elastic Foundation: Theory with Applications in the Fields of Civil and Mechanical Engineering, The University of Michigan Press, Ann Arbor, 1946

[47] Hino, J., Yoshimura, T., Konihi, K. and Ananthanarayana, N.: A finite element method prediction of the vibration of a bridge subjected to a moving vehicle load, Journal of Sound & Vibration, 96(1), 45-53, 1984

[48] Hsiao, K.M. and Huo, F.Y.: Nonlinear finite element analysis of elastic frames, Computers & Structures, 26, 693-704, 1987

[49] Huang, Y. and Li, F.: A new approach for free vibration of axially functionally graded beams with non-uniform cross-section, Journal of Sound & Vibration, 96(1), 45-53, 2010

[50] Huang, Y. and Li, X.F.: Buckling analysis of non-uniform and axially graded beams with varying flexural rigidity, Journal of Engineering Mechanics, 137(1), 73-81, 2011

[51] Huang, H. and Han, Q.: Elastoplastic buckling of axially loaded functionally graded material cylindrical shells, Composite Structures, 117, 135-142, 2014

[52] Huang, H., Chen, B. and Han, Q.: Investigation on buckling behaviors of elastoplastic functionally graded cylindrical shells subjected to torsional loads, Composite Structures, 118, 234-240, 2014

[53] Hughes, T.J.R., Taylor, R.L. and Kanoknukulchai, W.: A simple and efficient plate element for bending, International Journal for Numerical Methods in Engineering, 11, 1529-1543, 1977

[54] Ichikawa, M., Miyakawa, Y. and Matsuda, A.: Vibration analysis of the continuous beam subjected to a moving mass, Journal of Sound & Vibration, 230(3), 611-628, 2000

[55] Jahromi, B.H., Nayeb-Hashemi, H. and Vaziri, A.: Elasto-plastic stresses in a functionally graded rotating disk, Journal of Engineering Materials and Technology, 134(2), 021004-11, 2012

[56] Jha, D.K., Kant, T. and Singh, R.K.: A critical review of recent research on functionally graded plates, Composite Structures, 96, 833-849, 2013

[57] Jin, Z.H., Paulino, G.H. and Dodds, R.H.: Cohesive fracture modeling of elastic–plastic crack growth in functionally graded materials, Engineering Fracture Mechanics, 70, 1885-1912, 2003

[58] Kadoli, R., Akhtar, K. and Ganesan, N.: Static analysis of functionally graded beams using higher order shear deformation beam theory, Applied Mathematical Modeling, 32(12), 2509-2525, 2008

[59] Kang, Y.A. and Li, X.F.: Bending of functionally graded cantilever beam with power-law nonlinearity subjected to an end force, International Journal of Non-Linear Mechanics, 44(6), 696-703, 2009

[60] Kang, Y.A. and Li, X.F.: Large deflection of a non-linear cantilever functionally graded beam, Journal of Reinforced Plastics and Composites, 29(4), 1761-1774, 2010

[61] Kapur, K.K.: Vibrations of a Timoshenko beam using a finite element approach, Journal of the Acoustical Society of America, 40, 1058-1063, 1966

[62] Kar, R.C. and Sujata, T.: Dynamic stability of a tapered symmetric sandwich beam, Computers & Structures, 40(6), 1441-1449, 1991

[63] Karabalis, D.L. and Beskos, D.E.: Static, dynamic and stability analysis of structures composed of tapered beams, Computers & Structures, 16(6), 731-748, 1983

[64] Khalili, S.M.R. and Saboori, B.: Transient dynamic analysis of tapered FRP composite transmission poles using finite element method, Computers & Structures, 92(2), 275-283, 2010

[65] Khalili, S.M.R., Jafari, A.A. and Eftekhari, S.A.: A mixed Ritz-DQ method for forced vibration of functionally graded beams carrying moving loads, Composite Structures, 92, 2497-2511, 2010

[66] Kim, Y.W.: Temperature dependent vibration analysis of functionally graded rectangular plates, Journal of Sound & Vibration, 284, 531-549, 2005

[67] Koizumi, M.: FGM activities in Japan, Composites: part B, 28(1-2), 1-4, 1997

[68] Kocaturk, T. and Akbas, S.D.: Post-buckling analysis of Timoshenko beams made of functionally graded material under thermal loading, Structural Engineering & Mechanics, 41(6), 775-789, 2012

[69] Kosmatka, J.B.: An improved two-node finite element for stability and natural frequencies of axial-loaded Timoshenko beams, Computers & Structures, 57(1), 141-149, 1995

[70] Kounadis, A.N., Mallis, J. and Sbarounis, A.: Post-buckling analysis of columns resting on an elastic foundation, Archive of Applied Mechanics, 75, 395-404, 2006

[71] Lee, S.Y., Ke, H.Y. and Kuo, Y.H.: Analysis of non-uniform beam vibration, Journal of Sound & Vibration, 142(1), 15-29, 1990

[72] Leung, A.Y.T., Zhou, W.E., Lim, C.W., Yuen, R.K.K. and Lee, U.: Dynamic stiffness for piecewise non-uniform Timoshenko column by power series–part I: Conservative axial force, International Journal for Numerical Methods in Engineering, 51, 505-529, 2001

[73] Leung, A.Y.T., Zhou, W.E., Lim, C.W., Yuen, R.K.K. and Lee, U.: Dynamic stiffness for piecewise non-uniform Timoshenko column by power series-part II: Follower force, International Journal for Numerical Methods in Engineering, 51, 505-529, 2001

[73] Levyakov, S.V.: Elastica solution for thermal bending of a functionally graded beam, Acta Mechanica, 224(8), 1731-1740, 2013

[75] Li, X.F.: A unified approach for analyzing static and dynamic behaviors of functionally graded Timoshenko and Euler–Bernoulli beams, Journal of Sound & Vibration, 318(4-5), 1210-1229, 2008

[76] Li, Q.H. and Xu, S.L.: Experimental investigation and analysis on flexural performance of functionally graded composite beam crack–controlled by ultrahigh toughness cementitious composites, Science in China Series E: Technological Science, 52(6), 1648-1664, 2009

[77] Li, S., Hu, J., Zhai, C. and Xie, L.: A unified method for modeling of axially and/or transversally functionally graded beams with variable cross-section profile, Mechanics Based Design of Structures and Machines, 41, 168-188, 2013

[78] Lin, W.H. and Trethewey, M.W.: Finite element analysis of elastic beams subjected to moving dynamic loads, Journal of Sound & Vibration, 136(2), 323-342, 1990

[79] Mahi, A., Adda Bedia, E.A., Tounsi, A. and Mechab, I.: An analytical method for temperature-dependent free vibration analysis of functionally graded beams with general boundary conditions, Composite Structures, 92, 1877-1887, 2010

[80] Mahmoud Bayat, Pakar, I. and Mahdi Bayar: Analytical study on the vibration frequencies of tapered beams, Latin American Journal of Solids and Structures, 8, 149-162, 2011

[81] McCalley, R.B.: Rotary Inertia Correction for Mass matrices, General Electric Knolls Atomic Power Laboratory, Schenectady, NY, Report DIG/SA, 63-73, 1963

[82] Meek, J.L. and Xue, Q.: A study on the instability problems for 2D-frames, Computer Methods in Applied Mechanics and Engineering, 136, 347-361, 1996

[83] Mou, Y., Han, R.P.S. and Shah, A.H.: Exact dynamics stiffness matrix for beams of arbitrarily varying cross sections, International Journal for Numerical Methods in Engineering, 40, 233-250, 1997

[84] Nazari, A. and Sanjayan, J.G.: Compressive strength of functionally graded geopolymers: Role of position of layers, Construction & Building Materials, 75(30), 31-34, 2015

[85] Nguyen, D.K.: Post-buckling behavior of beam on two-parameter elastic foundation, International Journal of Structural Stability and Dynamics, 4(1), 21-43, 2004

[86] Nguyen, D.K.: Dynamic response of prestressed Timoshenko beams resting on two-parameter foundation to a moving load, Technische Mechanik, 28(3-4), 237-258, 2008

[87] Nguyen, D.K. and Le, T.H.: Dynamic characteristics of elastically supported beam subjected to a compressive axial force and a moving load, Vietnam Journal of Mechanics, 33(2), 113-131, 2011

[88] Nguyen, D.K., Trinh, T.H. and Gan, B.S.: Post-buckling response of elastic–plastic beam resting on an elastic foundation to eccentric axial load, The IES Journal Part A: Civil & Structural Engineering, 5, 43-49, 2012

[89] Nguyen, D.K.: A Timoshenko beam element for large displacement analysis of planar beams and frames, International Journal of Structural Stability and Dynamics, 12(6), 1-9, 2012

[90] Nguyen, D.K.: Large displacement response of tapered cantilever beams made of axially functionally graded material, Composites Part B: Engineering, 55, 298-305, 2013

[91] Nguyen, D.K., Gan, B.S. and Le, T.H.: Dynamic response of non-uniform functionally graded beams subjected to a variable speed moving load, Journal of Computational Material Science and Technology, 7(1), 12-27, 2013

[92] Nguyen, D.K. and Gan, B.S.: Large displacements of tapered functionally graded beams subjected to end loads, Applied Mathematical Modelling, 38, 3054-3066, 2014

[93] Nguyen, D.K., Gan, B.S. and Trinh, T.H.: Geometrically nonlinear analysis of planar beam and frame structures made of functionally graded material, Structural Engineering & Mechanics, 49(6), 727-743, 2014

[94] Nickell, R.E. and Secor, G.A.: Convergence of consistently derived Timoshenko beam finite elements, International Journal for Numerical Methods in Engineering, 5, 243-253, 1972

[95] Olsson, M.: On the fundamental moving load problem, Journal of Sound and Vibration, 145(2), 299-307, 1991

[96] Ozgumus, O.O. and Kaya, M.O.: Flapwise bending vibration analysis of a rotating double-tapered Timoshenko beam, Archive of Applied Mechanics, 78, 379-392, 2008

[97] Pacoste, C. and Eriksson, A.: Beam elements in instability problems, Computer Methods in Applied Mechanics and Engineering, 144, 163-197, 1997

[98] Patel, B.P., Ganapathi, M. and Touratier, M.: Nonlinear free flexural vibrations/post-buckling analysis of laminated orthotropic beams/columns on a two parameter elastic foundation, Composite Structures, 46(2), 189-196, 1999

[99] Pradhan, S.C. and Murmu, T.: Thermo-mechanical vibration of FGM sandwich beam under variable elastic foundations using differential quadrature method, Journal of Sound & Vibration, 321, 342-362, 2009

[100] Przemieneicki, J.S.: Theory of Matrix Structural Analysis, 70-82, McGraw-Hill, New York, 1968

[101] Raftoyiannis, I.G. and Polyzois, D.J.: The effect of semi-rigid connections on the dynamic behavior of tapered composite GFRP poles, Computers & Structures, 81(1), 70-79, 2007

[102] Rajabi, K., Kargarnovin, M.H. and Gharini, M.: Dynamic analysis of a functionally graded simply supported Euler–Bernoulli beam to a moving oscillator, Acta Mechanica, 224, 425-446, 2013

[103] Rajasekhara, N.N. and Venkateswara, R.G.: Free vibration and stability behavior of uniform beams and columns on nonlinear elastic foundation, Computers & Structures, 58(6), 1213-1215, 1996

[104] Razaqpur, A.G. and Shah, K.R.: Exact analysis of beams on two-parameter elastic foundations, International Journal of Solids and Structures, 27(4), 435-451, 1991

[105] Rieker, J.R., Lin, Y.H. and Trethewey, M.W.: Discretization considerations on moving load finite element beam models, Finite Elements in Analysis and Design, 21(3), 129-144, 1986

[106] Romano, F.: Deflections of Timoshenko beam with varying cross-section, International Journal of Mechanical Sciences, 38(8–9), 1017-1035, 1996

[107] Ronagh, H.R., Bradford, M.A. and Attard, M.M.: Nonlinear analysis of thin-walled members of variable cross-section, Part II: Application, Computers & Structures, 77(3), 301-313, 2000

[108] Ronagh, H.R., Bradford, M.A. and Attard, M.M.: Nonlinear analysis of thin-walled members of variable cross-section, Part I: Theory, Computers & Structures, 77(3), 285-299, 2000

[109] Saffari, H., Rahgozar, R. and Jahanshahi, R.: An efficient method for computation of effective length factor of columns in a steel gabled frame with tapered members, Journal of Constructional Steel Research, 64(4), 400-406, 2008

[110] Severn, R.T.: Inclusion of shear deformation in the stiffness matrix for a beam element, Journal of Strain Analysis, 5, 239-241, 1970

[111] Shahba, A., Attarnejad, R., Marvi, M.T. and Hajilar, S.: Free vibration and stability analysis of axially functionally graded tapered Timoshenko beams with classical and non-classical boundary conditions, Composites: part B, 42(4), 801-808, 2011

[112] Shahba, A., Attarnejad, R. and Hajilar, S.: Free vibration and stability of axially functionally graded tapered Euler–Bernoulli beams, Shock & Vibration, 18(5), 683-696, 2011

[113] Shahba, A., Rajasekaran, S.: Free vibration and stability of tapered Euler–Bernoulli beams made of axially functionally graded materials, Applied Mathematical Modelling, 36, 3094-3111, 2012

[114] Şimşek, M. and Kocaturk, T.: Free and forced vibration of a functionally graded beam subjected to a concentrated moving harmonic load, Composite Structures, 90(4), 465-473, 2009

[115] Şimşek, M.: Vibration analysis of a functionally graded beam under a moving mass by using different beam theories, Composite Structures, 92(4), 904-917, 2010

[116] Şimşek, M.: Non-linear vibration analysis of a functionally graded Timoshenko beam under action of a moving harmonic load, Composite Structures, 92, 2532-2546, 2010

[117] Şimşek, M., Kocaturk, T. and Akbąs, D.: Dynamic behavior of an axially functionally graded beam under action of a moving harmonic load, Composite Structures, 92(4), 904-917, 2012

[118] Sina, S.A., Navazi, H.M. and Haddadpour, H.: An analytical method for free vibration analysis of functionally graded beams, Materials & Design, 30(3), 741-747, 2009

[119] Singh, K.V. and Li, G.: Buckling of functionally graded and elastically restrained non-uniform columns, Composites: Part B, 40, 393-403, 2009

[120] Suresh, S. and Mortensen, A.: Functionally graded materials, The Institute of Materials, IOM Communications Ltd., London, 1998

[121] Tamura, I., Tomota, Y. and Ozawa, H.: Strength and ductility of Fe-Ni-C alloys composed of austenite and martensite with various strength, In: Proceedings of the 3rd International Conference on Strength of Metals and Alloys, Vol. 1, Institute of Metals, Cambridge, 611-615, 1973

[122] Tang, X.D.: Shape functions of tapered beam–column elements. Computers & Structures, 46(5), 943-953, 1993

[123] Tessler, A. and Dong, S.B.: On a hierarchy of conforming Timoshenko beam elements, Computers & Structures, 14, 335-344, 1981

[124] Thambiranam, D. and Zhuge, Y.: Dynamic analysis of beams on elastic foundation subjected to moving loads, Journal of Sound and Vibration, 198(2), 149-169, 1996

[125] Thomas, D.L., Wilson, J.M. and Wilson, R.R.: Timoshenko beam finite elements, Journal of Sound & Vibration, 31, 315-330, 1973

[126] Thomas, J. and Abbas, B.A.H.: Finite element model for dynamic analysis of Timoshenko beam, Journal of Sound & Vibration, 41, 291-299, 1975

[127] Timoshenko, S.P.: On the correction for shear of the differential equation for transverse vibrations of prismatic beams, Philosophical Magazine, 41, 744-746, 1921

[128] Timoshenko, S.P.: On the transverse vibrations of bars of uniform cross-section, Philosophical Magazine, 43, 125-131, 1922

[129] To, C.W.S.: Higher order tapered beam finite elements for vibration analysis, Journal of Sound and Vibration, 63(1), 33-50, 1979

[130] To, C.W.S.: A linearly tapered beam finite element incorporating shear deformation and rotary inertia for vibration analysis, Journal of Sound and Vibration, 78(4), 475-484, 1981

[131] Tong, X., Tabarrok, B. and Yeh, K.Y.: Vibration analysis of Timoshenko beams with non-homogeneity and varying cross-section, Journal of Sound and Vibration, 186(5), 821-835, 1995

[132] Touloukian, Y.S.: Thermophysical properties of high temperature solid materials, Macmillan, New York, 1967

[133] Trinh, T.H. and Gan, B. S.: Development of consistent shape functions for linearly solid tapered Timoshenko beam, Journal of Structural and Construction Engineering, Transactions of AIJ, 80, 713, 1103-1111, 2015

[134] Valipour, H.R. and Bradford, M.A.: A new shape function for tapered three-dimensional beams with flexible connections, Journal of Constructional Steel Research, 70, 43-50, 2012

[135] Vu Quoc, L. and LeGer, P.: Efficient evaluation of the flexibility of tapered I-beams accounting for shear deformations, International Journal for Numerical Methods in Engineering, 33, 553-566, 1992

[136] Wattanasakulpong, N., Gangadhara Prusty, B. and Kelly, D.W.: Thermal buckling and elastic vibration of third-order shear deformable functionally graded beams, International Journal of Mechanical Sciences, 53, 734-743, 2011

[137] Wood, R.D. and Zienkiewicz, O.C.: Geometrically nonlinear finite element analysis of beams, frames, arches and axisymmetric shells, Computers & Structures, 7, 725-735, 1977

[138] Yang, Q., Zheng, B.L., Zhang, K. and Li, J.: Elastic solutions of a functionally graded cantilever beam with different modulus in tension and compression under bending loads, Applied Mathematical Modelling, 38(4), 1403-1416, 2014

[139] Zhang, Y., Huang, H. and Han, Q.: Buckling of elastoplastic functionally graded cylindrical shells under combined compression and pressure, Composites Part B: Engineering, 69, 120-126, 2015

[140] Zhang, D.G.: Nonlinear bending analysis of FGM beams based on physical neutral surface and high order shear deformation theory, Composite Structures, 100, 121-226, 2013

[141] Zhaohua, F. and Cook, R.D.: Beam elements on two-parameter elastic foundations, Journal of Engineering Mechanics, 109(6), 1390-1402, 1983

[142] Zheng, D.Y., Cheung, Y.K., Au, F.T.K. and Cheng, Y.S.: Vibration of multi-span non-uniform beams under moving loads by using modified beam vibration functions, Journal of Sound and Vibration, 212(3), 455-467, 1998

[143] Zienkiewicz, O.C. and Taylor, R.L.: The finite element method, Vol. 2: Solid and fluid mechanics, dynamics and non-linear problems, 4th ed., McGraw-Hill, London, 1991